University of Napoli Federico II
Department of Physics

An Optical ReadOut for the Gravitatonal Reference Sensor of LISA

Candidate:

Adele La Rana

Fundamental and Applied Physics
Doctoral Thesis
XX Cycle - December 2007

Coordinator:
Prof. Gennaro Miele

Advisor:
Dr Luciano Di Fiore

To my family
with all my love

A reasonable starting point for a discussion of the many-body problem might be the question of how many bodies are required before we have a problem. In 18th century newtonian mechanics the three body problem was insoluble. With the birth of general relativity, around 1910, and quantum electrodynamics, around 1930, the two and one body problems became insoluble. And with modern quantum field theory, the problem of zero bodies (vacuum) is insoluble. So, if we are out after exact solutions, no bodies at all is already to many.

Richard Mattuck,
A Guide to Feynmann Diagrams and the Many-Body problem.

DON'T PANIC.

Douglas Adams,
The Hitch-Hikers Guide to the Galaxy.

Introduction

Einstein's General Relativity shows that compact concentrations of matter and energy modify the intimate structure of spacetime, warping it and changing the distance between points. In a dynamic universe, these concentrations vary shape and position in time, so the curvature also has to vary.
Already in 1916, few years after the first formulation of general relativity, Einstein inferred that the information about the variation had to propagate through space at the velocity of light by means of waves. These are the gravitational waves, ripples of the fabric of spacetime propagating at the same velocity of electromagnetic waves and carrying the information about how a time varying distribution of matter and energy affects spacetime curvature.
Gravitational waves constitute a fundamental prediction of General Relativity which hasn't found yet a direct experimental proof. Nevertheless a very stringent indirect confirmation of their existence has been provided by the observation of the binary star system PSR1913+16, accomplished by Russell Hulse and Joseph Taylor (Nobel Prize 1993). Their studies demonstrated that the variation in the orbital period of the system was predicted with extreme accuracy by energy loss due to gravitational wave emission.
Besides energy loss, gravitational waves produce direct physical effects, in terms of distance variation between free falling proof masses. This is the phenomenon on which the idea of direct detection is based.
The extremely weak interaction of gravitational radiation with matter makes the detection an extremely challenging task, but at the same time it constitutes an essential reason of scientific interest: gravitational waves can travel

through large distances virtually unmodified, bringing information from regions of the universe which cannot be observed by means of electromagnetic radiation.
Detecting gravitational waves will constitute the first step towards a completely new way of looking at the Universe, through the foundation of the so called gravitational wave astronomy.
This extremely high interest related to gravitational wave detection and observation has motivated and motivates the research of hundreds of physicists, engineers, mathematicians and computer scientists which keep cooperating in order to develope and improve the theoretical and practical issues needed for finally capturing gravitational radiation.
The idea of direct detection is based on measuring extremely small distance variations: starting from the '60, when the first resonant bars were built, all the technology that has been developed so far in the gravitational wave detection field aims at this conceptually simple task. However neither the resonant bar antennas nor the current ground-based interferometric antennas, which are the two kinds of gravitational wave detectors actually existing, have yet succeeded.
LISA (Laser Interferometer Space Antenna) will be the first space-borne gravitational wave interferometer. It is an ESA-NASA joint mission, with launching date scheduled for 2018. While its ground-based companions aim at the detection of gravitational signals with frequencies ranging from 10, $100\,Hz$ to $10000\,Hz$, LISA is sensitive to the frequency band $10^{-4}\,Hz - 10^{-1}\,Hz$. Different astrophysical gravitational wave sources correspond to these different frequency ranges.
Galactic binary pulsars and massive blackholes, which are the most promising source of gravitational waves, emit at frequencies lower than $1\,Hz$. Many of them are expected to be detectable by LISA. There is also a number of known 'guaranteed sources' for LISA, the so called verification binaries. However, the complementarity of the detectable signals makes sure that the united effort of ground-based interferometers and LISA can provide a wide

map of gravitational wave sources.
LISA is constituted of three spacecraft, orbiting the sun in a giant triangular formation and exchanging laser light beams in a modified Michelson interferometer setup. Differently from the proof masses of the ground-based interferometers, which are suspended to extremely sophisticated supports for noise isolation purposes, LISA test masses are in a true free fall condition.
Each spacecraft encloses and protects from external disturbances two freely floating test masses, following their geodesic motion and keeping as stationary as possible with respect to them. However, if left to itself, the spacecraft could not purchase this purpose, because of the external perturbations preventing it from actual free fall. A control system is then needed, in order to properly readjust at every time the position of the spacraft around the test masses.
This system is the so called drag-free control loop. Position sensors read the displacements of the spacecraft relatively to the test masses and the measured signals are used to drive special microthrusters, which correct the spacecraft position.
The displacement readout is operated by the so called Gravitational Reference Sensor (GRS).
Actually, it is not possible to keep the spacecraft stationary around the test masses by moving only the spacecraft, owing to the geometrical configuration of the system. It is necessary to readjust the position of the proof masses themselves with respect to the spacecraft. Since the detection concerns only the interferometric axes, it is necessary to keep a high quality free fall along those directions. Therefore the position of the proof mass positions will be corrected only along directions ortogonal to the optical axes, by means of electrostatic actuation. The position of the spacecraft will instead be readjusted by the microthrusters along the sensitive axes of the interferometer. The control signals for both the electrostatic actuators and the microthrusters are provided by the GRS.
The GRS can be a dangerous source of disturbance in its turn, because

the position sensing noise enters the drag-free control loop. Furthermore this noise can be reproduced by electrostatic actuators along the interferometer axes, by means of cross-coupling mechanisms among different degrees of freedom. In order to achieve the extremely demanding goal sensitivity of LISA, the $2\,kg$ proof masses must follow a geodesic motion with a residual acceleration $\leq 3 \cdot 10^{-15}\, m\, s^{-2}\, Hz^{-1/2}$ in the LISA frequency band. The position sensing noise coupled to the main axes of the interferometer must not spoil this condition.

The previous reasonings point out that the GRS plays a key rule in LISA and that its noise level is crucial for succeeding in gravitational wave detection. Therefore the development of a reliable solution for the GRS with high sensitivity performances is a fundamental task for the scientific outcome of LISA experiment.

The present thesis work concerns the development and experimental validation of a position readout based on optical levers. This optical readout (ORO) is proposed as a backup solution for the LISA GRS. The current reference solution is a capacitive readout, which has been developed by the LISA group in Trento and which will fly on the LISA technology demonstration mission, LISA Pathfinder, in 2010. The proposal of a backup solution replies to the necessity of mission risk reduction, which is obviously a fundamental task in a space-based experiment. Furthermore an optical readout is potentially more sensitive than a capacitive sensor and can thus relax the demanding requirement on cross-couplings imposed by this latter.

An auxiliary readout has the further advantage of providing extra-information on couplings. However, among other kinds of optical readouts, potentially more sensitive than required for LISA, the choice of a system based on optical levers is particularly interesting for its simplicity, which is a fundamental issue for a device planned to work in space.

The original research carried out during this thesis work concerned:

- the tests of the ORO in rigid bench-top setups, which allowed to demonstrate experimentally the ORO sensitivity performances and to estab-

lish some baseline solutions for the devices to use on LISA;

- the development, manufacturing and testing of a real-scale bench-top prototype representing a possible integration scheme of the ORO sensor in LISA, activity which has given positive results;

- the development of an ORO system to integrate on the four mass torsion pendulum in Trento, in order to test the ORO in a free fall approximation along one degree of freedom, its effective integration in the facility and the first results from the tests in Trento. This last activity has been accomplished in collaboration with the LISA group of Trento.

The mentioned research topics are enclosed partly in chapter II and then in chapter III, IV and V. Most of the work has been accomplished in the LISA laboratory of Napoli, while the experimental activity concerning the integration of the ORO on the pendulum and the related tests has required a transfer to Trento laboratory.

In chapter I there is an introduction to the basic concepts about gravitational waves, together with a short description of the current ground-based interferometers. Then the LISA experiment is illustrated in some detail, showing the differences and the main advantages with respect to the ground-based antennas. A section is dedicated to the the expected sources for LISA. Finally a brief description of LISA Pathfinder is presented.
A detailed description of the ORO concept and its model noises is given in chapter II. Here a short discussion of the capacitive sensor is also found, which allows to state the requirements for the ORO and to compare the expected performances, associated to the relative cross-coupling requirements. Chapter III is devoted to the tests of the ORO in bench-top setups and to the research of possible baseline solutions for LISA. Chapter IV describes the activity concerning the integration of the ORO in LISA and the real scale prototype accomplished for bench-top testings.
Finally chapter five deals with the integration of the ORO in the torsion

pendulum and the experimental results so far achieved.

Actually, the development of the ORO sensor for LISA had a very interesting technological transfer, resulting in a collaboration with the VST (Very Large Telescope Survey Telescope) group of Napoli. A small part of my research activity has been devoted to the development of an ORO system to be integrated in the secondary mirror of the VST, with the purpose of characterizing the system for the positioning and the orientation of the mirror. Since this work is not within the purposes of this thesis, it is briefly exposed in appendix A, referring for further details to the related article.

Contents

List of Figures

Chapter 1

Detecting Gravitational Waves with LISA

The acronyme LISA stands for Laser Interferometer Space Antenna. LISA will be the very first gravitational wave detector operating in space.
The experimental apparatus consists of the hugest and most sophisticated interferometer for gravitational wave detection ever conceived: three identical spacecraft orbiting the Sun in a triangular formation will constitute a kind of modified Michelson interferometer, with an extra-arm and armlenth of 5 million kilometers!
LISA is an ESA-NASA joint mission. Its launching date is expected around 2018. A preliminary technology testing mission, LISA Pathfinder, will be sent into orbit in 2010.
LISA will be sensitive to very low frequency gravitational waves, emitted typically by very massive sources, as massive black hole binary systems. Many expected gravitational wave sources are known to be in LISA frequency range $(0.1\,mHz - 100\,mHz)$.
LISA will be a very powerful instrument for atsrophysical observation: gravitational wave signals detected by LISA can provide fundamental information from near and far Universe, information which are complementary to those brought by elecromagnetic radiation.

In the first section of this chapter I will briefly introduce gravitational waves. Then I will describe in a certain detail LISA apparatus, its sensitivity and the expected detectable sources. In the last section I will shortly discuss LISA Pathfinder mission.

1.1 Gravitational Waves

The detection of gravitational waves is one of the present frontiers of General Relativity. The existence of gravitational waves was predicted by Einstein since 1916, as a consequence of the theory of General Relativity, but till now there is only an indirect experimental evidence about them.
This evidence stands in Hulse's and Taylor's observation of the first binary pulsar ever sighted, the system PSR1913+16, discovered by them in 1974. In over 10 years of observations, the two scientists measured a progressive reduction of the orbital period of the binary star and verified that it could be very precisely predicted by progressive energy loss due to gravitational wave emission. The discovery yielded to Hulse and Taylor the Nobel Price for Physics in 1993.
Later on the discovery and observation of other binary pulsars confirmed the indirect evidence of the existence of gravitational waves. In 2004 an international team of astronomers announced the discovery of the first double-pulsar system, J0737-3039A/B, in which both neutron stars emit detectable radiation as pulsars: after only 3 years of observation, the system provided the same level of agreement with Einstein's theory as Hulse's and Taylor's binary [1].
In the last fifty years many dedicated instruments have been carried out for direct detection of gravitational waves. Starting from the first resonant bars, conceived by John Weber in the '60s [2][3], the history of gravitational wave detection passes through the development of many generations of resonant detectors, built all around the world and still technologically improving [4] [5]. On the other hand investigations into laser-interferometric gravitational

wave antennas began in the '70s, and finally in the last few years a world wide network of interferometric detectors has started to take data.
Nevertheless gravitational waves still slip detection, no experiment has succeeded yet. Alternate manifestations of pure enthusiasm and open skepticism couple to the expectations of the scientific community, which are very high.

What are gravitational waves and what makes them so difficult to detect? This section deals with these two questions.

1.1.1 Einsten's Field equations predict Gravitational Waves

Einstein's General Relativity equations describe the way matter and energy affect space-time. Given a certain distribution of matter and energy, which is the other face of matter, the equations tell how this distribution determines the geometry of space-time:

$$R_{\mu\nu} - \frac{1}{2}Rg_{\mu\nu} = \frac{8\pi G}{c^4}T_{\mu\nu} \qquad \mu, \nu = 0, 1, 2, 3. \tag{1.1}$$

The left hand side contains the geometrical information: $R_{\mu\nu}$ is Ricci tensor and $R = g_{\mu\nu}R^{\mu\nu}$ is the trace of $R_{\mu\nu}$[6] [7] [8].
A fundamental term is the metric tensor $g_{\mu\nu}$, which defines the distance between two points of spacetime when matter is present:

$$ds^2 = g_{\mu\nu}dx^\mu dx^\nu. \tag{1.2}$$

If there were no gravitational sources and no gravitational perturbations, spacetime would be flat and the metric tensor $g_{\mu\nu}$ would become the metric of flat spacetime, that means Minkowski metric tensor $\eta_{\mu\nu}$:

$$\eta_{\mu\nu} = \begin{pmatrix} -1 & 0 & 0 & 0 \\ 0 & 1 & 0 & 0 \\ 0 & 0 & 1 & 0 \\ 0 & 0 & 0 & 1 \end{pmatrix}. \tag{1.3}$$

In this case the distance between two close points of spacetime is simply:

$$ds^2 = \eta_{\mu\nu} dx^\mu dx^\nu = -c^2 dt^2 + dx^2 + dy^2 + dz^2. \tag{1.4}$$

The right hand side of Einstein's field equations (1.1) describes the distribution of energy and matter, through the energy-impulse tensor $T_{\mu\nu}$. The quantity G is the universal gravity constant and its value is $(6.6732 \pm 0.0031) \times 10^{-11}\, m^3/(s^2\, kg)$.
The presence of matter and energy affects the metric of spacetime, that means the way we calculate the distance between points. If the distribution of energy and matter changes in time, so has to do spacetime curvature. The information about the changes in the metric have to travel in some way and propagate from the source to all the surrounding points of spacetime. Carriers of this information transmission are the gravitational waves.

In the weak field approximation, which means far enough from gravitational sources in order to consider spacetime almost flat, it is possible to find a coordinate system in which the metric tensor can be written as

$$g_{\mu\nu} = \eta_{\mu\nu} + h_{\mu\nu} \qquad |h_{\mu\nu}| << 1, \tag{1.5}$$

where $h_{\mu\nu}$ is a little perturbation on Minkowski's metric. There are infinite coordinate systems which allow this, so we can take advantage of the needless degrees of freedom by imposing a simplifing coordinate transformation, called Lorenz gauge transformation:

$$\partial_\mu h^\mu_\lambda - 1/2 \partial_\lambda h = 0 \qquad \text{Lorenz gauge.} \tag{1.6}$$

Einstein's field equations then become:

$$\Box \bar{h}_{\mu\nu} = \frac{-16\pi G}{c^4} T_{\mu\nu}, \tag{1.7}$$

where $\bar{h}_{\mu\nu}$ is the symmetric tensor $\bar{h}_{\mu\nu} = h_{\mu\nu} - 1/2 \eta_{\mu\nu} h$, $h = \eta_{\mu\nu} h^{\mu\nu}$ being the trace of $h_{\mu\nu}$. The equations (1.7) are Einstein's linearized field equations for

small deviations from flat spacetime. In vacuum, which means gravitational field sources at infinity, equations (1.7) become:

$$\Box \bar{h}_{\mu\nu} = 0. \tag{1.8}$$

As the analogue Maxwell's equations for electromagnetic field, equations (1.8) admit wave solutions. Note that the symmetric tensor $\bar{h}_{\mu\nu}$ has got 6 independent components out of 10, because of the 4 constraints imposed by equations (1.6).

The gauge transformations (1.6) do not unambiguously identify a coordinate system, because the Lorenz conditions and the field equations are both invariant under coordinate transformations $x_\mu \longrightarrow x_\mu + \xi_\mu$ with $\Box \xi_\mu = 0$. We can then impose 4 more constraints through the transverse and traceless gauge conditions, the so called "TT gauge":

$$\bar{h} = 0 \qquad \text{traceless} \tag{1.9}$$

$$\bar{h}_{0\mu} = 0 \qquad \text{transverse.} \tag{1.10}$$

These last gauge conditions identify univocally the coordinate system: these coordinates are called inertial coordinates and correspond to the geodesic curves of free falling masses. Notice that in the TT gauge $\bar{h}^{TT}_{\mu\nu} \equiv h^{TT}_{\mu\nu}$.

Only two independent components are now left for $h_{\mu\nu}$, which represent two transversely polarized wave solutions. If the wave is propagating along the z axis, the general solution of (1.8) can be written as the sum of two components:

$$h^{TT}_{\mu\nu} = h_+ e^+_{\mu\nu} + h_\times e^\times_{\mu\nu}, \tag{1.11}$$

where

$$e^+_{\mu\nu} = \begin{pmatrix} 0 & 0 & 0 & 0 \\ 0 & 1 & 0 & 0 \\ 0 & 0 & -1 & 0 \\ 0 & 0 & 0 & 0 \end{pmatrix} \tag{1.12}$$

and

$$e^{\times}_{\mu\nu} = \begin{pmatrix} 0 & 0 & 0 & 0 \\ 0 & 0 & 1 & 0 \\ 0 & 1 & 0 & 0 \\ 0 & 0 & 0 & 0 \end{pmatrix}. \tag{1.13}$$

The time dependence of the wave is contained in the functions $h_+ \equiv h_+(t)$ and $h_\times \equiv h_\times(t)$. The two independent tensors $e^{+}_{\mu\nu}$ and $e^{\times}_{\mu\nu}$ represent two ortogonal polarization for a gravitational wave propagating along z.

1.1.2 Physical effects of GW passage

Einstein's field equations predict the existence of gravitational waves. Gravitational waves are ripples in the structure of spacetime propagating at the same velocity of light, which carry the information about how a time varying distribution of matter and energy affects the curvature of spacetime.
Gravitational waves are transverse and possess two polarization states, labelled by + and ×. Each of the two polarization states warps spacetime in a peculiar way. If we consider a ring of proof masses in geodesic motion and a wave propagating along a direction ortogonal to the plane containing the ring, the effect would be the one shown in the figure 1.1.

The ring reduces and enlarges periodically along ortogonal directions, depending on the polarization state of the incident gravitational wave.
The passage of a gravitational wave causes a periodical variation in the distances between free falling proof masses: this is the physical effect on which all gravitational wave detectors are based. Detecting this effect is extremely difficult, because distance variations are extremely small.

1.1.3 The quadrupolar nature of gravitational waves

In order to understand the generating process of gravitational waves by a massive source, it is necessary to consider Einstein's linearized field equations (1.7), when matter is present and the energy-impulse tensor is not null.

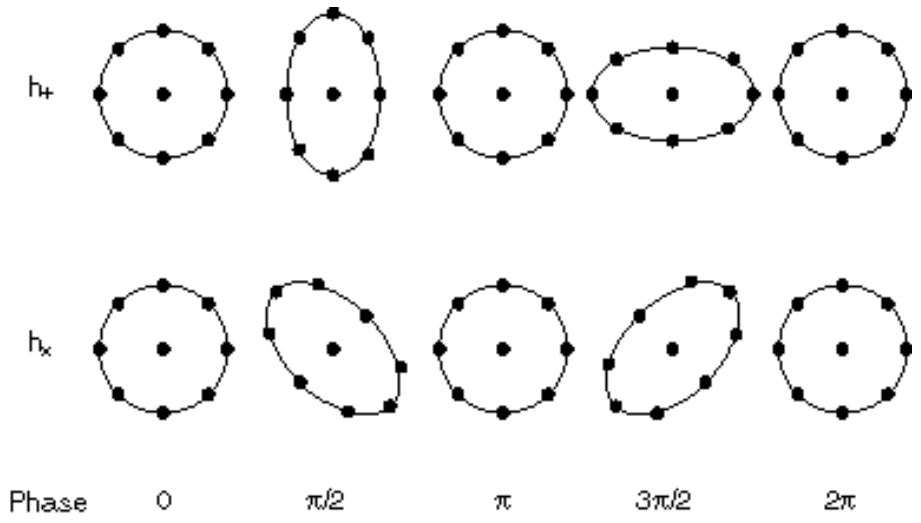

Figure 1.1: Periodic deformations of ring of proof masses, caused by the passage of a gravitational wave propagating ortogonally to the plain containing the ring. The first figure shows the physical effect due to a purely + polarized wave, the second figure shows the case of a pure × polarization.

It is possible to decompose not relativistic sources into multipoles, as for the electromagnetic field. The monopole moment of the mass distribution is the total mass, which is conserved. Analogously to what inferred in electromagnetism from the conservation of the charge, there is no monopole emission of gravitational radiation. Although, unlikely what happens for electromagnetic radiation, also the dipole term is null: the dipole moment of the mass distribution is conserved, because its time derivative is the total momentum of the source, which is constant. Then the dominant term of gravitational radiation results to be the second derivative of the energy density quadrupole moment of the source:

$$\bar{h}_{ij}(t,\vec{x}) = \frac{2G}{Rc^4}\ddot{q}_{ij}(t_r), \tag{1.14}$$

where $t_r = t - |\vec{x} - \vec{y}|/c$ is the delay time and the energy density quadrupole moment is given by

$$q_{ij}(t) = \int_{\vec{y}\in source} y_i y_j T_{00}(t,\vec{y}) d^3\vec{y}. \tag{1.15}$$

This quadrupolar dependence causes gravitational radiation to be very weak. The coupling constant between gravitational radiation and matter is $G/c^5 \approx 10^{-53}\, Watt^{-1}$: it's an indication of how negligible gravitational interaction is, compared to the other fundamental physical interactions. Unfortunately, a very small coupling constant means that also the interaction between gravitational waves and detectors is very weak: this makes the detection of gravitational waves an extremely challenging task. At the same time, this is one of the reasons that makes them so interesting: gravitational waves can travel through space and matter without undergoing almost any alteration, they can then bring information from sources and regions of the Universe which are very far in space and time.
The quadrupolar nature of gravitational radiation implies that sources with spherical symmetry do not emit gravitational waves. In order to detect gravitational waves we have to look for sources having a very large internal kinetic energy due to not spherically symmetric components.

1.2 Ground-based interferometric gravitational wave detectors

A Michelson interferometer is an instrument sensitive to very small changes in the distances between its mirrors. The mirrors can ideally be used as proof masses, while the distance variation between them is measured very accurately through interference of laser light.
The working principle of interferometric gravitational wave antennas is to set the mirrors in a condition as close as possible to free fall, minimizing all not-gravitational perturbations, in order to detect a gravitational wave as a phase variation of the interference pattern of the interferometer. This requires extremely complex and sophisticated technology.
The phase variation due to gravitational waves is proportional to the interferometer length, which means that an interferometric gravitational wave detector is more sensitive the longer is its armlength L. The distance variation

ΔL is obtained from the phase measurents and is related to the gravitational signal as:

$$\frac{\Delta L(t)}{L} \equiv h(t). \tag{1.16}$$

Ground-based interferometric gravitational wave detectors achieve sensitivity of $10^{-23}\, 1/Hz^{\frac{1}{2}}$ and work in the frequency range $10\, Hz - 10000\, Hz$. They deal with extremely delicate problems, such as the suspension of the mirrors and thier isolation from noise, the control of the interferometer on the working point.

Seismic noise limits the sensitivity of Earth-based detectors at frequencies lower than $100\, Hz$. At high frequencies ($f > 500\, Hz$) sensitivity is shot noise limited. In the central part of the band the dominant perturbation is thermal noise.

The ground-based interferometric antennas form a world wide network of scientific collaborations. A very brief description of the state of the art of ground-based gravitational wave interferometer is reported below.

LIGO (USA): The Laser Interferometric Gravity-Wave Observatory is a joining of three interferometers, two in Hanford Reservation, near Seattle, with $2000\, m$ and $4000\, m$ armlengths respectively, and one in Livingston Parish,Louisiana, with $4000\, m$ armlength [10]. LIGO is taking data since 2002 and has reached its nominal sensitivity in 2006. The picture 1.3 shows the sensitivity curves of the three LIGO detectors.

GEO600 (Germany): GEO600 is a british-german collaboration [11]. The experimental apparatus is sited in Hannover and the interferometer arms are $600\, m$ long. Between 2002 and 2006 GEO600 participated in several data runs in coincidence with the LIGO detectors and is now gradually approaching design sensitivity.

TAMA300 (Japan): The japanese detector is located in Tokyo and has $300\, m$ armlength [12]. It has been the first one to reach its nominal sensitivity and is taking data since 2001.

AIGO (Australia): The Australian International Gravitational Observatory interferometer is under construction in Gingin, western Australia. The interferometer will have $5000\,m$ armlength. A southern hemishere detector will largely increase the directional precision of the network, as shown in figure 1.2: a single gravitational source appears as a long streak in the sky without AIGO; with AIGO its location is identified to within less than a half degree [14].

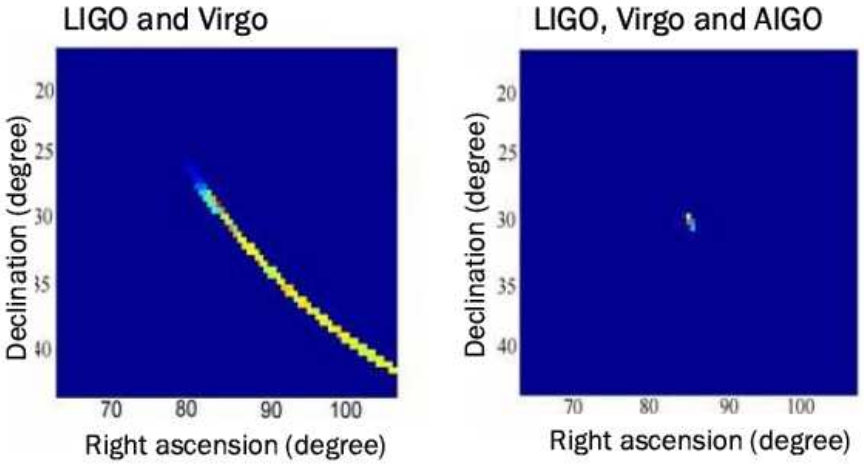

Figure 1.2: AIGO contribution in determining the position of a gravitational wave source: a single source appears as a long streak in the sky when detected by LIGO and VIRGO, while a joined detection of LIGO, VIRGO and AIGO allows to identify the source location to within less than a half degree.

VIRGO (Italy): The french-italian experiment VIRGO has seat in Cascina, near Pisa [13]. The interferometer has arms $3000\,m$ long. Virgo started its science runs the 22nd of May of this year. As you can see in figure 1.3, the actual sensitivity curve is still not the expected one, especially at the lower frequencies. A peculiar feature of Virgo is the extremely sophisticated suspension system of the mirrors: it is called "superattenuatore" and is made of a chain of five pendular attenuation stages, attached to an actively stabilized platform, laying on top of an inverted pendulum, which compensates for very low frequency and large ampli-

tude oscillations. The system allows to extend Virgo's sensitivity range down to $10\,Hz$.

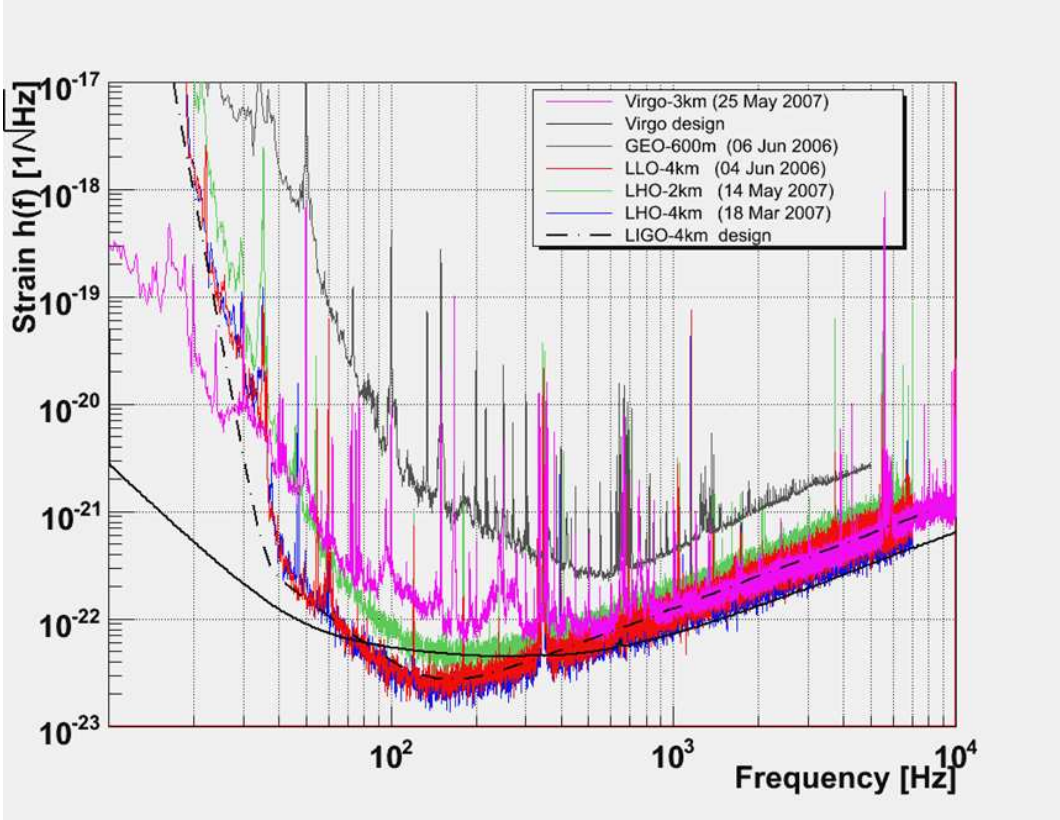

Figure 1.3: Comparison between the sensitivies of different ground-based interferometers. The black continous line represents VIRGO goal sensitivity, while the magenta line is VIRGO's experimental curve, measured the 25th of May of 2007. The red and blue line are the experimental sensitivity curves of LIGO (km) respectively measured on the 4th of June 2006 and on the 17th of March 2007, which match already very well the dashed line representing LIGO's model sensitivity. The higher grey curve is the experimental sensitivity curve of GEO600 (6 June 2006), while the green curve is referred to LIGO ($2\,km$).

These interferometric detectors have different sensitivities corresponding to their different armlengths. The most sensitive are of course LIGO and VIRGO, which have very similar expected performances.

Thanks to its original seismic isolation system, Virgo is the only ground-based interferometric antenna to be sensitive starting from $10\,Hz$. A much more performant seismic isolation looks unachievable: below $1\,Hz$ another terrestrial noise overcomes the expected astronomical signals, the so called Newtonian noise, which is due to time-dependent variations in the local Newtonian gravitational field. It isn't possible to isolate ground-based detectors from this gravity-gradient noise, which plays on such low frequencies.
On the other hand, galactic binary pulsars and massive black hole binaries are the most promising gravitational wave sources, but they emit at frequencies lower than $1\,Hz$ and are not detectable by ground-based detectors.
The brief discussion at the beginning of this section and this last point show the main advantages of making a space-based gravitational wave detector:

- the true geodesic motion of the proof masses;
- the possibility of making optical paths virtually as long as we wish;
- the absence of seismic and gravity-gradient noise and the consequent break-through towards very low and mostly interesting frequencies.

As we will see in the following section, LISA will allow to look at gravitational signals with frequencies in the band $0.1\,mHz - 100\,mHz$, which is a window complementary to the one detected by ground-based antennas. The collaboration between ground-based detectors and LISA offers the possibility to look at a very wide frequency distribution of gravitational wave sources.

1.3 LISA

The first concept studies for a space-borne gravitational wave detector date back to 1981. In 1985 P. L. Bender and J. Faller proposed a mission based on three drag-free spacecraft in heliocentric orbit, named LAGOS (Laser Antenna for Gravitational-radiation Observation in Space)[15]. This first proposal had already many elements of present-day Laser Interferometer Space

Antenna (LISA) mission.
LISA is an ESA-NASA project, under study since 1993. Many different arrangements have been proposed through the years and many alternative operative solutions are still under discussions nowadays. Here I will describe only the "traditional" working scheme of LISA.
The LISA project is in Phase A at both ESA and NASA since 2004. At the moment the launch is expected for 2018. The LISA Pathfinder mission will take off in 2010, with preliminary technology testing purposes.

1.3.1 A panoramic view of LISA

The basic idea is to place proof masses in space in true geodesic motion, a great distance apart and to measure interferometrically the distance variations induced by a passing gravitational wave.
In the present LISA design there are six proof masses in total, two by two shielded by three spacecraft from the external disturbances (solar wind, solar radiation pressure, etc...). The optical interferometric instrumentation is solidal to the spacecraft. While the two near proof masses are freely floating in space, the hosting spacecraft must keep as stationary as possible with respect to them and avoid any interference with their geodesic motion. This purpose is obtained measuring and correcting the relative position with a drag-free control loop, as will be explained in the next paragraph. The drag-free control will be discussed in detail in the second chapter.

After the launch, the three identical spacecraft constituting LISA will take one year to reach their final orbits, placing themselves at the vertices of an equilateral triangle with 5 million kilometer sidelength. This peculiar arm-length has been chosen for LISA to optimize sensitivity at the frequencies of expected gravitational wave sources.
During the long voyage towards the final orbits the proof masses are solidly anchored to the spacecraft by the so called caging mechanism, getting released only at destination.
Figure 1.4 illustrates the final configuration of LISA. Each spacecraft follows

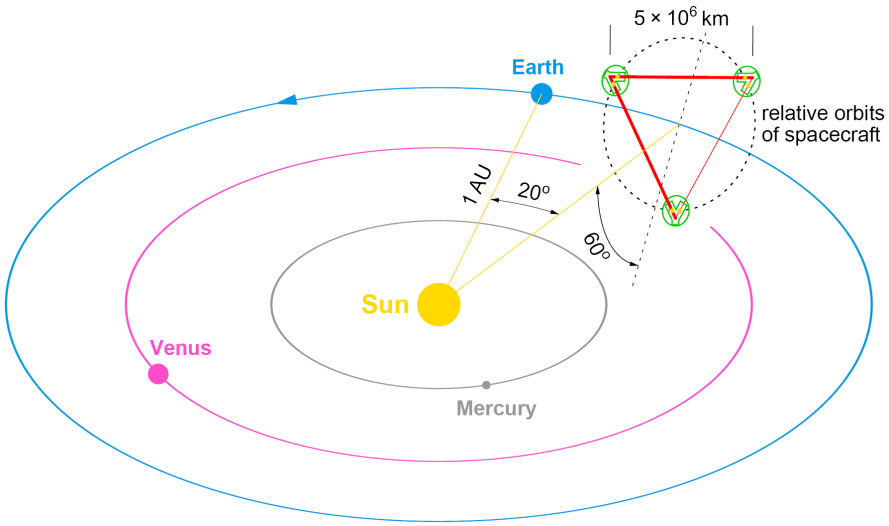

Figure 1.4: LISA configuration: the giant equilateral triangle moves in an earth-like orbit ($R = 1\,AU$), 20° behind the Earth [15]. The plane of the triangle is inclined at 60° to the ecliptic. Drawing is not to scale: the LISA constellation is drawn one order of magnitude larger than the true one.

its own orbit around the Sun: the orbits are chosen to keep the triangle sides as close to equal as possible over the mission lifetime. The three individual orbits have their inclinations and eccentricities such that the giant triangle rotates around its axis, keeping a 60° inclination with respect to the Earth's ecliptic plane. At the same time the center of the LISA constellation moves around the Sun in an earth-like orbit ($R = 1\,AU$), 20° behind the Earth [15]. As shown in the figure 1.5, the constellation revolves once around its center while completing one turn of its orbit, that means once a year.

The described geometry has the further advantage of exposing always the same side of the spacecraft to sun radiation, providing a thermally very stable environment. Furthermore solar pannels on the illuminated lid collect the incident sunlight for power supply.

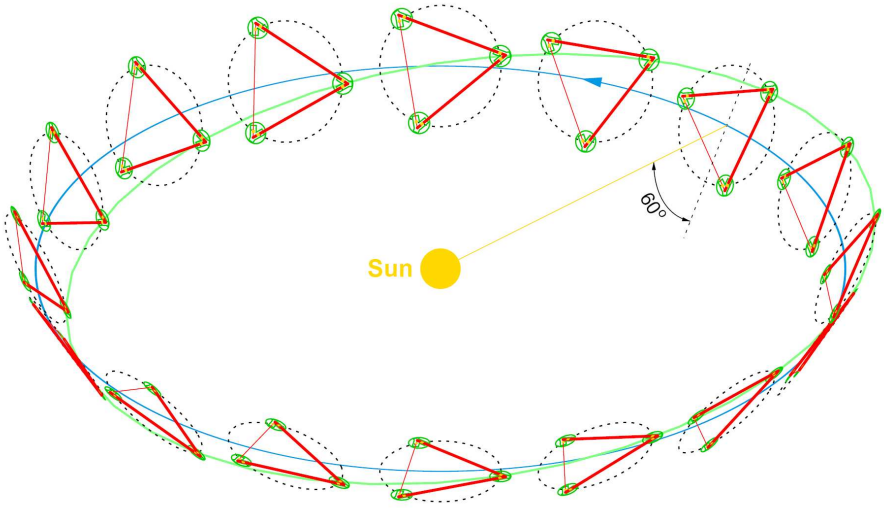

Figure 1.5: The final orbits of LISA spacecraft: each spacecraft moves on its own orbit. The triangular constellation appears to rotate once around its center in the course of a year's revolution around the Sun.

1.3.2 The spacecraft

Each spacecraft has the shape of a flat cylindrical box, containing a Y-shaped payload with arms subtending an angle of 60° [15], as shown in figure 1.6. Each arm of the payload includes an optical bench, a telescope for receiving and transmitting light and two lasers (one for backup purpose).
Each telescope points at one of the distant spacecraft at the other two corners of the triangle.

On each optical bench is assembled an electrode housing, which surrounds the cheif protagonist of the LISA adventure: the free falling proof mass. This is a $46\,mm$ AuPt cube (Au 90% Pt 10%) having a mass of $1.3\,kg$. The composing material assures very high reflectivity and magnetic susceptibility down to $3 \cdot 10^{-6}$, with a residual magnetic moment below $0.02\,\mu A\,m^2$.
The electrode housing hosts the so called Inertial Sensor or Gravitational Reference Sensor (GRS), which measures the relative position of the proof mass with respect to the spacecraft and provides the control signals for the drag-free control loop. We will speak in detail about the GRS in the next

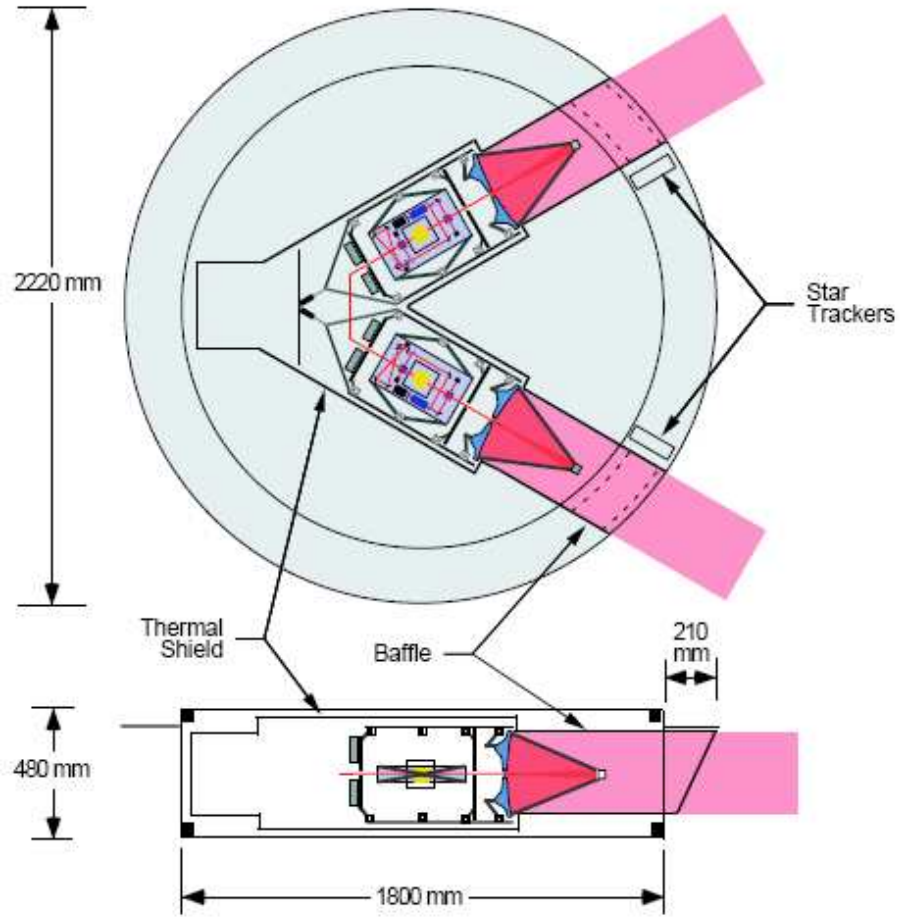

Figure 1.6: LISA spacecraft. Upper part: top view of the spacecraft showing the payload with its two optical assemblies. Lower part: one of the two payload arms.

chapter.

Because of the 60° angle between the proof masses, the correction of the relative position of proof masses and spacecraft can be achieved only by means of moving both the spacecraft and the masses.

In order not to spoil LISA sensitivity to gravitational waves, the position readjustment in the directions of the optical axes is obtained by moving the spacecraft: special microthrusters force the spacecraft to follow the displacements of the freely floating proof mass along that degree of freedom. These thrusters represent a really challenging technological task: they are

ion-emitting precision microthrusters capable of exerting on the spacecraft forces of few micro-newtons.
On the other hand, along the transverse degrees of freedom the position readjustment is obtained by means of electrostatic actuation on the proof masses: electrostatic actuators hosted on the electrode housing allow to move each test mass individually in the directions ortogonal to the corresponding interferometer arm.[1]
Electrostatic actuators and microthrusters are both driven by the GRS, in order to keep the relative position of spacecraft and proof masses as stationary as possible.
On the electrode housing are also mounted the UV flash lamps, which are used to free the proof mass from net charges deposited by cosmic rays and other agents.
The planned light sources are solid-state diode-pumped monolithic miniature Nd-Yag ring lasers, which will emit a continuous $1\,Watt$ infrared beam with a wavelength of $1.064\,\mu m$.

1.3.3 The optical scheme

Each laser is phase-locked either to its companion on the same spacecraft or to the incoming light from the distant one: the first phase-locking system works as a beamsplitter, the second one as an amplifying mirror or light transponder (see figure 1.7.

The laser light going out from one spacecraft to the other corners is not reflected back directly. Amplification at the end spacecraft is required, due to divergence of the beam over the very large distance. An extremely narrow outgoing beam, a few micro radians wide, would still appear spread out over a radius about $20\,kms$ long, after travelling $5\times10^9\,kms$. This estimate can be

[1] The configuration of electrostatic actuators in LISA electrode housings allow to move the test masses in all the six degrees of freedom, but in the drag-free control loop only the actuators relative to the transverse degrees of freedom are used.

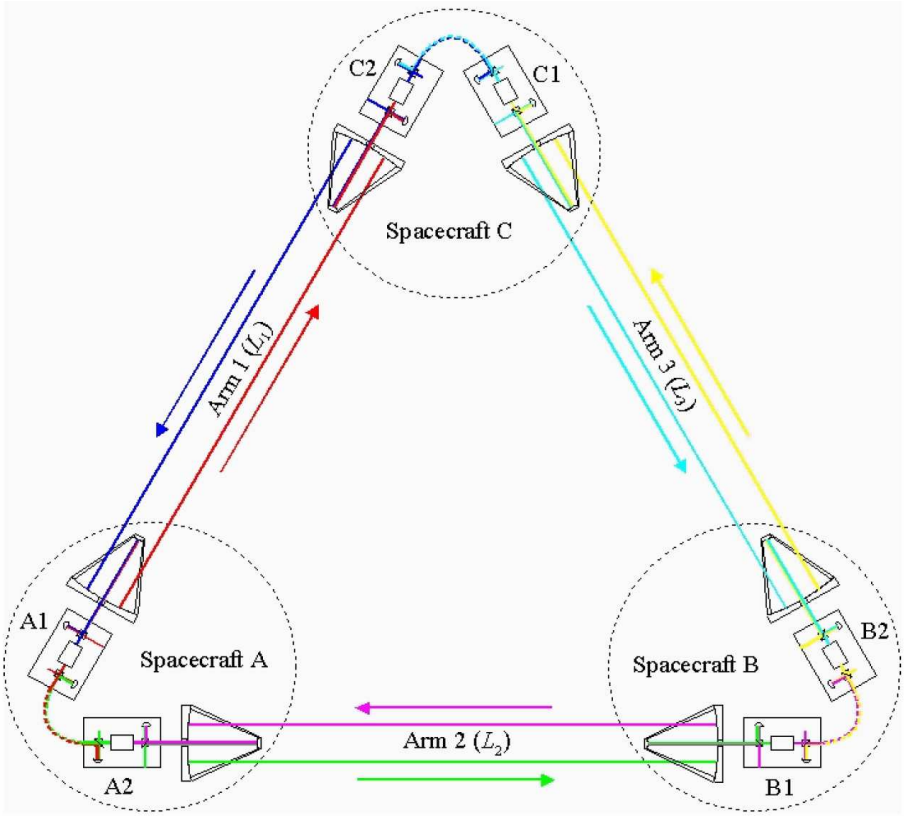

Figure 1.7: LISA Optical Scheme.

easily obtained from the formula describing the propagation of of a gaussian beam [16]. If $w_0 = 30\,cm$ is the initial waiste of the beam, corresponding to the telescope diameter, and L and λ are respectively the traveling distance (LISA armlength) and the wavelength of the laser beam, the waiste of the beam at the distant spacecraft is given by:

$$w = 2\left\{\frac{w_0^2}{4}\cdot\left[1+\left(\frac{\lambda L}{\pi\cdot w_0^2/4}\right)^2\right]\right\}^{1/2} \approx 25\,km. \tag{1.17}$$

Only a very small fraction of the original power, around $\frac{\pi(w_0/2)^2}{\pi(w/2)^2} \approx 10^{-10}$, reaches the end photodiode. This means that if the optical power is $1\,W$ at the beginning, only about $100\,pW$ arrive at destination.

Therefore the laser on the distant spacecraft is phase-locked to the incoming light, after the latter is been reflected off the proof mass and then a phase

replica is transmitted back at full intensity. When the transponded laser beam arrives back at the original spacecraft, it is reflected by the local proof mass and superposed with a portion of the original laser light, which works as a local oscillator in a standard heterodyne detection scheme. This relative phase gives information about the length variation of that interferometer arm.
This basic scheme is repeated along the other arms. The phase measurement for different arms are compared. Optical path difference changes and laser frequency noise are so determined.

1.3.4 LISA Sensitivity

LISA will measure length changes between its arms with sub-Angstrom precision. Taking account of the considerable armlength, LISA will be able to detect gravitational wave induced strains of amplitude $h = \Delta L/L \approx 10^{-23}$ with one year of observations and signal to noise ratio of 5. Figure 1.8 shows LISA sensitivity curve.

As you can see from figure 1.8, LISA is sensitive in the frequency band $0.1mHz - 100mHz$.
LISA sensitivity is limited at lower frequencies ($f < 3\,mHz$) by proof mass acceleration noise, which is due to stray forces perturbing the proof masses from their nominal geodesic motion, as we will see in next subsection. At higher frequencies position noise, essentially laser shot noise, is dominant. The current estimate gives a power spectral density with a $1/f^2$ slope in low frequency, that becomes a white noise in high frequency, with a corner at about $3\,mHz$. The white noise level is expected to be $4 \cdot 10^{-21}\,1/Hz^{1/2}$, quickly degraded above $20\,mHz$ by the loss in the antenna transfer function, due to the finite light travel time [3]. For a detailed discussion of the noises limiting LISA performances I refer to [15] [19].
A very peculiar feature of LISA sensitivity curve is that a diffuse background of unresolved galactic binaries is expected to contribute to the measured

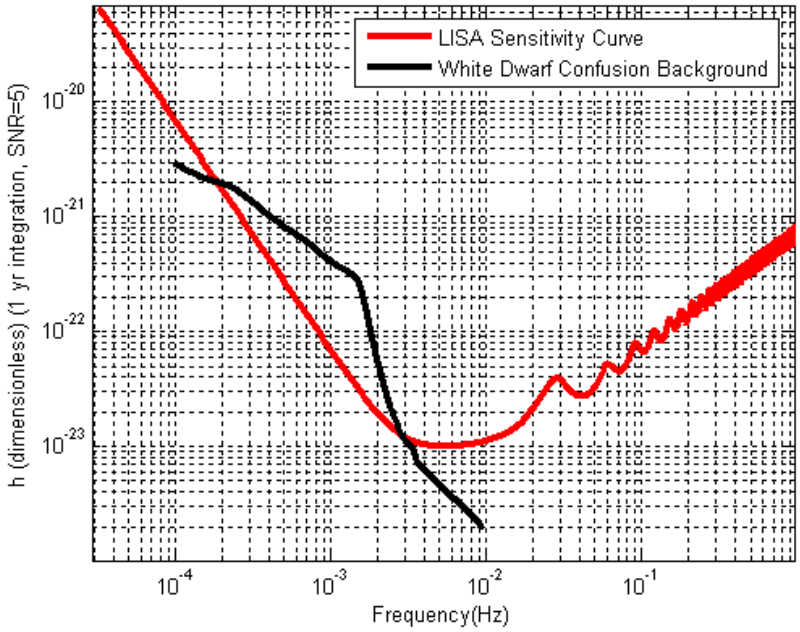

Figure 1.8: LISA Sensitivity Curve: it is expressed in terms of the dimensionless strain h. The graph is produced by using the *LISA sensitivity Curve Generator* tool [17]. The curve is calculated integrating over one year of observation and for a signal to noise ratio of 5. The black line represents the white dwarf binary confusion.

strain level in the frequency range $0.1 - 1\,mHz$. The galactic binary background will be discussed in the paragraph concerning LISA sources.
For ground-based interferometric detectors a fundamental issue is the isolation of the mirrors from noise sources. Analogously, for LISA the primary request is the geodesity of proof masses motion. LISA sensitivity depends on the ability in setting and keeping the proof masses in a condition as close as possible to pure geodesic motion, at least along the interferometer optical axes.

Figure 1.9 shows the LISA sensitivity curve compared to the sensitivity curve of VIRGO. The main difference between the two stands in their frequency bands, which determine the different astrophysical sources to which the experiments aim.

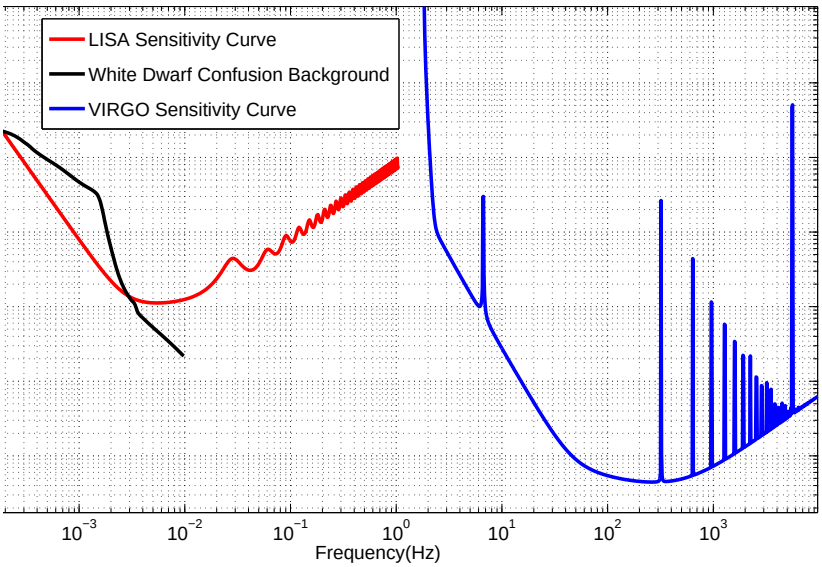

Figure 1.9: Comparison between LISA and Virgo sensitivities. The curves are produced by using the LISA data generated by the tool [17] and the VIRGO sensitivity curve data file available at [13]. For a consistent comparison here the LISA curve is calculated with a signal to noise ratio of 1 and without integration over time.

1.3.5 Geodesic motion of the proof masses and sensitivity goal

It is not difficult to show that at low frequencies the noise limiting LISA sensitivity is acceleration noise, caused by residual stray forces which prevent the free fall of the proof masses along the optical axes of the interferometer. In the weak field approximation, the time varying distance $L(t)$ between two LISA test masses representing the end-mirrors of an interferometer arm satisfies the following equation:

$$\frac{\partial^2 L}{\partial t^2} = \frac{F_x(t)}{m} + L\frac{\partial^2 h}{\partial t^2}, \tag{1.18}$$

where $h(t)$ is the gravitational wave strain, and m is the mass of each mirror ($2\,kg$). The term $F_x(t)$ is the differential force acting on the two proof masses along the optical axis x, which induces a spurious acceleration $F_x(t)/m$. The

related acceleration disturbance is the so called acceleration noise and is described by the power spectral density $\tilde{F}_x(f)/m$, where f indicates the frequency.

According to equation (1.18), the acceleration noise produces a displacement noise $\tilde{x}(f)$ along x, which can mask the effect of a passing gravitational wave and is expressed by:

$$\tilde{x}(f) = \frac{\tilde{F}_x(f)}{m} \frac{1}{(2\pi f)^2} \frac{1}{L}. \tag{1.19}$$

This displacement noise is dominant at low frequencies, owing to the f^{-2} term. This is true even if we assume a frequency independent force noise $\tilde{F}_x$. The acceleration noise rapidly degrades LISA sensitivity below few mHz. Furthermore, it can also worsen the maximum sensitivity floor of LISA at few mHz.

Taking into account the interferometer armlength $L = 5 \cdot 10^{-9}\, m$, in order to achieve the LISA design sensitivity the acceleration noise spectral density must satisfy the following upper limit:

$$\frac{\tilde{F}_x(f)}{m} \leq 3 \cdot 10^{-15} \times \left[1 + \left(\frac{f}{3\, mHz}\right)^2\right] \frac{m}{s^2\sqrt{Hz}}. \tag{1.20}$$

An extremely high quality free fall is thus required, in order to allow LISA to observe the most interesting low frequency sources. The acceleration noise of the test masses due to stray forces must keep below $3 \cdot 10^{-15}\, m/(s^2 Hz^{1/2})$ at low frequencies down to $0.1\, mHz$.

Figure 1.10 shows how different values of the acceleration noise affect LISA sensitivity curve and how a low acceleration noise is crucial in order to detect some of the expected gravitational wave sources.

1.3.6 Some differences between Ground and Space - Time Delay Interferometry

Up to now we didn't go into any detail about how the signals coming from the single arms of LISA are processed and combined. However a real comprehension of the way LISA works cannot be achieved without understanding

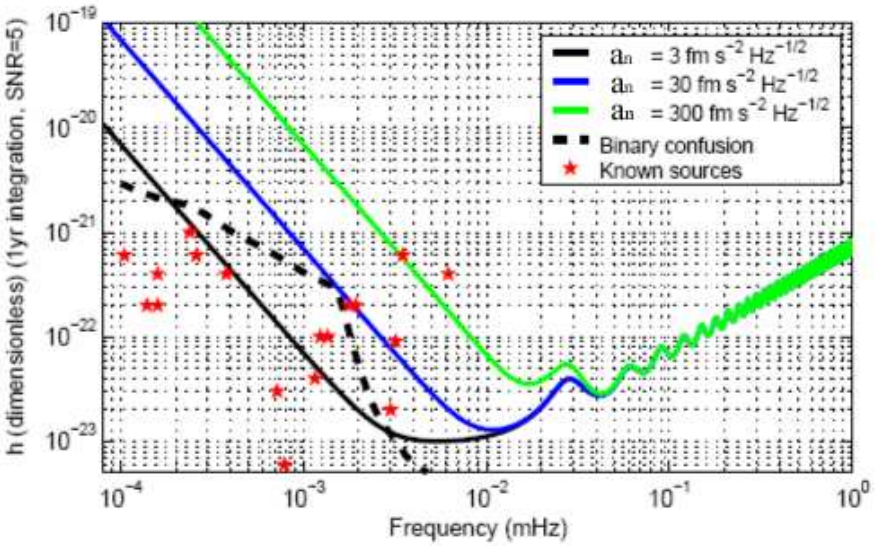

Figure 1.10: LISA sensitivity curve calculated assuming different residual acceleration noise levels a_n on the proof masses [17], for one year integration and signal to noise ratio of 5. The black dashed curve draws the white dwarf binary confusion noise. The red stars represent the amplitude of some of the verification binary signals, which are expected to be emitted from candidate sources with well known parameters.

some very special features concerning its signal processing.

It has been said that LISA can be thought as a Michelson interferometer in space, but this assertion can be quite misleading.

In interferometric ground-based detectors, laser light experiences the same delay in each arm, because of the armlength equality. Thus the phase or frequency noise from the laser precisely cancels at the photodetector, allowing phase measurement many orders of magnitude below the intrinsic phase stability of the laser itself. If this would not happen, detection would be impossible, because raw laser noise is orders of magnitude larger than all other noises.

In contrast with ground-based detectors, it is impossible to keep the arms of a space-based interferometer to be equal. LISA armlengths can differ by a few percent. The laser phase fluctuations experience different delays along each arm, so on each spacecraft the two signals coming from the two different

arms cannot be directly recombined to obtain laser noise cancellation. There is no hope of achieving the desired sensitivity to gravitational waves if laser phase noise is not accurately removed.
Fortunately this serious problem can be solved, as I will discuss further in this paragraph.
Another fundamental difference between space-based and ground-based interferometers is the interferometric detection technique, which is heterodyne for the first detectors and homodyne for the second ones[2].
In LISA each spacecraft sends and receives in turn two laser beams. All the laser beams are offset locked to each other, that means that the laser frequencies are all made different by an offset value (around $10\,kHz$) [15]. This frequency difference is needed to make the heterodyne measurement of the phase of the transponded beam returning from the far spacecraft. Indeed, on each spacecraft the laser light received from each arm is coherently combined at a photodetector with the light from the on board reference laser, and the frequency difference is recorded as a beat signal. Each spacecraft produces two beat signals.
Of course the use of different laser sources, although they are offset locked to each other, complicates further on the problem of laser noise cancellation.
On the other hand, LISA presents another peculiar problem with respect to its terrestrial companions. LISA arms are not only inequal, they are also time-varying. The LISA constellation expands and reduces rithmically and this pulsation causes the spacecraft to move with respect to each other with expected relative velocities of about $1\,m/s$. This means that the laser signals received at each spacecraft are always shifted in frequency by Doppler effect. The expected Doppler shifts are of the order of few MHz for annual orbit corrections and can be kept below tens of kHz at least for two arms by monthly orbit corrections. Of course a shift in frequency can simulate a phase variation due to a passing gravitational wave, so it is necessary to

[2] In the homodyne technique the interfering light beams come from a single laser, while in the heterodyne technique the light beams are produced by different lasers.

rectify the signals by removing Doppler beat notes.

How can the problem of laser phase noise cancellation be solved for LISA? Here I will briefly discuss the simplifying model exposed in [20] [21], which assumes that the six lasers are identical (and so are their frequencies) and that there has been a successful prior removal from the interferometer signals[3] of any Doppler beat notes due to relative motions of the spacecraft. We thus have six residual Doppler time series as the raw data of a stationary inequal-armlength interferometer working with equal lasers[4].
The cancellation of laser phase noise can be obtained by finding a suitable combination of the 6 LISA signals. However, the signals cannot be combined as they are: owing to the considerable armlengths of the interferometer, time-delays related to light propagation have to be taken into account[5].
The resolution relies in properly time-shifting and linearly combining the signals from the interferometer. This technique is called Time-Delay Interferometry (TDI).
As indicated in figure 1.11, the distances between pairs of spacecraft are L_1, L_2 and L_3, with L_i being opposite spacecraft i. The Doppler data stream are denoted by y_{ij} with $i \neq j$: y_{31} is, for example, the Doppler time series derived from reception at spacecraft 1 with transmission from spacecraft 2 [6]. The other Doppler time series are obtained by cyclic permutation of the indices i and j: $1 \rightarrow 2 \rightarrow 3 \rightarrow 1$.
The laser noise of the receiving spacecraft enters the Doppler data immediately at the time of reception, while the laser noise of the transmitting spacecraft enters at a one-way delay time earlier. Denoting the frequency fluctuation noise of the laser aboard the ith spacecraft by $C_i(t)$, the terms

[3] I refer to the two signals produced on each spacecraft by the superposition of the beams received from the far spacecraft with a little part of the light of the local laser.

[4] Actually the analysis taking into account moving spacecraft and inequality of the sources does not present basic conceptual differences with respect to the simplified case and assumes this latter as its starting point. For a complete discussion see [22].

[5] Laser light takes about $17\,s$ to travel through one-way LISA arm.

[6] The present notation allows to cyclically permute indices in subsequent equations.

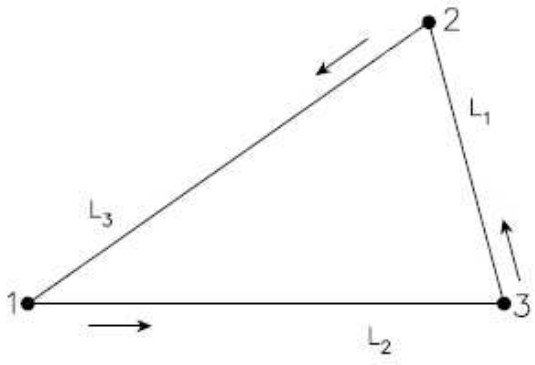

Figure 1.11: Unequal armlength interferometer.

due to laser noise in the six Doppler series can be written as:

$$y_{31}^{laser} = C_2(t - L_3) - C_1(t) \tag{1.21}$$

$$y_{21}^{laser} = C_3(t - L_2) - C_1(t) \tag{1.22}$$

with cyclic permutations of the indices.

The total signal on the spacecraft j relative to the $k \neq j \neq i$ arm is the sum of the gravitational signal, the laser phase noise, the shot noise and the acceleration noise:

$$y_{ij}(t) = y_{ij}^{gw}(t) + y_{ij}^{laser}(t) + y_{ij}^{shot}(t) + y_{ij}^{accel}(t). \tag{1.23}$$

where y_{ij}^{gw} and y_{ij}^{accel} involve propagation delays and geometric features of the setup, while the shot noise has an immediate effect at the time of reception and so the corresponding Doppler variable y_{ij}^{shot} doesn't involve time delays. The laser noises are the dominant terms and need to be cancelled.
It is possible to demonstrate that with independent lasers on two spacecraft laser noise cancellation can be achieved only at some selected Fourier frequencies [20], while with three spacecraft the increased number of Doppler signals allows removal of laser noises at all frequencies.
It is possible to verify by direct substitution that three independent linear combinations of the Doppler data which remove laser noise are:

$$\alpha = y_{21} - y_{31} + D_2 y_{13} - D_3 y_{12} + D_1 D_2 y_{32} - D_1 D_3 y_{23}, \tag{1.24}$$

$$\beta = y_{32} - y_{12} + D_3 y_{21} - D_2 y_{23} + D_2 D_3 y_{13} - D_2 D_1 y_{31}, \tag{1.25}$$

$$\gamma = y_{13} - y_{23} + D_1 y_{32} - D_3 y_{31} + D_3 D_1 y_{21} - D_3 D_2 y_{12}, \tag{1.26}$$

where D_j is a delay operator defined by $D_j y(t) = y(t - L_j)$.
There are many other combinations, which can be found with a systematic method illustrated in [21]. Different combinations have different sensitivities to gravitational waves and to system noises, so it is possible to optimize the combinations for specific cases.
An important combination is the so called fully symmetric Sagnac combination, which is mostly insensitive to gravitational radiation and allows to "turn off" LISA sensitivity to gravitational waves, in order to measure the noise level and discriminate whether a signal is present or not in LISA frequency band.

1.4 Expected Gravitational Wave Sources for LISA

The most important expected LISA sources can be grouped in three general classes: massive black hole binaries, extreme mass-ratio inspirals, and intermediate-stellar mass compact object binaries [18]. Each class of source presents special issues involving data analysis, source simulation, and population synthesis.
For data analysis purposes a more practical classification of the sources is made distinguishing them by the spectral character of their waves. Then we have: periodic sources, chirping sources, complex chirping sources and stochastic sources [23].
Here I will speak in some detail only about the first three groups.
Stochastic gravitational waves are random signals arising from the superposition of many uncorrelated sources, which produce a broadband nearly flat spectrum. Theoretical studies on stochastic sources are very promising but still relatively speculative.

An accurate and complete discussion of LISA scientific objectives is found in [18].

1.4.1 Periodic Sources: Binary Stars in the Galaxy

When LISA will open the eyes on the cosmos, it will be struck by the gravitational radiation emitted by millions of compact binaries from our galaxy. Compact binaries are double star systems in which two compact objects, such as white dwarfs, neutron stars or stellar-mass black holes, orbit each other. Binaries with orbital periods below a few hours emit gravitational radiation in LISA band. Their signal is weak compared to massive black hole binary radiation, but in return their number is extremely high in our galaxy and even in the Solar neighborhood. In the Milky Way there are billions of binary star systems and tens of millions of these are compact.
Several thousands of compact binaries are expected to be detected individually by LISA, allowing for parameter measurement. Among these binaries, there is a number of known systems which are chosen as verification binary stars. From the observation of their electromagnetic spectrum their orbital periods, positions and distances from the Earth are known with good precision. These guaranteed sources will thus appear in the LISA data with predictable and recognizable signals, allowing for verification of the performances of the space detector [24]. Some of these verification binaries are indicated in figure 1.10.
Population synthesis studies show that at low frequencies in LISA band the number of detectable binaries is so high that they form a confused background, in which the single sources are not identifiable. In figure 1.8 the average galactic background is plotted with the black line.
The galactic binary background must be regarded as noise in most cases, because it can overcome the extremely interesting signals emitted by massive black hole binaries, which are in the same low frequency region of LISA band.
Nevertheless the binary background can give precious information on stellar

population and in that kind of studies it is a signal in every respect.
Gravitational wave emission causes the stars to inspiral towards one another, gradually reducing their orbital period and increasing the frequency [23]:

$$f' = \frac{48}{5\pi}\mu M^{2/3}(2\pi f)^{11/3}, \tag{1.27}$$

where μ is reduced mass and M the total mass.
The masses we're talking about are of the order of $1\,M_\odot - 100\,M_\odot$, orbiting each other with periods between 100 and 10000 seconds. At the considered masses and frequencies the chirp is very slow, so frequency remains constant over a mission lifetime. These sources can thus be considered periodic unless we go to frequencies $f \geq 10mHz$ of LISA band, where we find several slowly chirping ones.

1.4.2 Chirping Sources: Massive Black Hole Binaries

Chirping sources emit peculiar quasi-sinusoidal gravitational signals, with frequency and amplitude rapidly increasing with time. As we can infer from equation (1.27) the frequency sweeps across the LISA band only if large masses are involved: the most promising expected sources for LISA are massive black hole (MBH) binaries with total system mass of $10^4\,M_\odot - 10^7\,M_\odot$ and mass ratio of $1/20 - 1$ or so. These sources sweep through LISA band in a time ranging from a few months to a few years and constitute the most powerful gravitational wave sources expected for LISA.
Optical, radio and X astronomy have provided great evidence that nearly all galaxies have MBH in their central nuclei. These are the remnants of galaxy formation. MBH binaries are created by the merger of galaxies and protogalaxies.
According to the studies of galactic dynamics, mergers of MBHs are frequent events in the Universe. Galaxies are continuously forming and growing through hierarchical processes, from the collision of smaller galactic structures.
The predicted rate of MBH mergers takes into account the great number of

galaxies in the present observable volume. Hubble Space telescope observes more than 10^{10} galaxies, and most bright local galaxies show evidence of central supermassive black holes ($M > 10^7\, M_\odot$). From fossil remnants of mergers among local galaxies one can deduce the rate of MBH mergers in the local group, that results to be at least one per year at redshift $z < 1$ [25] [26].

MBH binaries are so powerful sources that LISA will be able to detect them to a wide range of redshifts, back to the first protogalaxies at $z \approx 15$. According to recent studies [27], the rate of detectable MBH coalescences for LISA will be in the range $1 - 1000$ per year.

1.4.3 Complex Chirping Sources: Extreme Mass-Ratio Inspirals

Among the chirping sources a place apart is occupied by the extreme mass-ratio inspirals (EMRI), which are binary systems composed by a MBH and a stellar-mass compact object, with a mass-ratio ranging from about 10^2 to 10^7. Such systems are created by scattering processes in the cores of galaxies. Current estimates suggests that hundreds of these sources will be detectable by LISA each year [28].

The great interest of these sources stands in the fact that they can provide unprecedented insights into the spacetime geometry around MBHs. EMRIs can be accurate instruments for testing Einstein's theory, because they approximate from a physical point of view the ideal sources corresponding to a very special solution of the field equations of General Relativity, the so called Kerr metric [29].

The orbit of an EMRI is quite complex. A strong field black hole orbit has three orbital periods, describing respectively the motion in the axial direction, the poloidal oscillations and the radial oscillations. These periods coincide only in the weak field limit.

An EMRI emits thus a very complex chirping signal, which represents a

recognizable signature of the source.

1.5 The LISA Pathfinder mission

LISA Pathfinder mission aims at testing in space the most challenging technologies required for LISA.
It is an ESA mission, which will fly a European payload, called LISA Technology Package (LTP) and which will host on board also an american instrument, the Disturbance Reduction System, developed for NASA by the Jet Propulsion Laboratory in Pasadena.
As we already said, the launch is scheduled to take place at the end of 2010.
The experimental apparatus is composed by a single spacecraft, containing two free floating proof masses, identical to the LISA ones, each placed in its own electrode housing. These masses are used as reference masses for a one arm interferometer: it is like having one of LISA $5 \times 10^9\, km$ long arms squeezed down to $35\, cm$, in order to be hosted in a single spacecraft.
LTP contains only one optical bench, on which are mounted the two electrode-housings, analogous to the ones described before for LISA.
As mentioned previously, LISA sensitivity performance is limited at frequencies smaller than few mHz by stray forces perturbing the proof masses free fall trajectories. An extremely high quality free fall is needed: the level of isolation from stray perturbations required to achieve LISA sensitivity must fulfil the condition expressed by equation (1.20). A so demanding requirement has never been reached before in drag-free flight experiments. Verifying the feasibility of LISA drag-free requirements and the performances of the inertial sensor will be one of the fundamental tasks of LTP.
A second task will be the testing of the micro-Newton electric propulsion system, which we mentioned before.
Other fundamental tests that LTP will fulfil concern: the electrostatic actuators used to move the proof masses along the transverse degrees of freedom; the Charge Management System, compensating the net electrical charge de-

posited on the proof masses; the laser interferometry at the level of accuracy envisaged for LISA; the caging and the relaxing mechanism; the endurance of the different instruments and hardware in the space environment.
The successful demonstration of these very challenging technologies will represent a fundamental step towards the most complex and sophisticated LISA mission.

Chapter 2

An Optical Readout for the LISA Gravitational Reference Sensor

The stationariness of the position of each spacecraft around the proof masses is a fundamental issue of LISA. The aim of the Gravitational Reference Sensor (GRS) is to measure the displacements of the spacecraft with respect to the proof masses, providing the signals required by the drag-free control loop in order to readjust the relative position.
The usual solution for satellite drag-free control, adopted as a reference solution also for the LISA GRS, is the usage of capacitive sensors.
The obvious alternative solution is some kind of optical readout (ORO) system; this offers very small back-action and is potentially more sensitive than the capacitive one.
However a capacitive readout system has been already developed and tested on a torsion pendulum by the group of Trento University. It is the baseline inertial sensor that will fly on the LISA Pathfinder for technological demonstration in space. In case of successful flight testing, the capacitive sensor will certainly remain as the reference solution also for LISA.
Nevertheless, the demand for mission risk reduction results in the necessity of a backup solution for the GRS.
The development of an ORO system to be integrated in the present design

of the GRS is what my thesis work mainly concerned.
In this chapter I will describe the drag-free control of LISA and the GRS. I will illustrate the capacitive sensor performances obtained in Trento with the one mass torsion pendulum facility. Finally I will introduce our proposal for an ORO system, discussing its main advantages and making some analysis of the requirements for LISA and the expected model noises.

2.1 LISA Drag-Free Control and the GRS

One of the fundamental tasks of the spacecraft is to shield the proof masses from external perturbations, which can cause them to move and induce phase-signals appearing as gravitational waves. Such perturbations can be of many kinds: solar radiation pressure, solar wind, small particles moving across space.
This means that, while the two proof masses are freely floating, different external forces will be acting on the spacecraft, spoiling its geodesic motion and preventing it from correctly following the proof masses free fall. In the extreme case the spacecraft could hit the proof masses.
It is thus necessary to measure the relative position in order to control it. The measurement is made by an inertial sensor system called GRS.
Due to the fact that the proof masses are rotated of an angle of 60° with respect to each other, the spacecraft can be kept centred on the proof masses only by means of two different mechanisms. Along the main interferometer axes the position correction is obtained by moving the spacecraft. This is done with the already mentioned ion-emitting microthrusters. Along the transverse directions, instead, electrostatic actuators mounted on the electrode housings act directly on the proof masses.
Microthrusters and electrostatic actuators are both driven by the signals generated by the GRS. GRS, thrusters and electrostatic actuators constitute the so called drag-free control loop of LISA.
The proof masses represent at the same time the reference mirrors of the

interferometer and the inertial references for the drag-free control of the spacecraft. However, the electrostatic actuation prevents the mirrors to be in free fall along the transverse DOFs in the loop band-width. Furthermore the mirrors are forced by the servo-loop to follow the intrinsic noise of the position sensor.
The residual motion between the spacecraft and its proof masses must be reduced as much as possible. In this way, besides the cross-coupling noise which I'll analyse in next subsection, also the force disturbances due to spacecraft self-gravity and other relative position dependent perturbations are minimized.

2.1.1 The problem of cross-couplings

If the alignment between sensors and mirrors were perfect and there were no cross-couplings between the different DOFs, the sensor noise would be reproduced only along the transverse DOFs, while the mirrors inertiality would be kept safe along the intererferometer axes, which are the directions involved in the gravitational radiation strain measurement. There would be no problem in this case.
Unfortunately cross-couplings cannot be reduced to zero and thus the sensor noise couples the proof mass displacements also along the optical axes. In order to achieve LISA sensitivity, the cross-couplings must be kept below a certain treshold, which depends on the noise level of the inertial sensor, as we will discuss further.
The maximum acceptable cross-coupling noise is readily calculated taking in account the design sensitivity of LISA. As we saw in the previous chapter, the noise sources that limit the antenna sensitivity are laser shot noise in high frequency and acceleration noise in the low frequency region. The position noise curve behaves like $1/f^2$ in low frequency and then becomes white noise in high frequency, with a corner at about $3\,mHz$. The white noise has an expected value of $4 \cdot 10^{-11}\, m/Hz^{1/2}$ [15].
Assuming that the residual cross-coupling position sensing noise $\tilde{y}_s$ is the

same for every proof mass and for every DOF and that the noises add incoherently, furthermore taking in account two transverse DOFs for each mirror and two mirrors per arm, we get an upper limit for the noise introduced by cross-couplings in the drag-free servo loops:

$$\sqrt{\tilde{y}_s^2 + \tilde{y}_s^2 + \tilde{y}_s^2 + \tilde{y}_s^2} \leq 2 \cdot 10^{-11} m/Hz^{1/2} \Longrightarrow \tilde{y}_s \leq 10^{-11} m/Hz^{1/2}. \quad (2.1)$$

Introducing a safety factor of 10, we obtain a generally accepted upper limit of:

$$\tilde{y}_s \leq 2 \cdot 10^{-12} m/Hz^{1/2} \qquad \text{above } 3\,mHz, \quad (2.2)$$

while the specification is relaxed as f^2 below the corner frequency. This can be expressed by a more general relation, which is valid at all frequencies f:

$$\tilde{y}_s \leq 2 \cdot 10^{-12} \sqrt{\left[\left(\frac{3\,mHz}{f}\right)^2 + 1\right]^2} \qquad [m/Hz^{1/2}] \quad . \quad (2.3)$$

Summing up, in order not to spoil the required inertiality of the floating proof masses along the optical axes, the position sensing noise coupled to the main DOFs of the interferometer by means of the electrostatic actuation on the transverse DOFS must not overcome $2 \cdot 10^{-12}\, m/Hz^{1/2}$ above $3\,mHz$ [1]. The previous reasonings show that the precise centering and the stationariness of the spacecraft around the mirrors along the interferometer axes is crucial in order to achieve LISA sensitivity.

2.2 The Capacitive Sensor

2.2.1 Main features

The reference solution for LISA GRS is based on capacitive sensors. The basic principle is to use a plane parallel-faced capacitor, where one of the plates

[1] Notice that we have discussed the problem in terms of the displacement sensitivity of LISA. An equivalent point of view is to consider the acceleration noise induced by the drag-free control loop on the proof masses along the optical axis and remember that it must fulfil the upper limit expressed by equation 1.20.

is the surface of the test mass while the other one is set on the electrode housing and thus is integral with the spacecraft.
The current GRS design has been developed at Trento University and has been tested experimentally on a single mass torsion pendulum facility in Trento laboratories [30] [36] [37] [38].
The sensor is made up of a suitable geometrical configuration of plane condensers, as illustrated in figure 2.1 [39] [40]. Six pairs of electrodes are mounted on the electrode housing surrounding the proof mass.

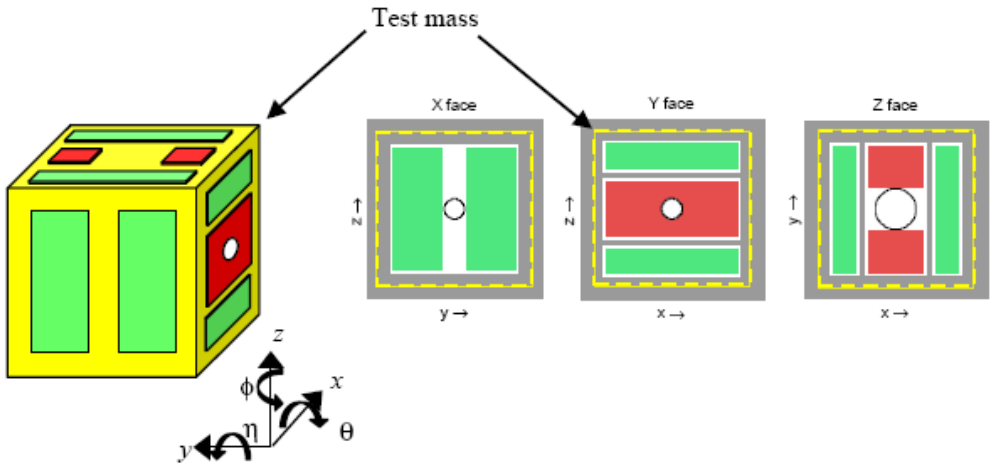

Figure 2.1: Capacitive Sensor scheme for the single mass torsion pendulum facility in Trento. The test mass, represented by the yellow cube, is surrounded by the sensing and injection electrodes. On the right, the electrode configuration respectively on the x, y and z electrode housing faces. The x axis is the interferometer/drag-free preferred one. The holes shown in the scheme are for the interferometer laser-light beam (x faces) and for the locking plunger of the caging mechanism (z faces), needed for holding the test mass during the launch phase. Some relevant geometrical dimensions: test mass cubic size $46\,mm$; x sensing electrodes-test mass gap $d = 4\,mm$.

The six readout channels can be linearly combined to reconstruct the test mass displacements in all the six DOFs.
Here I report the results obtained from the tests performed with the single mass torsion pendulum facility in Trento []. A four mass facility has been recently set up for further experimental verifications and will be discussed in

the last chapter of this thesis.
The single mass torsion pendulum is basically consituted of a proof mass hanged by a torsion fiber in a vacuum chamber (see figure 2.2). In this latter the electrode housing surrounding the proof mass and hosting the capacitive sensor is rigidly mounted on a support, which can be moved by a 5 DOF micromanipulator for centering purposes. The facility is equipped with an electrostatic actuation circuitry, which allows the control of the pendulum torsional and tilting modes.

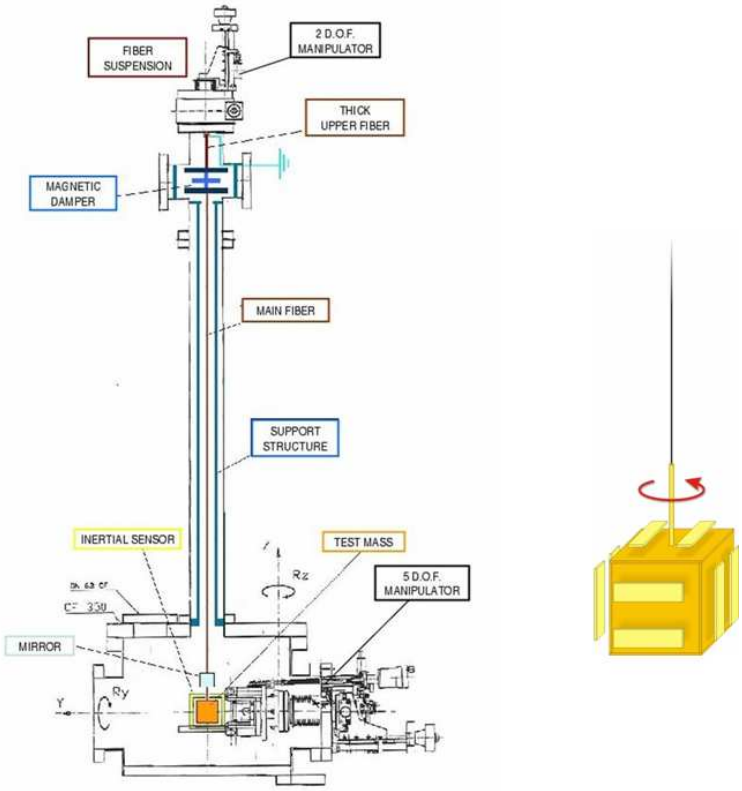

Figure 2.2: Scheme of the single mass torsion pendulum facility in Trento.

The sidelength of the proof mass is $46\,mm$, as it will be in LISA, while the x sensing electrodes-test mass gap is $d = 4\,mm$.

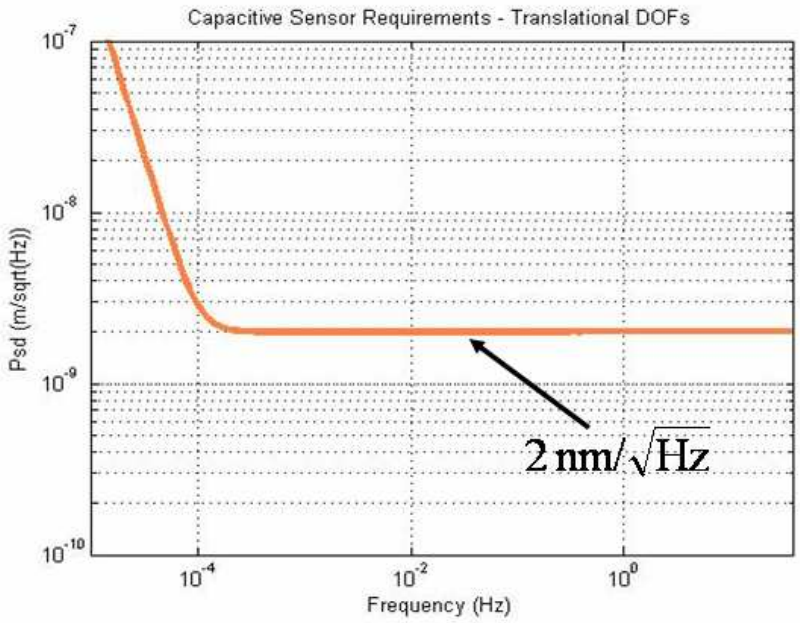

Figure 2.3: Capacitive sensor expected sensitivity to translational degrees of freedom.

Graphs 2.3 and 2.4 show the sensitivity requirements for the capacitive sensor with regard to the translational and the rotational DOFs [15] [30]. The curves represent the model noise level expected for the capacitive sensor and are in very good agreement with the experimental curves obtained with Trento apparatus.
The sensitivity to translational DOFs is of $2\,nm/Hz^{1/2}$ in all the frequency band interesting for LISA, while for rotational DOFs we get a value of $200\,nrad/Hz^{1/2}$.

One of the main disadvantages of capacitive sensors is the need for a very small free gap between the two plates and then between mirror and spacecraft. In order to achieve the sensitivity required for LISA, the gap cannot exceed few millimeters. The small free gap turns out in strong sensitivity to net charges deposited on either the proof mass or the spacecraft. As a consequence the maximum acceptable rate of charge deposition is very demanding and a frequent discharge by UV flash lamps is needed.

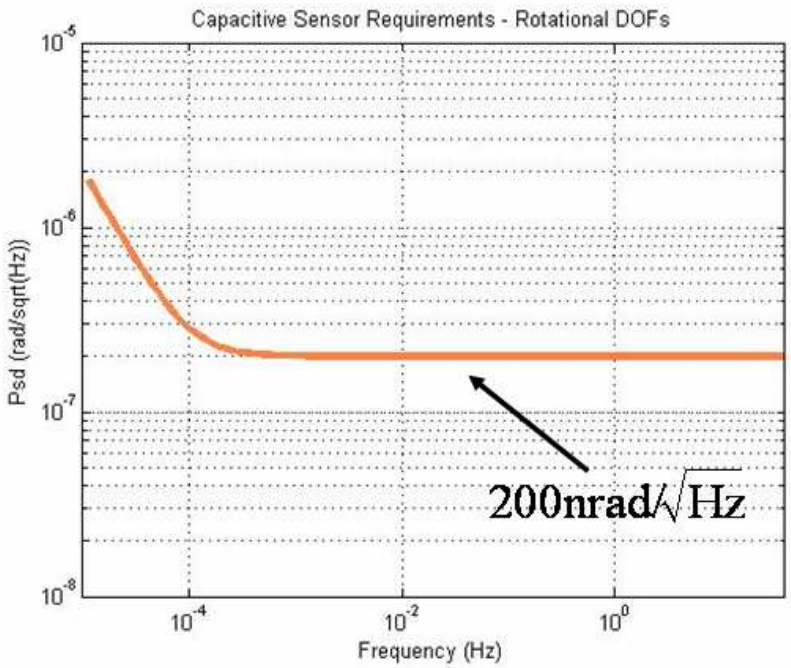

Figure 2.4: Capacitive sensor expected sensitivity to rotational degrees of freedom.

The ground testing facilities pave the way to the tests on the technology demonstration mission LISA Pathfinder, on which the capacitive sensor is planned to fly.

2.2.2 Cross-coupling requirements

Referring to the result obtained in (2.2), we can now estimate the maximum acceptable cross-coupling for the drag-free control loop in the case of the reference solution for the inertial sensor of LISA.
If the upper limit of the noise due to cross-coupling is established by (2.2), the maximum acceptable cross-coupling between different translational DOFs is given by the ratio of $\tilde{y}_s$ and the sensitivity of the capacitive sensor to the translational DOFs:

$$\frac{\tilde{y}_s}{\text{GRS sensitivity}} = \frac{2 \cdot 10^{-12} m/Hz^{1/2}}{2 \cdot 10^{-9} m/Hz^{1/2}} = 0.001. \tag{2.4}$$

The cross-coupling of the transverse DOFs to the main interferometer axis must be of the order of one part per thousand. It is worth of noting that the requirement holds in the frequency interval where LISA is limited by position noise, while it can be relaxed as $1/f^2$ below $3\,mHz$.
The condition stated above is a very stringent requirement and represents an extremely challenging technological task. Cross-couplings below 0.1% are generally very difficult to achieve in a real system. Usually coupling effects are of the order of few percent. Of course this does not represent an intrinsic limit, but the problem is that cross-couplings are caused by a great number of predictable and sometimes unpredictable mechanisms (machining and assembling imperfections, calibration and centering errors and so on) and keeping them under control is a very difficult job. The difficulties are increased if this job has to be developed for space, as for LISA, where the experimental apparatus is out of reach for possible corrections.
It is clear that any reduction of the readout noise below the specifications in figure 2.3 would give a corresponding relaxation of the requirement for the cross-couplings.
On the other hand, the sensitivity of the capacitive sensor can be further improved only by reducing the free gap between test mass and electrodes, but this would increase unacceptably the sensor back-action (due, for example, to net charges).
The previous reasonings lead naturally to think about an alternative solution for the LISA GRS. This can be found among the optical readout systems.

2.3 The ORO Sensor

The LISA research activity in Napoli concerns the study, development and testing of an optical readout (ORO) system for the inertial sensor of LISA. This activity has started since 200 [30]. I joined it three years ago beginning my phd studies.

2.3.1 Why an ORO Sensor?

In principle an ORO can achieve better sensitivities performances than a capactive sensor, without the problem of reducing the free gaps between proof mass and electrodes. On the contrary an ORO system can work with large gaps and thus can potentially lower the effects due to electromagnetic stray forces. This means that an ORO system would allow a significant noise reduction with negligible back-action.
The replacement of the capacitive sensor with an optical one has been already proposed since a long time and different schemes have been suggested, but none has been developed in detail and experimentally demonstrated in the configuration adapted to flight on LISA.
On the other side, the capacitive sensor developed in Trento is planned to be tested in the LISA Pathfinder mission and it is very likely that, in case of successful test on flight, it will remain as the reference solution also for LISA.
The possibility of replacing the capacitive sensor with an optical one not tested in space environment, even though more performing, has not to be considered.
Nevertheless, as explained earlier, the demand for mission risk reduction states the necessity of a backup solution for the GRS. A further advantage of having an auxiliary sensor is that it can provide extra information on couplings between different degrees of freedom.
In developing an ORO solution for the inertial sensor of LISA our primary goal is thus to provide a reliable instrument to be integrated in the present design of the GRS, in order to substitute the capacitive sensor in case of failure during the mission. This reasoning states that the basic sensitivity requirements for an ORO system are those achieved by the capacitive sensor.
Any further improvement in the sensitivity would relax the extremely demanding constraints on the cross-couplings and would turn out to be very useful in any case, especially if the ORO were adopted as the main sensor

and the capacitive sensor became the backup solution.
However sensitivity and back-action are not the only issues to be taken into account while studying an alternative solution for LISA GRS. The simplicity and reliability of the instrumentation are fundamental requirements as well. Furthermore the ORO must be compatible with the present design of the LISA inertial sensor, so that it can be integrated with minimal modifications of the project.
Keeping in mind all these arguments, we have selected a sensor based on optical levers.
Of course, other kinds of optical sensors are possible. An alternative solution can be some type of interferometric readout. This can perform better sensitivities than an optical lever system, but it is a much more complex device. An optical lever has the advantage of being very simple and thus cheap and reliable, which are fundamental properties for a device planned to work in space. Furthermore, it is worth noting that, at the low frequencies we are interested in, sensitivity is not limited by the intrinsic noise of the sensor, that is shot noise in the case of the optical readouts. Other sources of noise intervene, which are independent from the optical sensor, such as thermal drifts in both mechanics and electronics, as well as other perturbing effects that are not easily identifyable.
For this reason, a simpler ORO solution can be preferable with respect to an interferometric sensor, which is in principle much more sensitive than required, but also presents higher costs and greater complexity.
For further details on proposed interferometric solutions to be integrated in LISA GRS see [31] [32] [33] [34].

2.3.2 The principle scheme of the ORO

The principle scheme of the ORO is very simple. As it is sketched in figure 2.5, a laser beam is sent through a mono-modal optical fiber to the surface of the proof mass. The reflected beam is collected by a detector sensitive to beam position (quadrant photodiode (QPD) or position sensing device

(PSD)). A translation or rotation of the test mass results in a displacement of the light spot across the sensor.

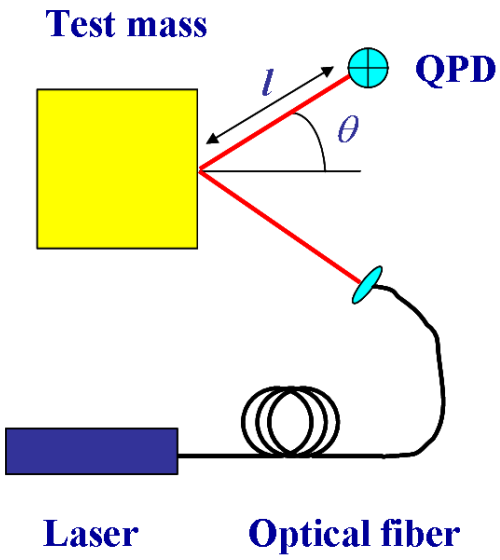

Figure 2.5: ORO's principle scheme: an optical lever. A fiber coupled light source sends a light beam to the surface of the test mass. The position of the reflected beam is read by a position sensor (QPD or PSD). The light beam is collimated and focused by means of a proper fiber output focuser (output fiber coupler). The optical lever's length l and incidence angle ϑ are indicated in the figure.

A translational displacement Δx_{TM} of the test mass causes a displacement Δx_{Ph} of the light spot on the photodetector depending on the incidence angle ϑ as:

$$\Delta x_{TM} = \frac{\Delta x_{Ph}}{sin\vartheta}. \tag{2.5}$$

A rotation of the proof mass relative to a variation $\Delta\vartheta$ of the angle ϑ corresponds to a displacement Δx_{Ph} of the light spot on the photodiode depending on the optical lever armlength l :

$$\Delta x_{Ph} = 2l \cdot \Delta\vartheta. \tag{2.6}$$

With a suitable combination of three sensors, it is possible to recover the

displacements of the proof mass in all six DOFs, as we will see in chapter four.
The single-mode optical fiber is necessary to reduce the beam jitter that would otherwise be dominating.
The photodiodes signals are read by trans-impedance amplifiers, which transform them from current signals to amplified voltage signals.

2.3.3 The expected noise sources of the ORO system

In order to establish if our ORO system can achieve the required sensitivity, it is necessary to model the intrinsic noise sources and calculate the expected noise level for the sensor.
In the frequency band of interest $(0.1-100\,mHz)$ it is possible to identify the main sources of noise of our ORO sensor as the shot noise and the electronic noise of the photodiode amplifier [42]. The other modeled noise sources are negligible at these frequencies.
As for any optical sensor, the ultimate limit is shot noise, which is due the random fluctuation of the number of photons incident on the photodetector per unit of time. This results in a current noise $\tilde{I}_{SN}$ in the measured photodetector current I_{Ph}, which corresponds to a displacement noise described by the formula:

$$\tilde{x}_{SN} = \frac{\tilde{I}_{SN}}{|dI_{Ph}/dx|}, \tag{2.7}$$

where the tilde indicates the power spectral density of the below quantity.
The shot noise $\tilde{I}_{SN}$ is expressed by $\tilde{I}_{SN} = \sqrt{2I_{Ph}e}$, where e is the electron charge. The photodiode current is evaluated in terms of the optical power P_0 of the light beam and of the photodiode responsivity $\alpha(\lambda)$ [2], depending

[2] The responsivity of a photodiode characterizes its performance in terms of the photocurrent generated per incident optical power at a given wavelength [41]:

$$\alpha(\lambda) = \frac{I_{ph}}{P_0}.$$

on the wavelength λ, by means of the relation $I_{Ph} = \alpha(\lambda)P_0$.
The measurement range L is represented by the size of the light spot in case a QPD is used or by the detector size in a PSD setup, as will be shown in next chapter. In this interval the photodiode current ranges from $-I_{Ph}$ to I_{Ph}. The quantity dI_{Ph}/dx in equation (2.7) can thus be reasonably approximated by $dI_{Ph}/dx \approx \Delta I_{Ph}/\Delta x = 2I_{Ph}/L$.
Taking in account these relations and making $\alpha(\lambda)$ explicit in terms of the quantum efficiency η of the photodiode [3], we get:

$$\begin{aligned} \tilde{x}_{SN} &\approx \frac{L}{2}\sqrt{\frac{2hc}{P_0\eta\lambda}} \approx \\ &\approx 1.4 \cdot 10^{-11} \left(\frac{633\,nm}{\lambda}\right)^{1/2} \left(\frac{1\,mW}{P_0}\right)^{1/2} \left(\frac{0.84}{\eta}\right)^{1/2} \left(\frac{L}{1\,mm}\right) \end{aligned} \quad (2.8)$$

$$\text{dimension units} \qquad [\tilde{x}_{SN}] = \left[m/\sqrt{Hz}\right].$$

Notice that the shot noise limited sensitivity of the ORO depends on the light power P_0 and on the measurement range L [4].
It is worth noting that for reasonable values of the light power $(0.1 - 1\,mW)$ in (2.8), the shot noise results negligible in the LISA frequency band.
On the other hand, the current noise I_n of the trans-impedance amplifier used to read the photodiode current imposes a limit displacement sensitivity

[3] The quantum efficiency of a photodiode measures the probability of the conversion process of received photons to free electron hole pairs and is defined as the ratio of the number of free electron hole pairs giving rise to a photocurrent I_{ph} and the number of incident photons [41]:

$$\eta = \frac{I_{ph}/e}{P_0/h\nu}.$$

where P_0 and ν are the power and the frequency of the incident light, while e is the electron charge and h the Planck constant.

[4] The equality (2.8) is a handy way of expressing the displacement noise due to photodiode current shot noise. The value $1.4 \cdot 10^{-11}\, m/\sqrt{Hz}$ of the diplacement noise corresponds to the numerical values of the physical parameters specified in the round brackets. Substituting different desired values for the parameters, in the proper dimension units indicated in the brackets, it is possible to obtain the associated displacement noise.

given by:

$$\begin{aligned}\tilde{x}_I &= \sqrt{N}\frac{\tilde{I}_n(f)}{|dI_{Ph}/dx|} \approx \sqrt{N}\cdot\frac{L}{2\alpha(\lambda)P_0}\cdot\tilde{I}_n(f) \approx \\ &\approx 4\cdot 10^{-10}\left(\frac{0.43\,A/W}{\alpha(\lambda)}\right)\left(\frac{1\,mW}{P_0}\right)\left(\frac{1\,mHz}{f}\right)^{1/2}\left(\frac{L}{1\,mm}\right) \quad (2.9)\end{aligned}$$

$$\text{dimension units} \qquad [\tilde{x}_I] = \left[m/\sqrt{Hz}\right],$$

where we assume $\tilde{I}_n(f) = (5.4\cdot 10^{-12})/\sqrt{f}\,A/(Hz)^{1/2}$, which is the typical value for a widely used device (Analog Devices OP27EP). The quantity N is the number of current signals: $N = 4$ for two dimensionals sensors.
As the shot noise, also the electronic noise depends on the laser power and on the measurement range. However, differently from shot noise, which is white, the electronic noise depends on the frequency f as $1/f^{1/2}$. At the frequencies we are interested in, electronic noise is the expected limiting factor for an ORO based on optical levers, as illustrated in figure 2.6.

In equations (2.8) and (2.9) the noise is expressed in terms of the displacement of the spot on the sensor. To convert this in terms of proof mass displacement, we should insert a factor depending on geometrical configuration ($1/(2sin\vartheta)$, as will be shown in next chapter).
The previous calculations show that our ORO can in principle reach a sensitivity well below $10^{-9}\,m/\sqrt{(Hz)}$ in the whole measurement band of LISA and is then potentially much more sensitive than the capacitive sensor.
However at such low frequencies, besides the intrinsic noise of the sensor other relevant noise sources intervene, as I mentioned before.
Mechanical vibrations and thermal drifts depend on the actual setup and can be reduced using an appropriate rigid mounting and thermal stabilization. Nevertheless they cannot be completely removed. Furthermore for frequencies between $0.1\,mHz$ and $100\,mHz$, that means for periods between $10\,s$ and $10000\,s$, mechanical drifts, creeps and other residual noise sources are difficult to identify and render very problematic the experimental verification of the potential sensitivity of the ORO sensor with a bench-top experiment.

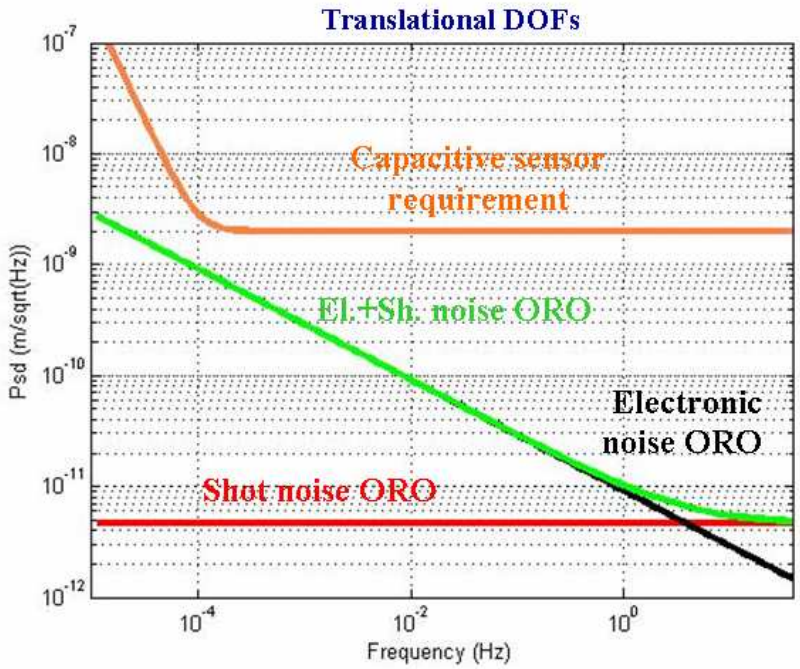

Figure 2.6: ORO's Model Noise. The red line represents the expected shot noise, while the electronic noise is the black curve. The incoherent some of the two, that is ORO's total model noise, is indicated in green. The expected sensitivity for translational DOFs of the capacitive sensor is the orange curve. Electronic noise and shot noise are here calculated assuming the following values for the parameters: $P_0 = 0.2\,mW$, $L = 0.4\,mm$ (spot size), $\lambda = 633\,nm$ (He-Ne laser).

2.3.4 The back-action of the ORO sensor

In section 1.3.5 it has been shown that in order to achieve LISA sensitivity the acceleration noise of the test masses due to stray forces must keep below $3 \cdot 10^{-15}\,m/(s^2 Hz^{1/2})$. This means that for a $2\,kg$ proof mass the power spectral density of stray forces must not overcome the value $6 \cdot 10^{-15}\,N/\sqrt{(Hz)}$.
The force perturbation exerted by the ORO sensor on the proof mass is essentially due to the fluctuations of the incident light power. In order to establish the maximum acceptable laser power noise $\tilde{P}$ of the ORO sensor, we assume for the power spectral density $\tilde{F}$ of the stray forces a conservative upper limit of $\tilde{F} \leq 6 \cdot 10^{-16}\,N/\sqrt{Hz}$.
Remembering that the radiation force F_R and the incident light power P

fulfil the relation[5] $F_R \leq 2 \cdot P/c$, we get the following requirement for the laser power stability of the ORO sensor:

$$\tilde{F}_R \leq 2 \cdot P/c \leq \tilde{F} \Longrightarrow \tilde{P} \leq 10^{-7}\, W/\sqrt{Hz}. \tag{2.10}$$

The condition (2.10) can be achieved by actively stabilizing the laser power.

2.3.5 Research Activities

The research activity I carried out during my PhD studies concerned three main topics.

The first aspect of this work has been the characterization of the sensitivity performances of the ORO sensor in rigid bench-top setups. This activity has been developed in the LISA laboratory of Napoli. Different configurations have been tested, in order to identify the best solution for LISA. Different kinds of light sources, optical fibers, detectors and so on, have been investigated, as will be illustrated in the next chapter.

The second topic consisted in the study and development of a real scale prototype of the ORO for the integration in LISA. In order to do this the engineering model for the electrode housing of LISA Pathfinder mission has been considered as a baseline, in order to analyze the problem of the integration of the ORO in the most realistic configuration available at the moment. This activity and its results are described in chapter IV of this thesis.

The last part of my work has been carried out in collaboration with the LISA group of Trento and concerned the testing of the ORO sensor on a four mass torsion pendulum. The facility in Trento allows to verify the sensitivity and back-action performances of the ORO in a condition as close as possible to free fall for a single DOF. The ground testings on the torsion pendulum will be discussed in chapter V.

[5] Equality is fulfiled in case of normal incidence of the laser beam on the surface of the proof mass.

Chapter 3

The ORO Performances

The aim of the measurement and the analysis described in this chapter is the characterization of the ORO sensitivity performances in rigid bench-top setups. Many different configurations of the ORO have been tested, investigating different solutions for the light sources, the position sensors and the fiber components, in order to improve the sensitivity of the device, reduce the noise level and finally find a suitable configuration to fly on LISA.

3.1 The experimental setup

3.1.1 Inside the box

The rigid bench-top layout we set up for testing the ORO performances is shown in figure 3.1.

The bench is machined from a single block of stainless steel, with interfaces for two fiber couplers and two sensors. The test mass is represented by the small tower in the center and mounts two mirrors on its sides. It can be rigidly fixed on the bench itself or mounted on a translation stage, such as a micrometric screw system or a piezo-electric translator with capacitive control, which allow to move it for calibration. The central structure is fixed to the steel block with screws and the whole assembling is rigidly mounted on an optical bench.

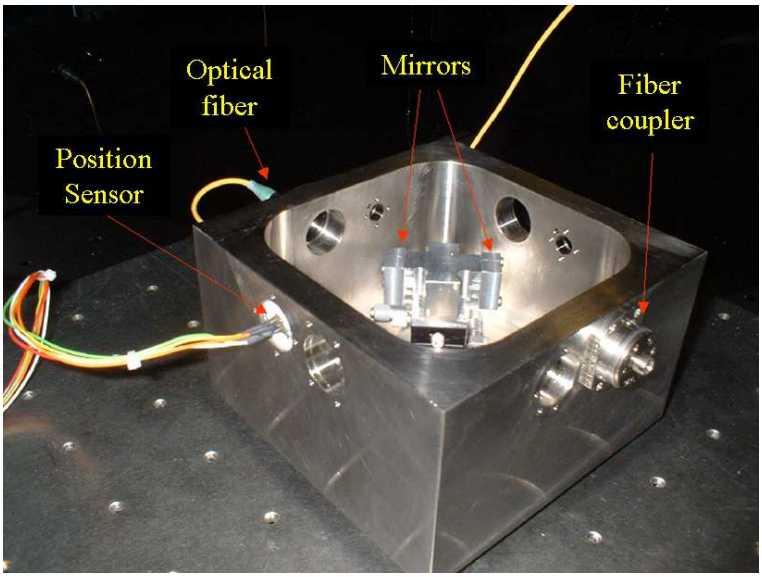

Figure 3.1: Rigid bench-top setup.

The length and the angle of the optical lever are respectively $l = 57.5\,mm$ and $\vartheta = 45°$.

The idea is to have a setup as rigid as possible so that the measured residual motion of the light spot on the photodiode is due to the intrinsic noise of the sensor itself, rather than to actual motion of the test mass.

As it is possible to see from figure 3.1, the setup is symmetric for differential measurement: there are two opposite optical paths, each of which corresponds to a different light beam outgoing from the relative fiber coupler, reflecting on the mirror and being collected by the relative detector. In figure 3.1 only one ORO sensor is mounted on the bench.

The whole setup is closed in a box to avoid air flows and other external disturbances. Initially we had at our diposal only a black plexiglas box. Then we earned a very simple thermally insulated box made up of expanded polystyrene. We lined the inside with common aluminium foil, in order to further reduce thermal variations.

A temperature sensor attached to the steel block monitors the thermal variations inside the box.

Assuming an asymmetry of $0.2\,mm$, due to machining tolerances, and a thermal expansion coefficient for steel of $\alpha \approx 2 \cdot 10^{-5}$ we get, in presence of a temperature fluctuation δT, a displacement noise $\delta x \approx 4 \cdot 10^{-9} \cdot \delta T$. By assuming fluctuations amplitude of $10^{-2} K/Hz^{1/2}$ with a white spectrum in the whole band, it should be possible to go down to the intrinsic noise of the sensor.

Beyond the numerous measurement with the rigid setup, some tests have been accomplished with a real scale bench-top prototype reproducing the layout for integration of the ORO on Trento torsion pendulum. This setup is described in subsection 3.3.7.

3.1.2 Outside the box

Inside the box is closed the rigid steel setup, with the test mass tower, the fiber couplers and the position sensors assembled on it. What does our apparatus look like outside the box? The light sources, comprehensive of their thermal controlers and power supply are positioned outside and so are the amplifiers of the photodiodes, included the direct voltage generator providing them power supply.
The picture is completed by the digital acquisition system. The measurement described in this chapter have been performed with a four channel FFT analyser (ONO SOKKI).

3.1.3 About the tests

The tests I carried out concerned different devices:

- **Light Sources** $\longrightarrow$ He-Ne Laser ($\lambda = 630\,nm$), Laser Diode ($\lambda = 830\,nm$), Super Luminescent Light Emitting Diode ($\lambda = 830\,nm$);
- **Fiber components** $\longrightarrow$ SM (single mode) and PM (polarization mantaining) optical fibers, Fiber output Couplers: aspheric micro-lenses,

graded index lenses;

- **Sensors** $\longrightarrow$ Quadrant Photodiode (QPD), Position Sensing Device (PSD).

The system has been also tested with a Faraday insulator, inserted at the output of the laser in order to reduce the light reflected back to the laser along the fiber, which perturbs the laser's stability.
A study of the influence of temperature variations on the ORO system has also been carried out. Furthermore the apparatus has been tested in vacuum for some time.
It is worth of noting that we are interested in the LISA frequency band, which means that our measurement must last from several ours to several days in order to investigate the noise level of the ORO sensor in the band ranging from $10^{-4}\,Hz$ to $10^{-1}\,Hz$. At the extremely low frequencies we deal with, it is very difficult to control the experimental conditions for carrying out repeated measurement. Tests made up in different days and with identical setups have often lead to different results in the sensitivity performances of the ORO. Furthermore at such low frequencies the identification of noise sources reveals to be a very challenging task.
The most relevant results of the bench-top measurement are shown in section 3.3.

3.2 The measurement procedure

3.2.1 The signals

Each QPD amplifier has seven outputs: four of them are the single voltage signals from each quadrant of the photodiode, and the other three are special combinations of the four quadrant signals. The single quadrant outputs have been used only for checking purposes.

Referring to figure 3.2, we call V_1, V_2, V_3 and V_4 the four quadrant signals

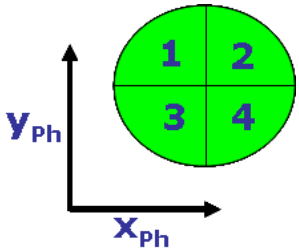

Figure 3.2: Sketch of a quadrant photodiode.

and the recombined signals are:

$$S = V_1 + V_2 + V_3 + V_4 \qquad [Volts] \tag{3.1}$$

$$H = V_1 + V_3 - (V_2 + V_4) \qquad [Volts] \tag{3.2}$$

$$V = V_1 + V_2 - (V_3 + V_4) \qquad [Volts] \tag{3.3}$$

which represent the voltage signals corresponding respectively to the total optical power incident on the photodiode, to the horizontal and vertical positions of the light spot with respect to the center of the QPD.
The signals to be acquired are thus the photodiode signals S, H and V and the temperature T. Other useful signals are the capacitive signals from the piezoelectric translators, when in use, which give the voltage displacements of the test mass as measured by the piezoelectric capacitors. These signals can be calibrated to give the proof mass displacement in metres, using the calibration factor indicated on the instrument data sheets ($0.5001\,V/\mu m$).
Of course for the measurement in vacuum chamber another signal to be acquired is pressure.

3.2.2 Acquisition and preliminary signal processing

The parameters we have to indicate in order to start up the acquisition with the ONO SOKKI are the number of samples N and the sampling frequency f_s, which is related in this instrument to the frequency range by the relation $FrequencyRange = 2.56 \times f_s$. Furthermore it is necessary to establish a suitable measurement range for each acquisition channel, with the purpose of

exploiting the dynamics of the instrument with an eye to possible saturation of the channels.
The acquired signals S, H, V are each one a digital time series made up of N samples with sampling frequency f_s. The signals are transfered to a PC and are processed with Matlab software. The first thing to do is to verify that no channel has saturated the measurement range during the time of acquisition. Drifts in the horizontal and vertical signals can easily cause saturation over the long periods of our measurement.
The contribution of the laser power fluctuations to horizontal and vertical signals can be cancelled out by normalizing H and V to the sum signal S (see figure 3.5). The normalized time series H_N and V_N constitute the data to be furtherly processed.
It is worth noting that we are interested in making a study of the noise level of our ORO sensor, which means that we have to deal with the power spectral density of the horizontal and vertical photodiode signals. As already done in section 2.3.3, we indicate the power spectral density of a discrete time series y with $\tilde{y}$.

3.2.3 The calibration

Once we get the horizontal and vertical normalized signals in normalized volt units, we can transform them in meters, in order to have the time stream of the light spot displacements along the axes of the photodiode or the time stream of the proof mass displacements. The calibration factor which allows to translate the normalized voltage signals in the meter diplacements of the light spot is the photodiode calibration factor C_{Ph}, defined by:

$$C_{Ph} = \frac{\text{Normalized Photodiode Signal}}{\text{Light Spot Displacement}} \qquad [m^{-1}]. \tag{3.4}$$

Actually the calibration factor we can measure is C_{TM}, defined as:

$$C_{TM} = \frac{\text{Normalized Photodiode Signal}}{\text{Test Mass Displacement}} \qquad [m^{-1}], \tag{3.5}$$

from which we can calculate the proof mass displacements corresponding to the time signals H_N and V_N. The two calibration factors are related by geometrical means. From figure 3.3 it is possible to see that the diplacement

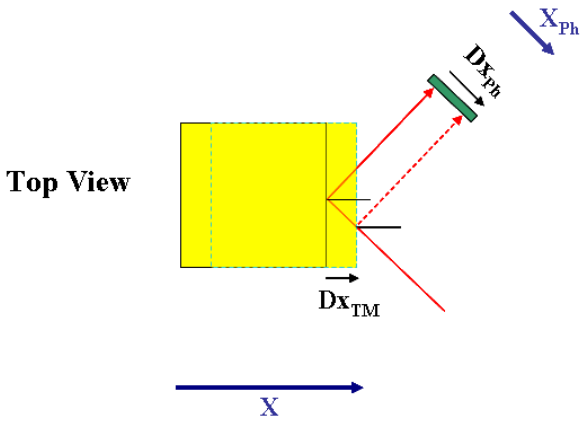

Figure 3.3: Test mass diplacements versus light spot displacements.

Dx_{TM} of the test mass corresponds to an horizontal displacement Dx_{Ph} of the spot on the photodiode, by means of the geometrical relation:

$$Dx_{Ph} = 2sin(\vartheta) \cdot Dx_{TM} = \sqrt{2} \cdot Dx_{TM}. \tag{3.6}$$

Correspondingly, the two calibration factors are related as:

$$C_{Ph} = \frac{C_{TM}}{2sin(\vartheta)}, \tag{3.7}$$

where ϑ is the angle of incidence of the light beam on the mirror attached to the proof mass. In our rigid setup $\vartheta = 45°$. This means that for this ORO configuration the two calibration factors satisfy: $C_{Ph} \equiv \frac{\sqrt{2}}{2} C_{TM}$. The test mass displacements are obtained with a micrometric screw translator or with a piezoelectric device, which allow to move the mass along the diagonal of the steel block (translation axis). The translation causes the light spot to move along the horizontal axis of the photodiode: we assume reasonably that the calibration factor has the same value for both the axes of the detector. We thus position the mass so that the light spot is approximately centered

on the sensor, with $H \approx 0\,V$ and $V \approx 0\,V$. In the case of the micrometric screw translator, the method we adopted was to move the test mass of $60 - 70\,\mu m$ by steps of $10\,\mu m$, starting from an extreme position: the light spot translates correspondingly along the horizontal axis, moving from negative to positive values of H or viceversa (see figure 3.4). For each step we

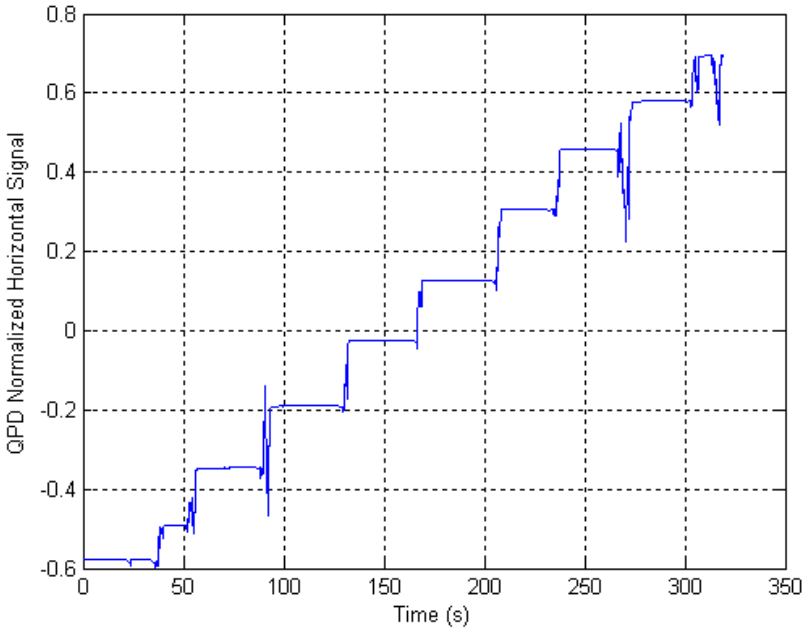

Figure 3.4: Test mass step diplacements obtained with the micrometric screw translator. Each step is $10\,\mu m$ wide.

can calculate the calibration factor as the ratio of the difference between the corresponding values H_N^i and H_N^{i+1} and the step itself ($10\,\mu m$). These values generally differ by few percents. The final calibration factor is estimated as the medium value among these previous values.

A more accurate way of calculating the calibration factor is to use the piezoelectric translator and to induce periodic back and forward translations of the proof mass along the diagonal of the steel block. This is done by driving the piezo with an external sinusoidal signal having appropriate amplitude and frequency. Correspondingly the light spot will go back and forward along

the horizontal axis and the time series H will be a sinusoidal signal. In this way with a suitable number of periods we can calculate the calibration factor from the ratio of the power spectral density of the piezoelectric capacitive signal, previously calibrated in metres, and the power spectral density of H_N: the calibration factor is given by this ratio calculated at the modulation frequency f_{sin}. In fomula:

$$C_{TM} = \left(\frac{\tilde{H}_N}{\tilde{S}_{PZT}} \right)_{f_{sin}}, \tag{3.8}$$

where S_{PZT} is the displacement (μm) of the test mass read by the capacitive sensor of the piezoelectric (sinusoidal signal) [1].
Finally the displacements Dx_{Ph} and Dy_{Ph} of the light spot along the axes of the detector can be obtained as:

$$Dx_{Ph} = \frac{H_N}{C_{Ph}} \qquad [m], \tag{3.10}$$

$$Dy_{Ph} = \frac{V_N}{C_{Ph}} \qquad [m]. \tag{3.11}$$

The displacement of the test mass along the translation axis of the setup is:

$$Dx_{TM} = \frac{H_N}{C_{TM}} \qquad [m]. \tag{3.12}$$

3.2.4 Calibration and Sensitivity of the ORO

The bigger are the calibration factors C_{Ph} and C_{TM}, the more sensitive is the ORO system, because it means that for a same displacement the response

[1] There is another equivalent way of calculating the calibration factor, which will be used in next chapter:

$$C_{TM} = \left| \frac{FFT(H_N)}{FFT(S_{PZT})} \right|_{f_{sin}}, \tag{3.9}$$

where we have indicated with FFT the fast Fourier transform. This calculation returns modulus and phase, this latter providing the sign of the calibration factor. For the tests described in this chapter the sign has no importance. In the next chapter more degrees of freedom will be considered and the phase will be relevant for the sign attribution of the elements of the calibration matrix.

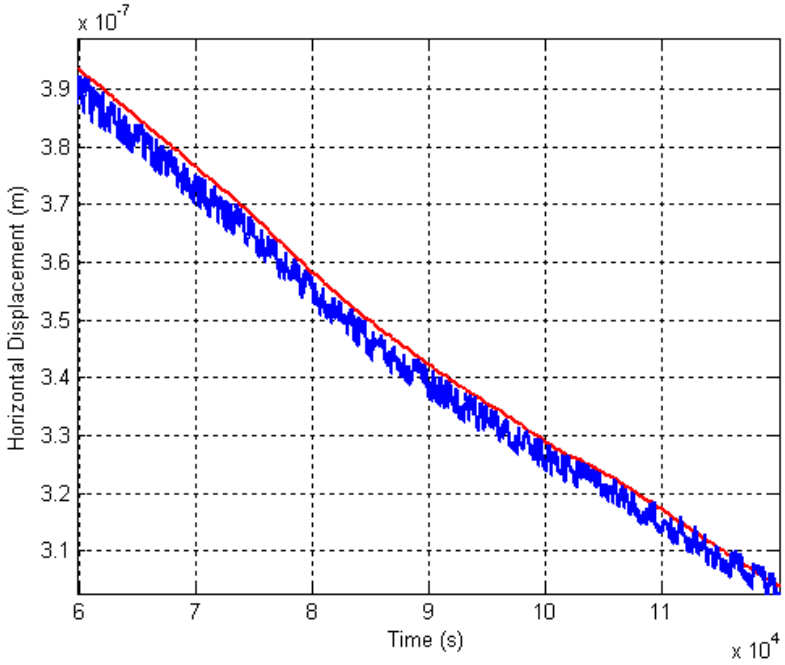

Figure 3.5: Comparison between normalized (red) and not normalized (blue) displacement signal. The normalization cancels the laser power fluctuations.

signal is greater. In particular, given the calibration coefficient of the photodiode C_{Ph}, C_{TM} increases with the angle of incidence of the light beam. So proof mass displacement sensitivity increases with the angle of the optical lever.

Another important consideration is that the sensitivity of an ORO sensor depends on the light power of the laser and on the measurement range of the detector. This is shown in the equations (2.8) and (2.9), where the modeled noises expected for the ORO, shot noise and electronic noise, are expressed in terms of the parameters of the ORO device. In particular ORO's model noise is inversely proportional to light power and directly proportional to the measurement range.

In the case of a quadrant photodiode (QPD) the measurement range is equal,

in good approximation, to the size of the light spot [2]. A gaussian beam with a diameter d corresponds to a measurement range of $2 \cdot \frac{d}{2} = d$, as it is easily understood from figure 3.6.

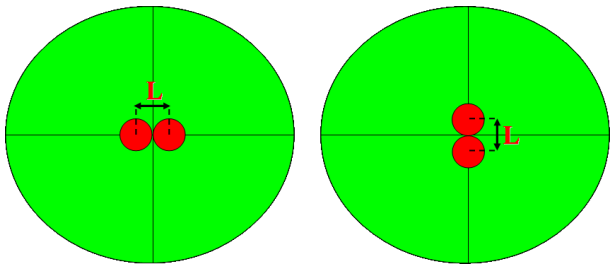

Figure 3.6: Measurement range of a quadrant photodiode. The red circle represents a gaussian light spot in the extreme positions of the photodiode measurement range.

The smaller is the spot, the smaller is the measurement range. This means that under the same conditions (laser power, angle of the optical lever) and for a same proof mass displacement we get a greater response signal when the light spot is smaller. A way to visualize this is that the H and V signals range between the same values but for a smaller displacement range of the spot on the detector: the calibration factor C_{Ph} increases and so does C_{TM}. In order to increase the ORO sensitivity we can thus use very collimated beams. On the other hand we have to take into account that the increase in sensitivity is obtained reducing the measurement range: the displacement range of the proof mass is reduced too and this of course can be a problem. We must play attention to this point when we collimate the laser beam.
It is worth noting that in case a QPD detector is used, every time we change the collimated beam size, it is necessary to calculate the new calibration factors.
In our measurements the typical value of the spot diameter is $400\,\mu m$.

[2] The approximation consists in the fact that the cross dividing the four quadrants is an insensitive area. The QPDs chosen by us have a usable area of $3\,mm \times 3\,mm$, in which the insensitive cross about $100\,\mu m$ wide doesn't contribute to the measurement range. It is worth noting that when the spot is perfectly centerd on the QPD, the signal S undergoes a drop, especially if the spot size is comparable with the width of the insensitive cross.

On the other hand the measurement range of a position sensing device (PSD) is defined by the dimensions of the detector. This means that generally a PSD shows lower sensitivity than a QPD.

3.3 The measurement

In this paragraph I describe the main measurement campaigns performed in order to test the ORO sensor with different experimental configurations. References [42] [43] [30] report the first studies on the ORO sensor and the first experimental results, obtained with a bench-top setup with elements mounted separately on the optical bench. This analysis was done before I joined the group and I won't enter in any detail about it, referring to the relative articles. I will only show a comparison between the noise level of those first measurement and the one obtained during the first campaign on the rigid setup (see figure 3.17).

As it has been said before, measurement at the very low frequencies we are interested in take very long time, each lasting several hours, or days (up to one week). If we want to go down to $0.1\,Hz$ or below, many samples are needed for averaging in order to improve the accuracy. Furthermore, any change in the setup requires opening the thermal insulation box and some time is thus required to get again a stable and uniform temperature, before we can start a new measurement. So it is generally not so easy to be sure that in comparative experiments all the experimental conditions are the same: in some cases it is easier to identify the setup which gives a good sensitivity rather than rule out, without doubt, the one giving not completely understood troubles.

All the different setups generally show measurable differences only at very low frequencies, while they normally give similar results for frequencies above a few Hz (where the device is generally limited by readout electronic noise and mechanical vibrations). This results in the fact that we cannot use high

frequency measurement (which would be much faster) to extrapolate low frequency behaviour.

3.3.1 Quadrant Photodiode or Position Sensing Device

As we mentioned in the second paragraph, once fixed all the other parameters in equation (2.8) and (2.9), the sensitivity is inversely proportional to the measurement range (L), that is the spot size [3] in the case of the QPD and the detector size for the PSD.
As expected, in our measurement the best sensitivity results were achieved with the QPD, that we adopt as the reference solution for our ORO.
The PSD offers the advantage that the response is not depending on spot size and shape and so it is more stable in time, while for the QPD any change in spot size requires a new calibration and the shape of the spot can affect the measurement.
An interesting aspect is connected to the presence of the photodiode window. In our first experiments, performed with He-Ne laser, we observed, for frequencies below few tens of mHz, an extra unexplained noise with a time varying spectrum (non stationary spectrum). This effect disappeared when we removed the window from the photodiode, so we interpreted it as due to the presence of interference fringes across the spot, due to multiple reflections in the window itself. Any change in the fringe pattern can result in a change of the spot's barycenter and is read as a beam displacement. In practice, in our device the position signal is proportional to the light power, while the noise connected to the window is proportional to the light phase, as happens in an interferometer. For all the following measurement we always used windowless photodiodes, but we think that by using short coherence sources (SLEDs) this effect should become negligible. We didn't check this point yet, but we plan to devote dedicated tests.

[3] By spot size I mean the diameter of the spot.

3.3.2 Fibers and fiber components

Before describing the measurement with the different light sources it is useful to give some detail about the fibers and the fiber components tested in the ORO system.
In general we have adopted SM fibers in order to get a good and stable beam quality and to filter out beam position and angular jitter that would otherwise be dominating for a free space sources.
As a rule, we used only angle polished connectors in order to get a low back-reflection.
We have tested both SM and PM (polarization maintaining) fibers, with or without Faraday Insulators inserted along the optical paths.
We also tested, as fiber output focusers, aspherical micro-lenses and graded index lenses. In the latter case the spot size was typically about $0.4\,mm$.
For the He-Ne laser we got the best sensitivity measurement with PM fibers, while we coundn't find any significant indication that the Faraday insulator was giving any improvement. For what concerns the output couplers, the sensitivity performances with GRIN lens were poor. We think that this is due to the bad beam quality, confirmed by visual inspection by projecting the beam on a far screen, but we cannot assert if this is a general problem or is due to the specific components we tested.
The LD measurement were always dominated by the noise due to mode hopping, so that we couldn't get any information about the fiber optic components.
In the end, the SLED measurement provided stable and reproducible results with no evidence of differences between using SM or PM fibers. In this case we only used aspherical micro-lens collimators for the time being, but we plan to repeat tests with graded index as well.
An important thing to point out is that fiber components planned to work on LISA must have small dimensions. Furthermore they should be compact and the most simple as possible. Taking in account these requirements, the reference solution for the fiber focusers must be chosen among the pigtail

style fiber collimators, which can be found on the market either in the aspherical micro-lens or graded index versions.
These focusers are integrated in the fibers, as it is for the usual graded index collimaters, so that the fiber end shows a cilindrical bulge, the so called *ferrula*. The bulges can have different diameter and length. The graded index focusers we tested were very small, with a diameter of $2.5\,mm$, dimensions that fit the tiny spaces available on the spacecraft. However, these collimaters have shown to be extremely delicate, thus certainly not suited to space operation; furthermore, as already mentioned, they didn't give successful results. On the other side, a pigtail aspherical micro-lens collimator with $3\,mm$ diameter has been tested with the SLED source, showing very good sensitivity performances. This solution has been adopted for the test on the torsion pendulum in Trento, as will be said later on.
It is worth noting that, differently from the traditional adjustable fiber couplers, which can be fixed to the relative support with screws, the pigtail collimaters need suitable holders to be adapted to the interfaces of the support. We have designed, developed and tested different kinds of holders for the ferrulas (with circular and triangular hole sections) and tried different fixing strategies, by glueing the ferrula to the holder or by tightening it delicately with a screw pressure. Actually the best solution seems to be to fix the collimator in between two cilindrical grooves, with the top groove pressing on the ferrula by means of two screws on its sides screwing in the bottom groove. As will be shown later, this is the solution adopted for the ORO torsion pendulum setup.

3.3.3 He-Ne Laser Source

The first type of source used to test the ORO has been a fiber coupled He-Ne laser ($\lambda = 633\,nm$), with a single longitudinal mode and power or frequency stabilization. The VIRGO laboratory in Napoli was already equipped with a certain number of these lasers, so it was a natural preliminary choice.
Figure 3.7 shows the time evolution of the test mass diplacements Dx, during

a measurement lasting 200000 s. The measurement refers to the following experimental features: He-Ne laser ($P_0 = 0.2\,mW$); PM optical fiber ($\lambda = 633\,nm$); aspheric micro-lens collimator ($\lambda = 633\,nm$, spot size= $0.1\,mm$); fiber coupled Faraday insulator ($\lambda = 633\,nm$, attenuation); windowless QPD (Responsivity= $0.45\,A/W$); test mass mounted on micrometric translator ($C_{TM} = 13000\,m^{-1}$); plexiglas box. Figure 3.8 shows the corresponding time evolution of temperature: as it it possible to see from the comparison with the displacement graph, temperature and displacement have very similar trends.

Also the relative spectrums, illustrated in figures 3.9 and 3.10, present

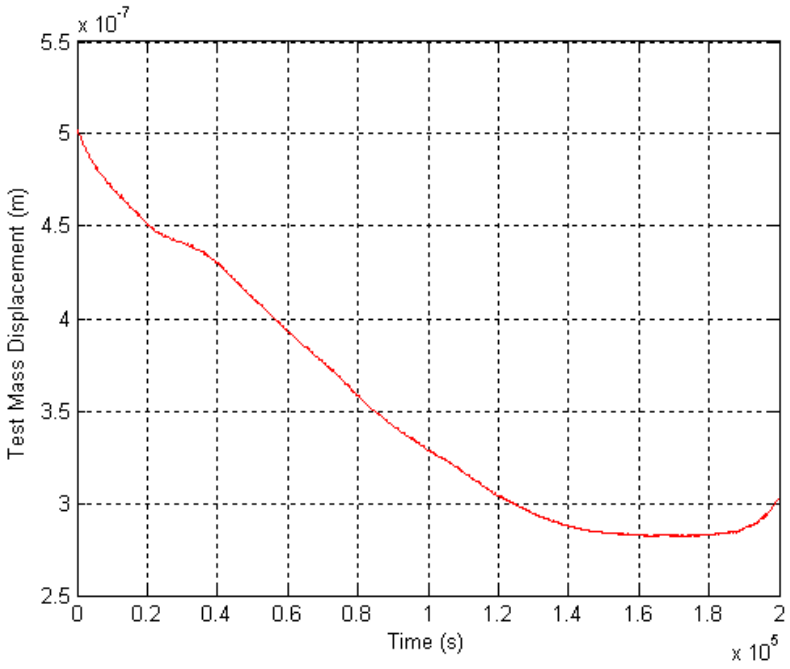

Figure 3.7: Time evolution of test mass displacement (He-Ne setup).

common features, as the peaks around $0.7\,mHz$.

Figure 3.9 shows the spectrum corresponding to the same setup described above but with a graded index fiber focuser ($\lambda = 633\,nm$, nominal spot size= $0.4\,mm$). The noise level is considerably higher than the one obtained with the aspheric micro-lens coupler.

In order to estimate the angular noise corresponding to the displacement

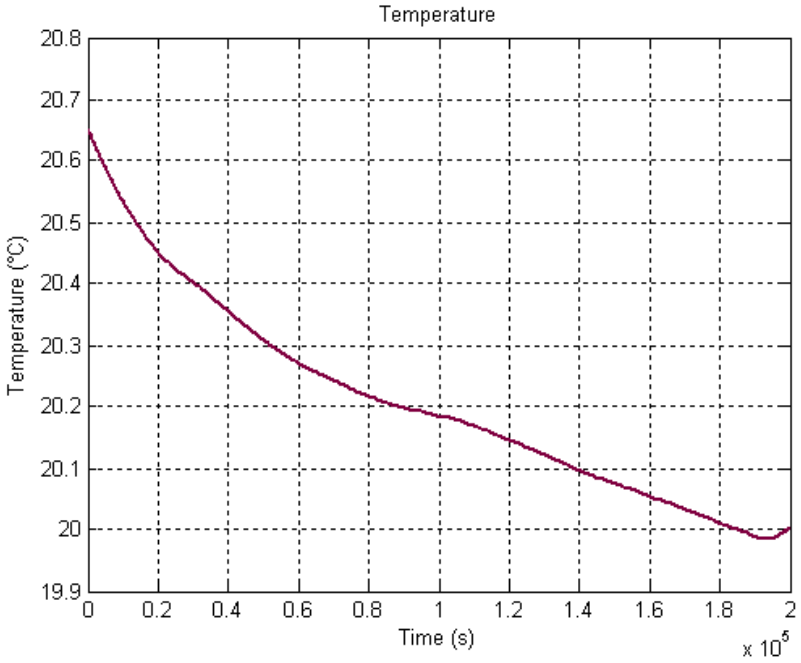

Figure 3.8: Time evolution of temperature inside the plexiglas box (He-Ne setup).

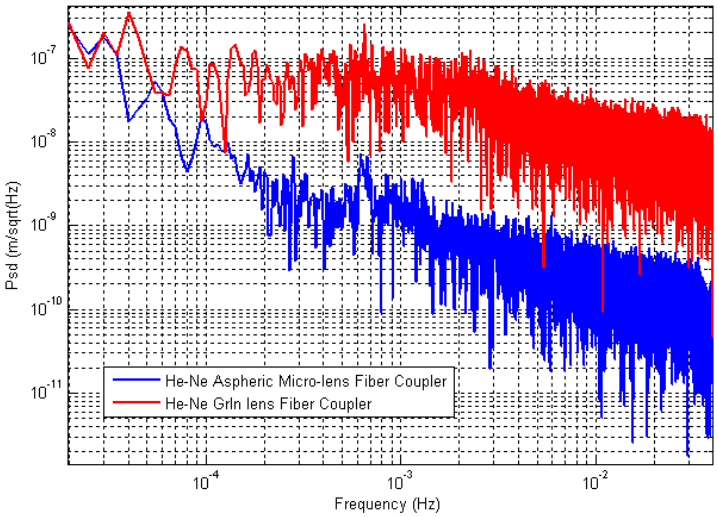

Figure 3.9: Power spectral density of the measured proof mass displacement. The blue curve represents the measurement obtained with the traditional adjustable aspheric micro-lens collimators, while the red curve has been measured using the graded index collimators.

noise of the test mass, we take into account the geometrical relation between the rotation angle $D\phi$ around the axis ortogonal to the optical bench, in the point where the beam is reflected and the horizontal displacement of the light spot on the photodiode:

$$D\phi = \frac{Dx_{Ph}}{2lcos(\vartheta)} \qquad [rad], \tag{3.13}$$

where $l = 57.5\,mm$ and $\vartheta = 45°$ are as usual the armlength and the angle of incidence of the optical lever. Using equation (3.6), we get:

$$D\phi = \frac{Dx_{TM}}{l} \qquad [rad]. \tag{3.14}$$

From the test mass displacement data relative to the blue curve in figure 3.9, we obtain the angle noise curve of figure 3.11. As it is possible to see, the ORO noise level is below the capacitive sensor curve at all the interesting frequencies.

Sensitivity curves analogous to the blue curve in figure 3.9 have been obtained with the rigid setup enclosed in the thermally insulated box.
General results obtained with the He-Ne light source are illustrated in figure 3.12, for a wider range of frequencies.
The demonstrated sensitivity performances of the ORO are good: the noise level is below the capacitive readout's specifications in almost all the frequency band. As it is possible to see from the figure, the two curves intercept around $0.5\,mHz$, but above $1\,mHz$ the ORO curve decreases as $1/f^{1/2}$. This slope is in agreement with the electronic noise model, although the absolute value is greater than the model curve by a factor of about 4. Below $1\,mHz$ the ORO spectrum has a steeper behaviour, with a slope around $1/f$. For frequencies above $10\,Hz$, it approaches the shot noise limit, in agreement with the model.

There is still a residual unidentified noise which keeps the measured spectrum above the ORO model noise by a factor ≈ 4 over large part of the bandwidth. However, the demonstrated performance is already good enough

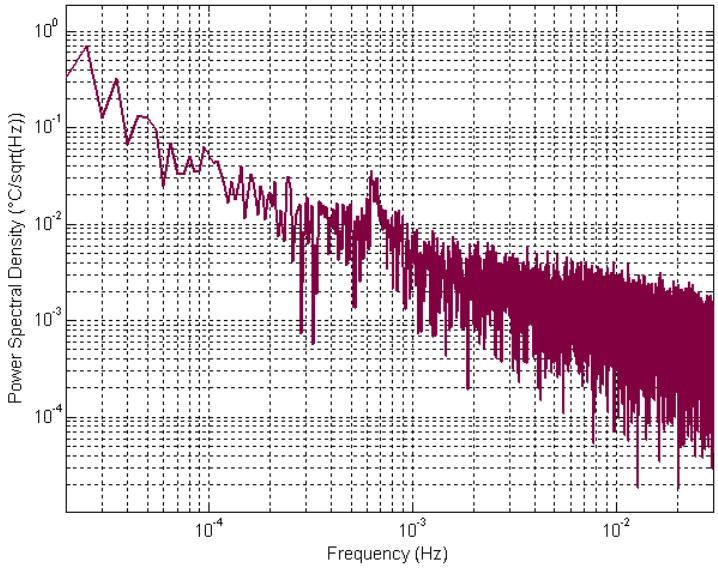

Figure 3.10: Power Spectral Density of the temperature inside the plexiglas box (He-Ne setup).

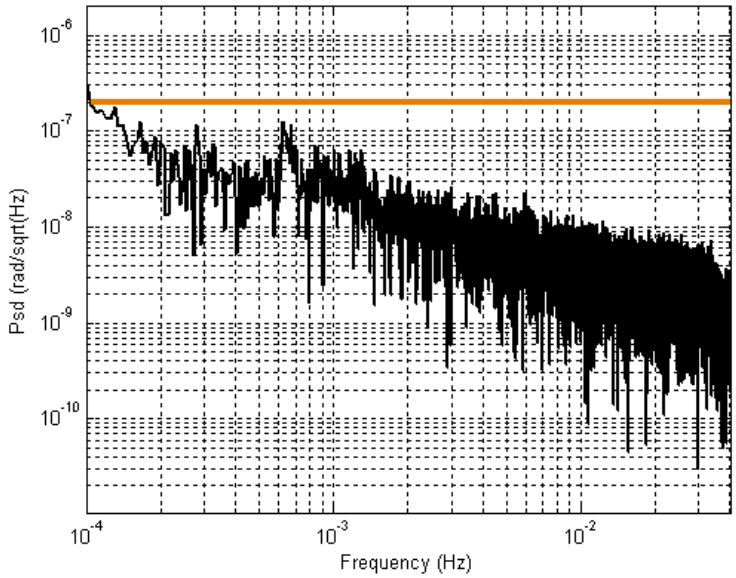

Figure 3.11: Comparison between ORO angular sensitivity performance (He-Ne setup, black spectrum) and the corresponding capacitive sensor requirement (orange line).

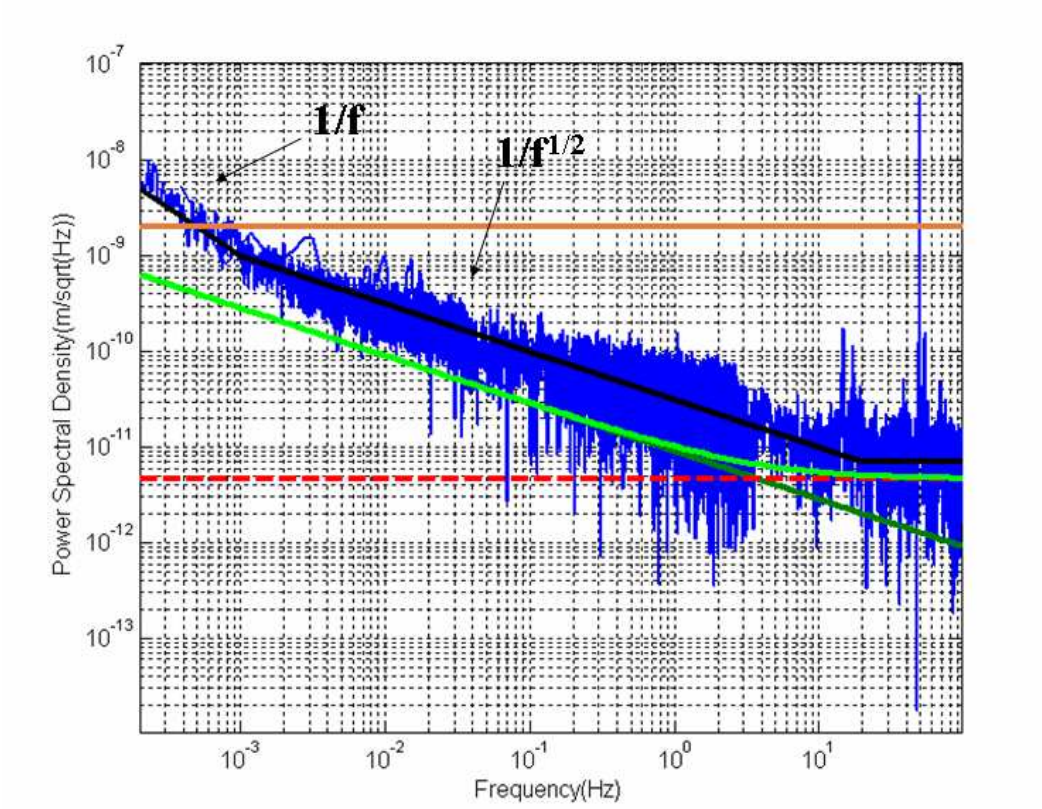

Figure 3.12: Comparison between ORO measured displacement noise (He-Ne setup, blue curve), ORO model noises (shot noise: red dashed curve; electronic noise: dark green; total model noise: light green) and the capacitive sensor requirement (orange line). The black curve is a schematic representation of ORO measured noise level, that will be useful for further calculations.

for our purposes.

Of course the identification of the excess noise is an important task, because if we don't understand its origin we cannot be sure about its relevance in space environment.

Actually another important point is that the results shown here correspond to the best measurement performed in the He-Ne configuration of the ORO. The sensitivity performances achieved with the same configuration in different measurement were not equal. The results were not constant and stable: as already mentioned, it is very difficult to keep under control all the experimen-

tal and environmental conditions in measurement carried out at frequencies ranging from $10^{-4}\,Hz$ to $0.1\,Hz$. On the not stationary results obtained with the He-Ne measurement I will come back later, in the paragraph concerning the SLED sources.
Despite these two points, the results were very encouraging.
However the measurement carried out with the He-Ne laser have to be considered as preliminary, because this kind of light source does not suit space operation: it is fragile, power consuming and has relatively large overall dimensions. Consequently it can only be used for ground tests as the bench-top measurement, but not as a reference solution to be flight on LISA, where some solid state source should be adopted. Possible solutions can be laser diodes or light emitting diodes, described below.

3.3.4 Laser Diode Source

We have tested an infrared laser diode, having a wavelength $\lambda = 830\,nm$. The choice of the wavelength is dictated by the fact that LISA's proof mass has maximum reflectivity for infrared light. A laser diode is a solution suitable to space: it is small (dimensions), robust and requires less power than the He-Ne laser.
The experimental features were the following: Laser diode ($\lambda = 830\,nm$, $P_0 = 0.2\,mW$); PM optical fiber ($\lambda = 830\,nm$); aspheric micro-lens collimators ($\lambda = 830\,nm$, spot size= $0.2\,mm$); fiber coupled Faraday insulator ($\lambda = 830\,nm$, attenuation); windowless QPD (quantum efficiency, responsivity); test mass mounted on micrometric translator ($C_{TM} = 7000\,m^{-1}$); expanded polystyrene box [4].
The measurement showed that the laser diode was affected by mode hopping, as illustrated in figure 3.13. The source works on a certain resonant frequency for some time and then a sudden instability makes it 'jump' to an-

[4]Furthermore in this setup it was necessary to introduce an optical filter (optical density= 0.5) at the end of the fiber output coupler such to reduce the incident otical power, in order not to saturate the photodiode amplifier.

other resonance mode: the operation point of the source switches from one longitudinal mode to another, causing both the laser power and the wavelength to undergoe istantaneous variations. The first effect is corrected by normalization. On the other hand, the instantaneous changes in the emitted wavelength result in sudden displacements of the light spot on the detector, originating on the dioptric surfaces at the fiber end (which is angle polished, as I mentioned before) and through the collimator lens. These are actual beam displacements, that cannot be canceled out by normalization [5].

The mode hopping causes an increase in the noise level of the sensor. It

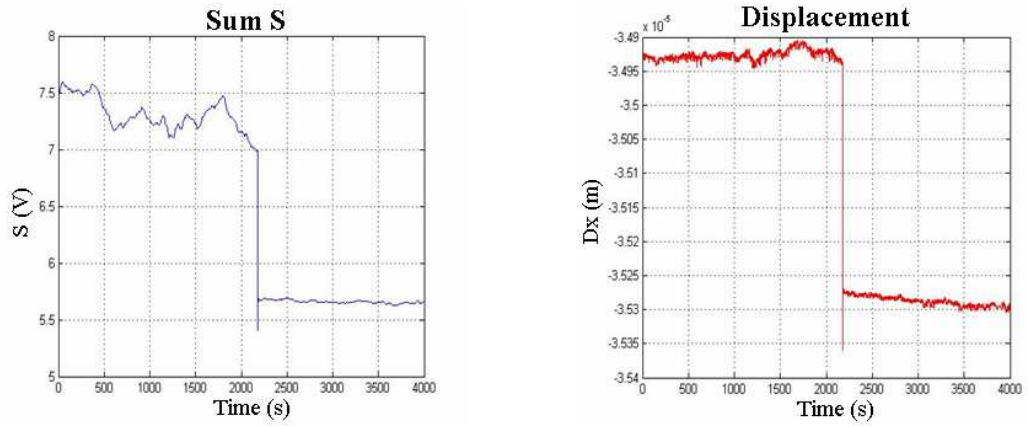

Figure 3.13: Laser diode mode hopping. The graph on the left side shows the jumps in the time evolution of the sum S, while the plot on the right hand represents the corresponding jumps in the horizontal displacements of the light spot on the photodiode.

is worth noting that a laser diode undergoing a mode jump every few hours would be acceptable for the majority of applications, where relatively high frequency (above $100\,mHz$) are involved, but cannot be used at the very low frequencies we are interested in. Our measurement last several days and the

[5] In order to verify that frequency variations of the laser light result in actual displacements of the light spot on the photodiode, we made some tests with the He-Ne laser. We induced a sinusoidal frequency modulation of the laser light by feeding an external sinusoidal signal (Amplitude= $10\,V$ Frequency=$100\,MHz$) at the external driving input of the laser. The measurement showed that the sinusoidal behaviour was reproduced either in S than in H_N and V_N. The frequency modulation causes real displacement of the beam.

mode jumps turn out in an unacceptable noise source.
It is possible to reduce considerably mode hopping in two ways: by inserting a Faraday optical insulator in the optical path, in order to cut out any back-reflection; by actively stabilizing the laser diode temperature and current. However both strategies do not solve completely the problem: disturbance can be hardly eliminated at all.
The mode hopping phenomena is common in Fabry-Perot laser diodes, but alternative solutions can be found. Indeed in the next future we plan to investigate Distributed Feed-Back (DFB) laser diodes and Fiber Bragg Grating (FBG) laser diodes, which should be mode hopping free.

3.3.5 Super Luminescent Light Emitting Diode

We were lucky with our second choice among solid state light sources: we successfully tested fiber coupled super luminescent light emitting diodes (SLED). The wavelength is once more $830\,nm$.
Compared to traditional LEDs, these light sources have a greater optical efficiency. They are in between laser diodes and normal LEDs, in some sense. As laser diodes, they provide an almost monochromatic beam, but with a relatively short coherence length (well below $1\,mm$). On the other hand they are not lasing, so they are mode hopping free.
The very short coherence length make the LEDs unsuited to cases in which coherent light is needed, as in interferometric optical readouts. For an ORO based on optical levers there is no need of coeherent light. On the contrary the use of incoherent light can be an advantage: the short coherence length avoids the effect of ghost fringes, due to multiple reflections within optical components or windows, which can, in some cases, spoil the sensitivity of the ORO system, as we have mentioned before.
Moreover SLEDs (like laser diodes) are already available on the market with single-mode fiber pigtail and in compact standard packages (like Butterfly or Mini-Dil), so that their integration on the LISA flight hardware should be relatively easy.

The experimental setup used for the measurement shown in figure 3.14 is the following: SLED source ($\lambda = 830\,nm$, $P_0 = 0.2\,mW$); PM or equivalently SM optical fiber ($\lambda = 830\,nm$); aspheric micro-lens collimator ($\lambda = 830\,nm$, spot size= $0.4\,mm$); no Faraday insulator; windowless QPD (responsivity); test mass mounted on micrometric translator ($C_{TM} = 4000\,m^{-1}$); expanded polystyrene box. Tests have been performed also with graded index fiber couplers ($\lambda = 830\,nm$, spot size= $0.4\,mm$), giving noise levels in a factor $2 - 4$ above the sensitivity curve measured with aspheric micro-lens.

From graph 3.14 it is possible to see that the ORO sensitivity performances

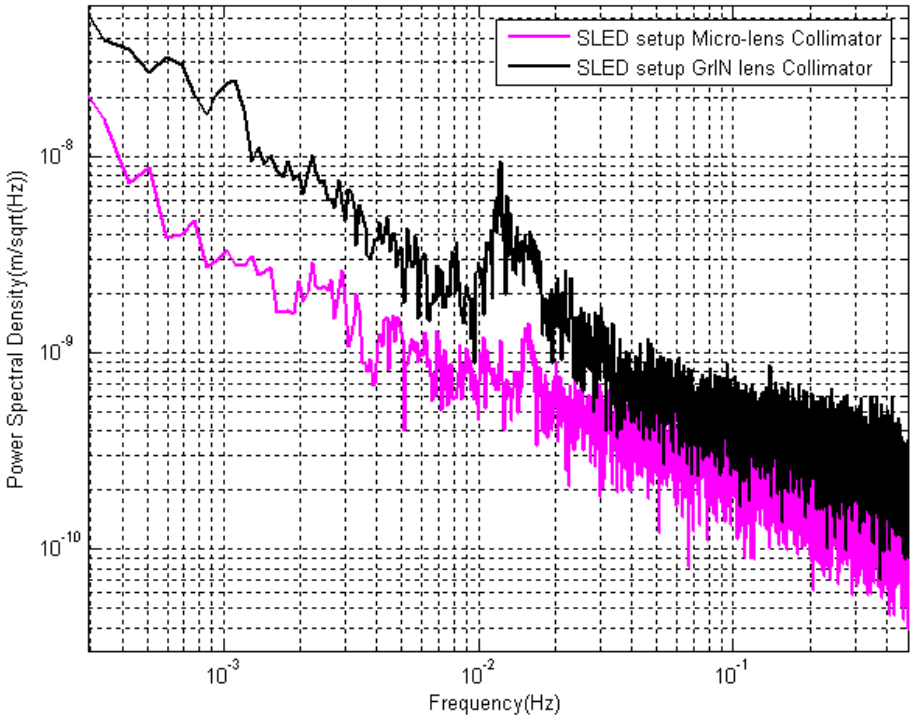

Figure 3.14: ORO sensitivity performances with the SLED setup. The measurement obtained with micro-lens collimators are represented by the pink curve, while the results achieved with the graded index collimators are plotted in black.

with the SLEDs sources are comparable to the best ones achieved with the He-Ne laser. Furthermore, while the best sensitivity curves obtained with He-

Ne sources were not easily reproducible, in the case of the SLEDs the ORO behaviour shows to be much more stable and reliable and measurement have a higher degree of repeatibility. From these experimental observations we can reasonably infer that the not stationariness of the ORO sensitivity performances achieved with the He-Ne was caused by laser instabilities.
All the previous reasonings, added to the fact that the SLED features are suited to space, have made up our mind to choose the SLED as our reference solution, at least until we try the DFB and FBG laser diodes.
It is important to note that we observed that after a certain period of use, ranging from 30 to 60 hours of light emission, the SLED sources undergo deterioration: the optical power begins to decrease linearly with time and correspondingly the normalized variation $\Delta S/S$ of the sum signal shows a medium rate of the order of $10^{-7}\,s^{-1}$. It is necessary to solve this problem in view of space use, finding longer lasting SLEDs.

3.3.6 Electronic Noise measurement

In order to make measurement of the electronic noise of the photodiode amplifier it is necessary to shade the detector or, equivalently, to shut down the incident laser beam. The measurement is carried out in the usual way, with the only exception that now no light reaches the photodiode. The signals coming out from the photodiode amplifier thus represent the intrinsic electronic noise of the device.
To compare the measured electronic noise with the experimental sensitivity curves it is necessary to render homogenous the data. The voltage noise data $H_{ElNoise}$ and $V_{ElNoise}$ have to be normalized with respect to the sum S (or to its mean) [6] relative to the enlightened photodiode data with which we want to make the comparison. Of course, if we want to compare the spectrums in meters, also the corresponding calibration factor has to be used, as usual.

[6] We normalize with respect to the mean value of S instead to S itself because the measurement to compare are usally carried out in different days and the data stream have different number of samples and sampling frequency.

It is possible to see from figure 3.15 that the measured noise behaves like

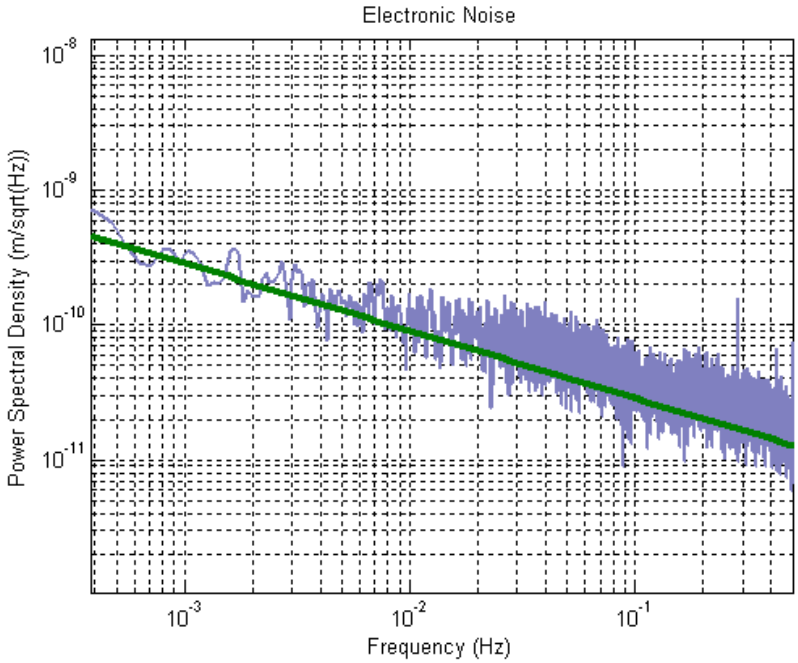

Figure 3.15: Comparison between ORO measured electronic noise (violet curve) and model electronic noise (green line).

$1/f^{1/2}$, as expected. Furthermore, after calibration the measured noise level is reproduced quite well by the model equation (2.9), once the actual values for P_0, and C_{TM} are taken in account.

As already stressed in the paragraphs above, despite the agreement of the measured electronic noise with the model, the measured sensitivity is above the expected noise by a factor of about 4 over almost all the considered frequency band. Improvements in sensitivity have been achieved testing the different devices described above, as windowless photodiodes, special light sources and different fiber components. However this residual unexplained noise remains. We performed different tests in order to identify and cancel the excess noise, as described further in this chapter.

3.3.7 Prototype for the ORO integration on Trento torsion pendulum

The great part of the measurement described in this chapter has been performed with the rigid setup. However, during my thesis work also another ORO bench-top layout has been developed and tested. This is a real scale prototype reproducing the ORO configuration as it will be integrated on the torsion pendulum in Trento. We have developed this real scale prototype in order to make preliminary tests of the ORO layout proposed for the integration.
A detailed description of the study which has lead to the current ORO integration scheme lies outside the aims of this chapter and is instead furnished in chapter V. Here I will just introduce briefly the experimental setup, which has been used for the bench-top tests.
As it is possible to see from figure 3.16, in this setup the light beam travels in a plane which is ortogonal to the optical bench. The test mass is fixed on

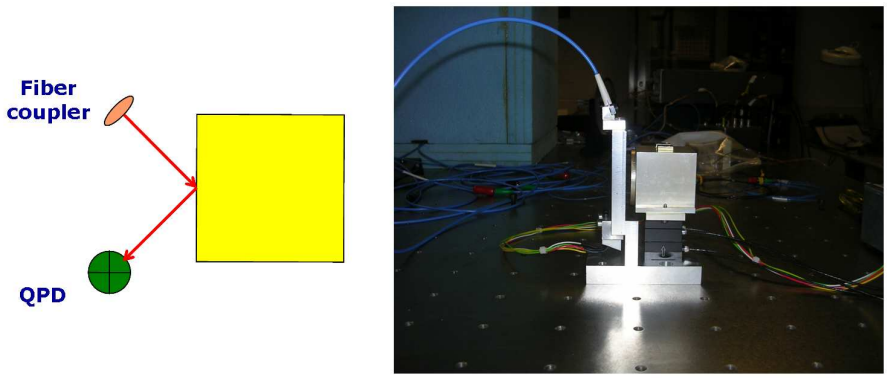

Figure 3.16: ORO real scale bench-top prototype for integration in Trento torsion pendulum.

three piezoelectric translators in a column, which are screwed in their turn to the basis of the setup. The mirror is on the left side of the test mass. The ORO components (fiber collimator and the photodetector) are mounted on

a kind of L-shaped structure on the left, which is fixed on the basis. This latter is screwed to the optical bench.
The optical lever is defined by the armlength $l = 52.5\,mm$ and the angle $\alpha = 70°$.
The reference solution adopted for the light source is a fiber coupled SLED ($\lambda = 830\,nm$). The fiber output coupler is a pigtail aspherical micro-lens collimator with a diameter of $4\,mm$ ($C_{TM} = 11000\,m^{-1}$). Figure 3.16 shows the collimator mounted on top of the L-shaped support: the holder is the one described in section 3.3.2 with the two cilindrical grooves tightened by two lateral screws.
The photodetector is a quadrant photodiode and is glued to a macor support, screwed to the L-shaped structure on the bottom.
During the measurement the setup is enclosed in the plexiglas box.
The performed measurement are shown in figure 3.18 (pink curve): the results are very good, the sensitivity performances are comparable with the best ones obtained with the He-Ne setup. As it is possible to see in graph 3.18, the system has got a (presumably) thermal peak around $1.4\,mHz$.

3.3.8 Comments on general results

As it has been anticipated at the beginning of this section, figure 3.17 shows the improvements achieved in ORO sensitivity with different setups: starting from the so called bench-top measurement (pink curve), in which there was no rigid setup but the elements were separately mounted on the optical bench; passing through the first measurement with the rigid setup and the traditional QPD (red curve); ending with a rigid setup measurement obtained using the windowless QPD (blue curve). In all these setups the light source was an He-Ne laser.
In figure 3.18 are plotted the results of some sensitivity measurement performed with the He-Ne setup (blue line) and the SLED prototype layout (magenta line). In particular, we selected the results obtained with the setup giving the best performances. Both the curves are the average of measure-

ment performed with the same setup at different times and in different frequency intervals.

On the same plot are also reported the expected sensitivity of the capacitive

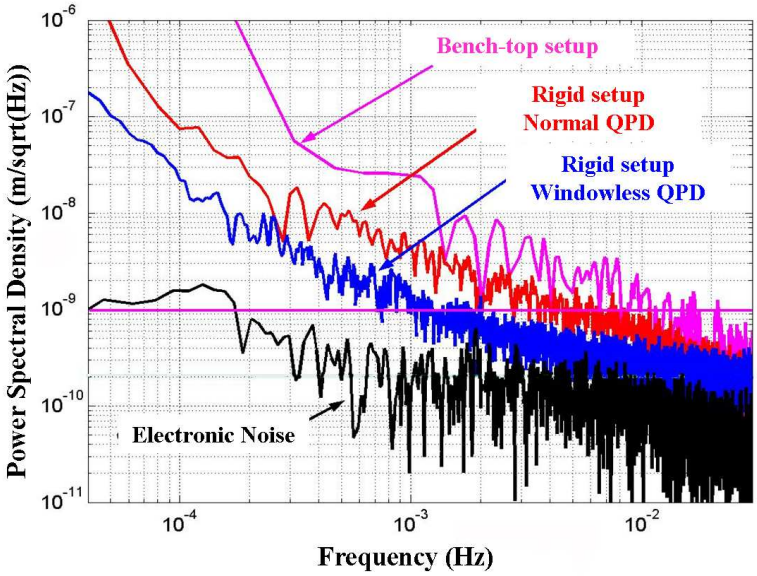

Figure 3.17: Comparison between old and new measurement of ORO sensitivity (He-Ne laser source). The measurement performed with the first bench-top setup are shown by the pink curve. The red and blue curves refer to rigid setup measurement using respectively a traditional QPD and a windowless QPD. The measured electronic noise is shown in black. The magenta line is plotted with the only purpose of indicating the noise level $10^{-9}\, m/Hz^{1/2}$ as a visual reference.

sensor (orange line) and the expected electronic noise (green line) and shot noise (red line) computed according to equations (2.8) and (2.9) respectively and their incoherent sum (cyan line). The noises have been computed for He-Ne assuming $P_0 = 0.2\, mW$ and $dI/dx = 0.5\, A/m$, but they change only slightly for the SLED.

Finally, the black line represents an approximation of the measured sensitivity (essentially the same with both the light sources) that we will use for further analysis.

From the analysis of figure 3.18, we can give some conclusion about the

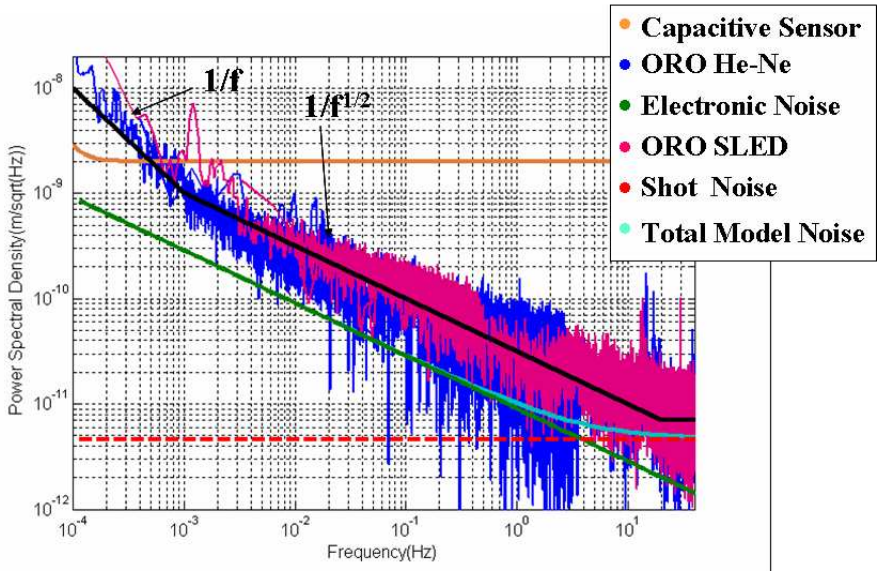

Figure 3.18: General comparison between ORO noise levels measured with different experimental layouts. ORO sensitivity with the He-Ne setup (blue line) and the SLED prototype setup (magenta line). Expected sensitivity of the capacitive sensor (orange line) and expected electronic noise (green line) and shot noise (red line) and their incoherent sum (cyan line). The black line represents an approximation of the measured sensitivity (essentially the same with both the light sources), which will be used in further calculations.

ORO sensitivity. First of all, it is verified experimentally that an ORO system based on optical levers and position sensors can give much higher sensitivity than the one achieved by the capacitive sensor designed for LISA. In our measurement, the improvement ranges from a factor of 2 at $1\,mHz$ to a factor of 20 at $100\,mHz$.

At lower frequencies, below $0.5\,Hz$, the ORO noise spectrum exceeds the design sensitivity of the capacitive readout, showing a steeper slope. We think that this is mainly due to thermal and mechanical drifts, rather than to sensor intrinsic noise.

For frequencies above $10\,Hz$, the residual noise approaches the shot noise limit, in agreement with the model.

One more interesting point, is that, in a large frequency band, the measured noise spectrum shows a $1/f^{1/2}$ slope. This slope is in agreement with the

electronic noise model, but the absolute value is about a factor of 4 above the expected one. On the other side, the measured electronic noise, essentially dominated by the current noise of the trans-impedance amplifier used to read the QPD signal, is in agreement with the model. We observed this discrepancy between actual and potential sensitivity of the ORO in all our measurement. The main investigations we carried out in order to identify the excess noise are described in the next subsections. The tests have been performed before introducing the SLED sources; we used thus the He-Ne laser setup.

3.3.9 Analysis of thermal effects

Temperature variations of the rigid setup can be good candidates as sources of the excess noise.

A handy way of verifying the effects of temperature variations and thermal isolation on the ORO system is to expose the rigid setup to a periodic heating source. We used a normal desk lamp as heating source, its lighting regulated by a timer. We have performed measurement with different lightings periods, with the rigid setup closed in the thermally insulated box and then in the plexiglas box. The experimental configuration was the same described for the He-Ne measurement.

Figure 3.19 shows the time evolution of the temperature and of the corresponding horizontal signals of the photodiode when the apparatus is thermally isolated and when it is not (period of 60 minutes: $30\,min$ lamp on and $30\,min$ lamp off).

Correspondingly the spectrums of the horizontal signals show different amplitudes at the thermal resonance, stating the necessity of thermal isolation (figure 3.20).

However, despite the good filtering of temperature fluctuations operated by the expanded polystyrene box, we didn't observe any improvement in displacement sensitivity out of the modulation frequency.

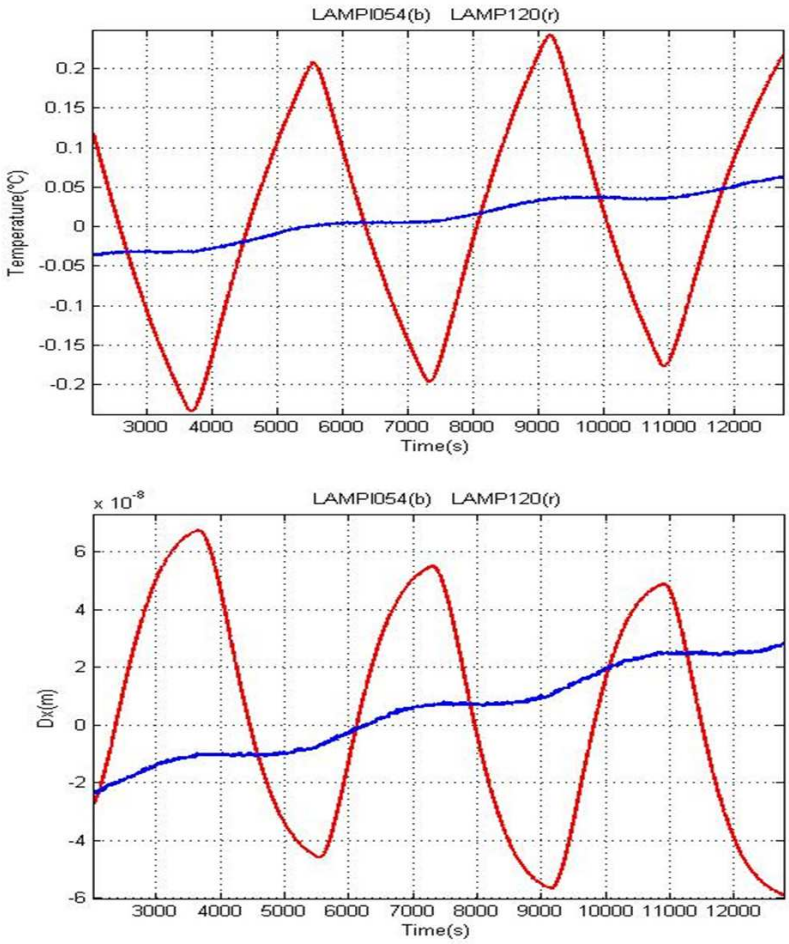

Figure 3.19: Temperature and test mass displacement time evolution using plexiglas box (red curves) and expanded polystyrene box (blue curves).

3.3.10 Measurement in vacuum chamber

Other investigations in order to identify the residual excess noise consisted in the measurement under vacuum. The aim is to cut-out the effect of air flows and air refractive index fluctuations.

The vacuum encloser used to test the rigid setup is shown in figure 3.21. The optical fibers and the electric cables of the photodiode enter the vacuum

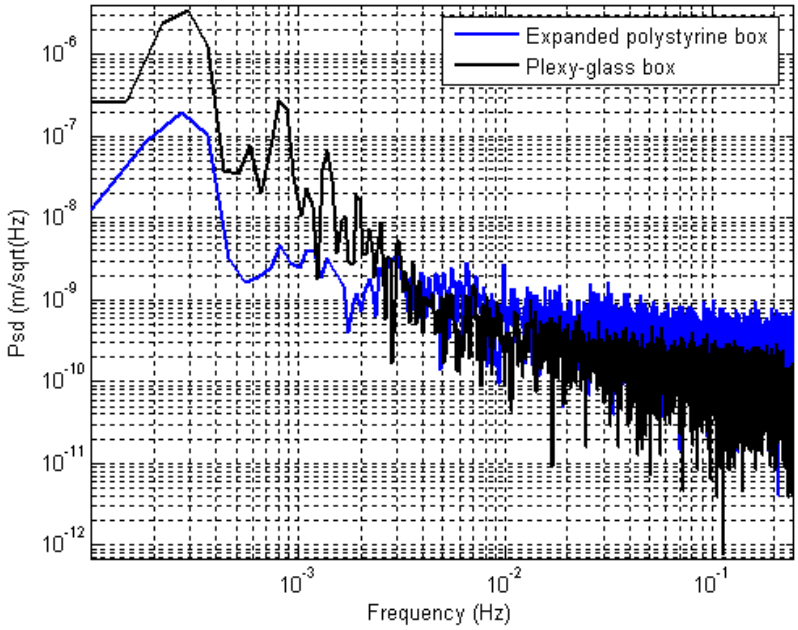

Figure 3.20: Comparison between ORO displacement noise levels using plexiglas (red curve) and polystyrene box (blue curve). The system undergoes a periodic thermal solicitation by means of the lamp light (period: 60 minutes), corresponding to the resonance peak at about $0.3\,mHz$ which is present in both the spectrums. Despite the better thermal isolation, the effects of which are remarkable at low frequncies, above $3\,mHz$ the noise level in the polystyrene box is even slightly higher than in the plexiglas box. This means that at those frequencies thermal noise is not predominant.

chamber through suitable feedthroughs. We fixed the rigid setup to the floor of the chamber. We used the same experimental configuration described in section 3.3.3, but with fiber components suited to vacuum.
The starting operation pressures of our measurement were in the order of $0.1\,mBar$, obtained with a two stage rotary pump.
The vacuum tests of the rigid setup were not successful: the noise level of the horizontal and vertical signals of the photodiode were very high and not stationary, presumably due to the bad behaviour of the He-Ne laser source. From the performed measurement we couldn't get any resolutive answer about the influence of air pressure on the ORO sensitivity. We plan

Figure 3.21: Vacuum encloser used to test the rigid setup.

to repeat the measurement campaign with the SLED sources.

3.3.11 Differential Measurement

The rigid setup is symmetric to allow differential measurement, as it has been said at the beginning of this chapter. As it is possible to understand from the first sketch in figure 3.22, a translation of the test mass along the diagonal of the steel block produces a symmetric displacement of the two light spots along the horizontal axes of the two photodiodes. By summing the two displacement signals it should be possible to cancel out the common noise and obtain a better sensitivity.

We performed many different measurement in order to establish if the signal combination works at noise cancellation. Tests were carried out both with two He-Ne lasers and with two SLEDs, and their respective setups described previously. Unexpectedly all the results showed no noise cancellation neither by summing the signals nor by subtracting them.

We have thus performed special tests on our rigid setup, in the different con-

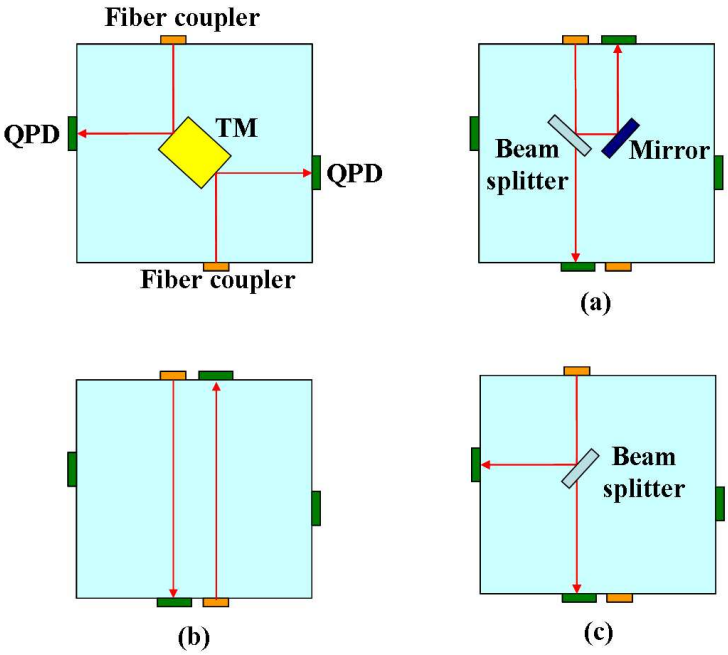

Figure 3.22: Differential measurement configurations on the rigid setup (top view). The first picture shows the rigid setup prepared for differential measurement in its usual symmetric layout. The yellow rectangle represents the test mass. The orange and green rectangles are respectively the fiber couplers and the QPDs. Sketch (a) shows a modified layout in which the incoming light beam is divided in two beams by a beam splitter. One of the beams goes straight through towards the front QPD. The second beam is directed by a mirror to the back QPD. Sketch (b) shows a setup using two light sources. The light beams go straight from the fiber couplers to the relative QPDs, placed in opposite positions. In the last setup a single light beam is splitted by a beam splitter, but differently from layout (a) the two secondary beams are both sent to their relative photodetectors without any other mirror reflection.

figurations illustrated in figure 3.22.

In the first case a laser beam is divided by a beamsplitter in two components, in order to have a symmetric condition with a single light source. The two signals Dx^1_{Ph} and Dx^2_{Ph} are very similar (figure 3.23), although not as much as we expected. Reasonably the difference can be explained by the effect of the mirror. However, the difference $\frac{1}{2}(Dx^1_{Ph} - Dx^2_{Ph})$ shows a small noise cancellation, especially at low frequencies, as it is shown in figure 3.24.

Very slight cancellation with the sum combination $\frac{1}{2}(Dx^1_{Ph} + Dx^2_{Ph})$ is ob-

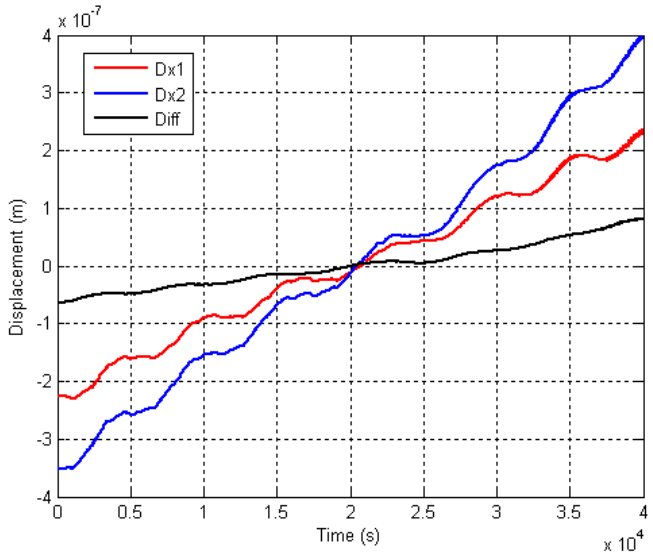

Figure 3.23: Differential measurement with setup (a) of figure 3.22: the horizontal displacements of the light spots on the two photodiodes (blue and red curves) and the difference between the two (black curve).

tained with setup (b) in figure 3.22, where two light sources are used. Laser noise overcomes the common displacement noise.

A definitely better cancellation is obtained with the setup (c), using as in the first case a single light source (figure 3.25). ORO sensitivity looks dominated by actual displacements of the light beam. These displacement can be rotations or translations, of course. However, taking into account the geometrical configuration in use, the results obtained with this last setup suggest that translations of the light beam overcome rotations. The combination $\frac{1}{2}(Dx^1_{Ph} + \alpha \cdot Dx^2_{Ph})$ achieves indeed the best noise cancellation for $\alpha = 1$, which is in agreement with common noise due to translational displacement of the light beam. Geometrical considerations show that common noise due to rotation of the light beam is compatible instead with a value $\alpha \approx 3/10$.

It is worth pointing out that in all the tests performed the sensitivity achieved with noise cancellation does not overcome the one relative to the best mea-

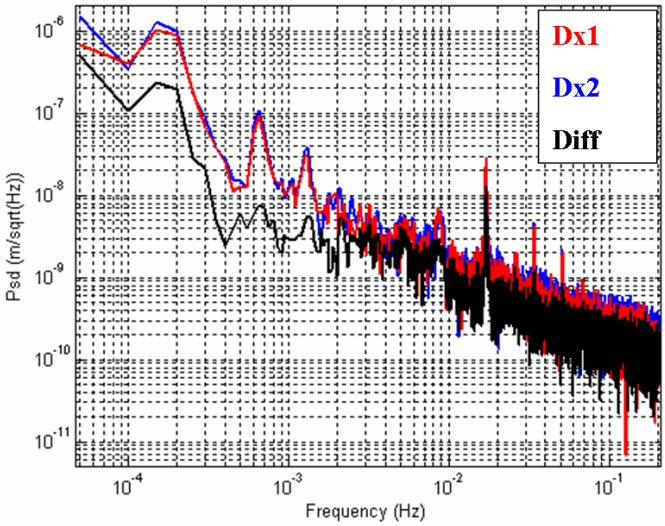

Figure 3.24: Differential measurement: noise cancellation with setup (a). The blue and red curves are the power spectral densities of the horizontal displacements of the light spots on the two photodiodes. The black curve is the power spectral density of the difference signal.

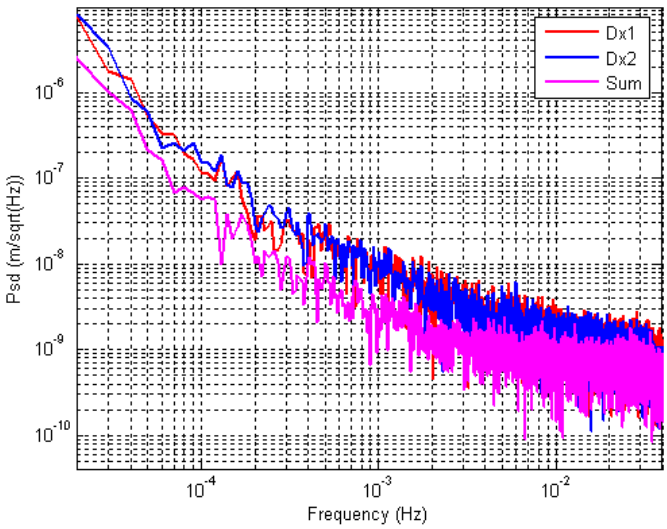

Figure 3.25: Differential measurement: noise cancellation with setup (c). The blue and red curves are the power spectral densities of the horizontal displacements of the light spots on the two photodiodes. The pink curve is the power spectral density of the sum of the two photodiode signals.

surement with the single beam (figure 3.18). This indicates that in the best measurement the limiting noise is not due to beam displacements, which should be reduced by summing or subracting the signals.

3.4 What about the relaxation of cross-coupling conditions?

Considering the sensitivity performances so far demonstrated for the ORO sensor (figure 3.18), we can now estimate the cross-coupling conditions described in chapter II assuming the ORO as LISA GRS solution. Figure 3.26 shows the displacement sensitivity of LISA and the maximum acceptable cross-coupling noise $\tilde{y}_s$ expressed by (2.3). Taking in account the ORO ex-

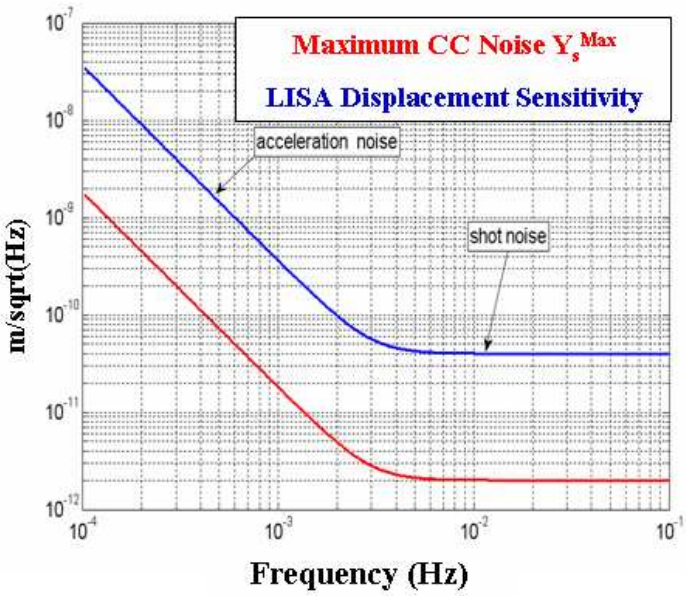

Figure 3.26: LISA displacement sensitivity and maximum acceptable cross-coupling noise.

perimental sensitivity curve, the black line in figure 3.18, we calculate the related maximum acceptable cross-coupling as a function of frequency. In

order to do this we just have to follow equation (2.4):

$$\text{Maximum Cross-coupling} = \frac{\tilde{y}_s}{\text{GRS sensitivity}}, \tag{3.15}$$

calculated at all frequencies.
Using in turn for the *GRS sensitivity* the ORO experimental sensitivity, the ORO model sensitivity and the capacitive sensor sensitivity (figure 3.18), we obtain the results illustrated in figure 3.27.

As mentioned in the previous chapter, the usage of the capacitive read-

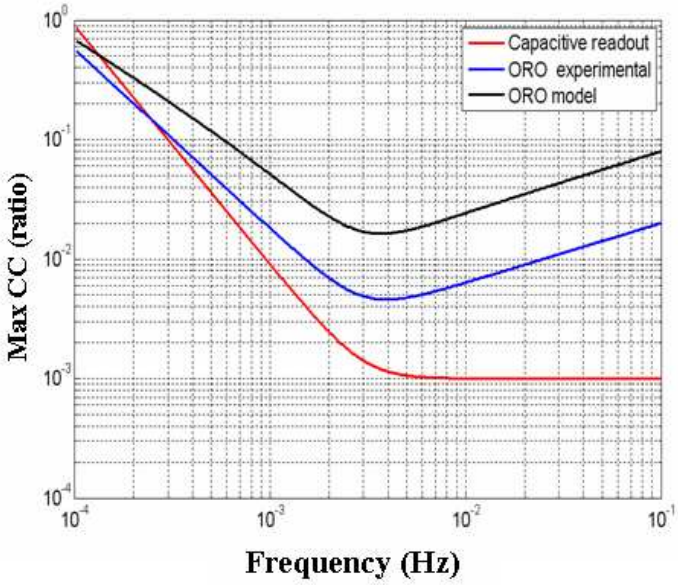

Figure 3.27: Requirements on LISA cross-coupling assuming as reference solution for the GRS in turn: the capacitve sensor (black curve), the ORO sensor with the current sensitivity (blue curve) and the ORO sensor with its potential sensitivity (red curve).

out requires a cross-coupling upper limit of 0.1% above $3\,mHz$, which is an extremely demanding task. Only below $1\,mHz$ it gets above a more reassuring 1%. On the other hand, assuming the ORO measured sensitivity the maximum cross-coupling turns out to be above 1% except for the band $1.5\,mHz - 25\,mHz$ and however above 0.5% almost everywhere, with a minimum of 0.45% at $4\,mHz$.
Of course the relaxation on the cross-coupling conditions gets even greater if

we take into account the ORO potential sensitivity, going well above 1% in the whole frequency band.

In concluding this chapter it is worth stressing that, despite the not yet explained noise source which keeps the measured sensitivity above the potential sensitivity in a factor about 4 above $1\,mHz$, the performances so far demonstrated make of the ORO sensor a very promising candidate either as the main solution for the inertial sensor of LISA, allowing to relax the very stringent cross-coupling conditions imposed by the capacitive sensor specifications, or as a backup solution, constituting an efficient and reliable device to put beside the actual reference sensor.

Chapter 4

The integration of the ORO sensor in LISA

In principle, the actual integration of the ORO in the LISA inertial sensor would be very easy if taken into account from the beginning of the design. On the contrary, the project of the LISA Pathfinder inertial sensor was already in an advanced phase when the ORO was proposed for the first time by my group.
Furthermore, the ground tests of the ORO were still immature and there was not yet an ORO baseline setup suitable to space in order to include the optical sensor in LISA Technology Package. Timing was not favourable to the ORO sensor, but the strong necessity of an auxiliary sensor aboard, being reliable, handy and highly performant, certainly is.
Of course, in case of successful test of the GRS in LISA Pathfinder mission, only marginal modifications will be accepted for LISA. For this reason, in order to develope a trustworthy project for the integration of the ORO, the design of the Pathfinder inertial sensor has been assumed as a baseline, providing the most realistic model actually available for LISA electrode housing.
This chapter deals with the analysis, the experimental work and the measurement I accomplished in order to develope and test a real scale prototype reproducing the electrode housing environment and mounting a suitable ORO

setup.

4.1 The real scale prototype

4.1.1 The integration baseline

The proposal of the current integration scheme of the ORO in LISA GRS was made before I joined the group and is described in [43] [30], to which I refer for further details. Figure 4.1 shows the scheme of the inertial sensor engineering model for LISA Pathfinder at the moment of the proposal. Some details have changed since then, but the principle scheme has remained essentialy the same. In particular the overall dimensions of the caging mechanism

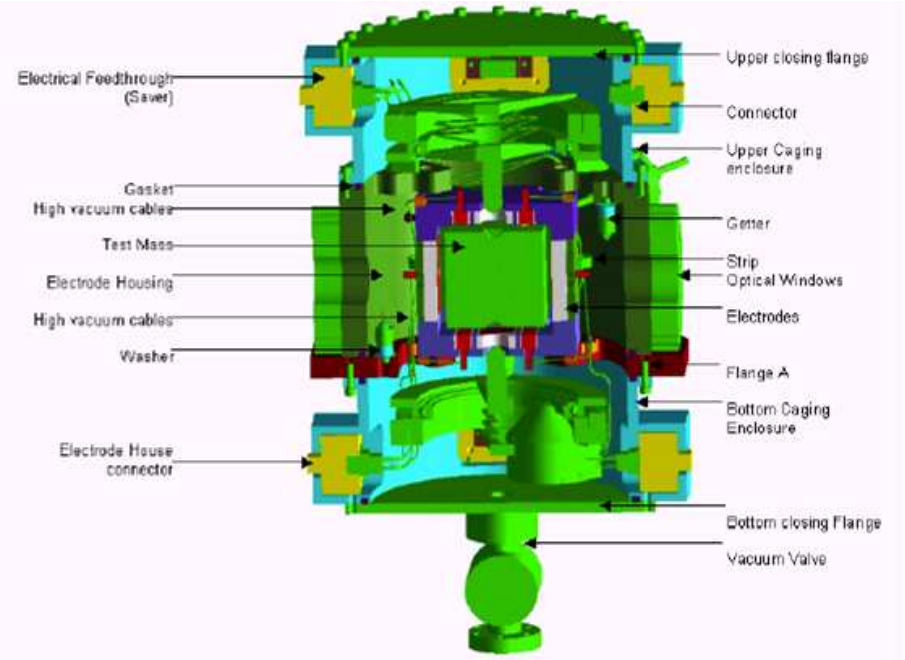

Figure 4.1: Engineering model of LISA Pathfinder Inertial Sensor.

and of the electrodes are basically unvaried and constitute the greater obstacles in finding suitable paths for the ORO light beams. The layout of the electrodes (actuation and capacitive sensing electrodes) and of the locking plunger leaves only a little space for the optical beams to enter the electrode

housing, hit the test mass surface and get out again towards the position sensors.

As mentioned before, if we want to measure the proof mass displacements in all the six degrees of freedom (DOF), we need three ORO sensors, which means three different optical paths. The three light beams impinge on three ortogonal faces of the proof mass, that we call x, y and z, referring to the related normals (see figure 4.4). Correspondingly we shall indicate the associated optical paths with X, Y and Z. Figure 4.2 shows the electrode housing, the grey and orange cube box, enclosing the test mass. On the external green support it is possible to see the three fiber couplers and the three detectors of the ORO setup. The light beams (red lines) are visible at the output of the fiber couplers and when they end on the photodiodes. The hole on top of

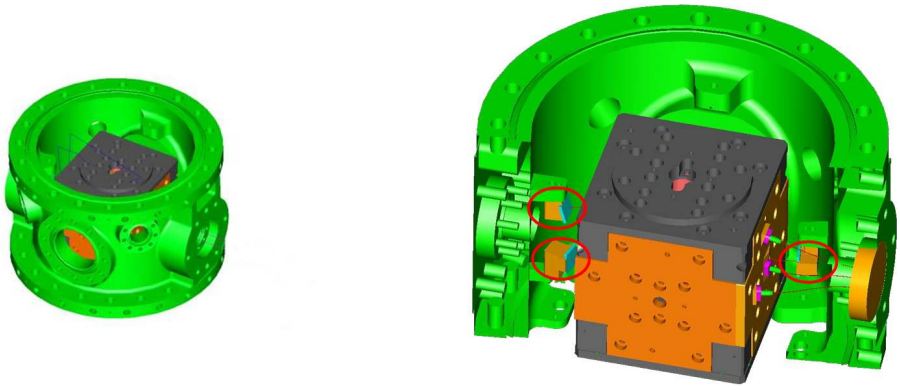

Figure 4.2: LISA Pathfinder vacuum encloser and electrode housing model.

the electrode housing is where the locking plunger of the caging mechanism passes.

Figure 4.3 shows the same picture without the cubic structure hosting the electrodes, in order to reveal the inside. As illustrated in the figure, the proposed solution is to use the electrodes as mirrors along the two x and z paths: each of the two light beams is sent by properly oriented fiber couplers to the surface of a first electrode, gets reflected, hits the test mass, gets reflected by a second electrode and finally reaches the photodiode placed outside the electrode housing. The z path is not centered along the top face of the

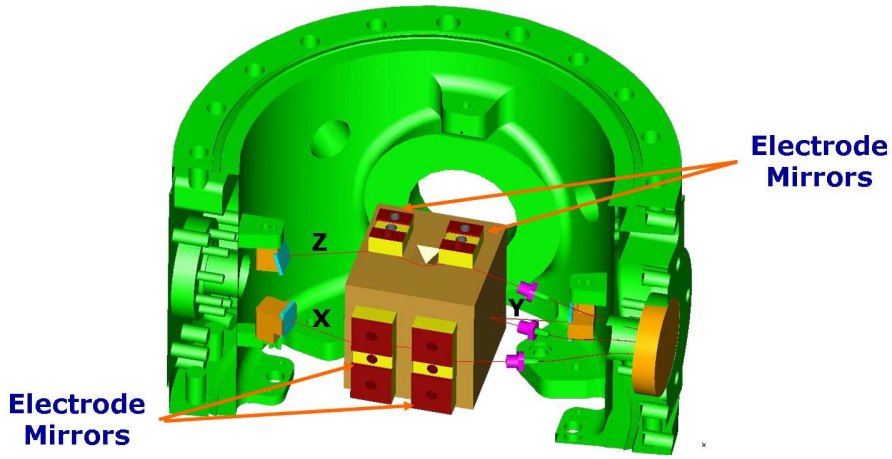

Figure 4.3: ORO integration scheme.

proof mass, because the central part is occupied by the caging mechanism (tetraedric hole in the proof mass top face).
The y-beam hits directly the test mass and is reflected towards the relative sensor, in the usual optical lever configuration. As it is possible to notice already by looking at figure 4.3, the optical lever angle relative to the y path is the smallest. This corresponds to a smaller sensitivity, as explained in the previous chapter.
Another important feature is the use of fibers with suitably small pigtail style collimators, in order to fit the tiny available spaces.

4.1.2 The prototype

The described integration scheme was the starting point of my work on the present topic. I adopted the discussed layout as a reference solution for developing a real scale bench-top prototype, in order to test the proposed ORO setup. It is worth noting that the setup can be updated according to the possible evolution of the inertial sensor design from Pathfinder to LISA.
A $3-D$ picture of the real scale prototype is illustrated in figure 4.4, where

the top lid hosting the two dummy z electrodes has been removed to allow to look the inside.

The test mass hosts three mirrors, one on top and the other two respectively

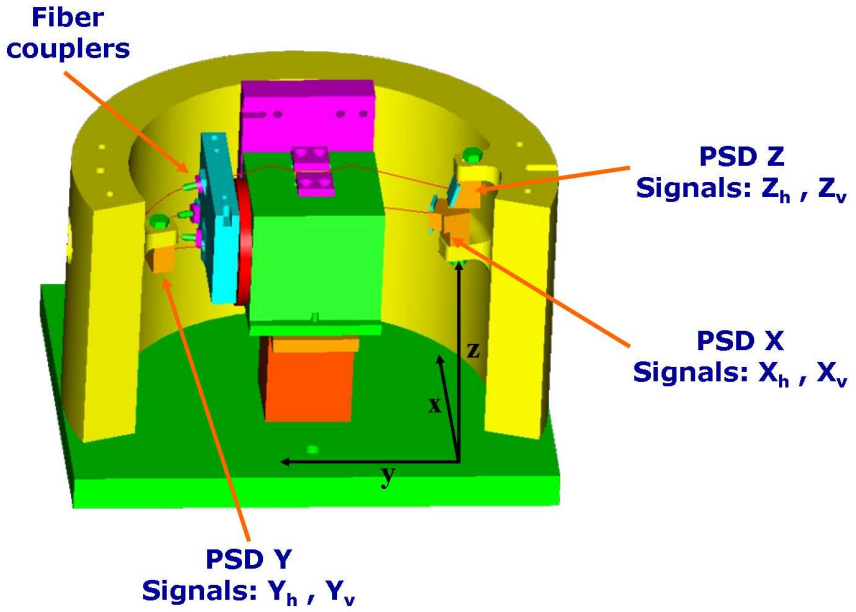

Figure 4.4: Real scale prototype, 3-D picture.

on the left and back side. Other mirrors are fixed to the supports representing the electrode holders, along the x and z paths: two for the x electrodes and two for the z electrodes.

A maybe more clarifying figure is 4.5, which shows a detailed scale scheme of the prototype through its front and top views. The indicated geometrical parameters have the following values:

- $L_x = 30\,mm$, $L_y = 27\,mm$, $L_z = 36\,mm$;
- $\beta_x = 75°$, $\beta_y = 10°$, $\beta_z = 74°$;
- $S_x = 15\,mm$, $S_z = 15\,mm$;
- $d = 6\,mm$.

It is worth remembering that the side length of the test mass is $46\,mm$.

The overall dimensions of the electrodes, of the proof mass and of the

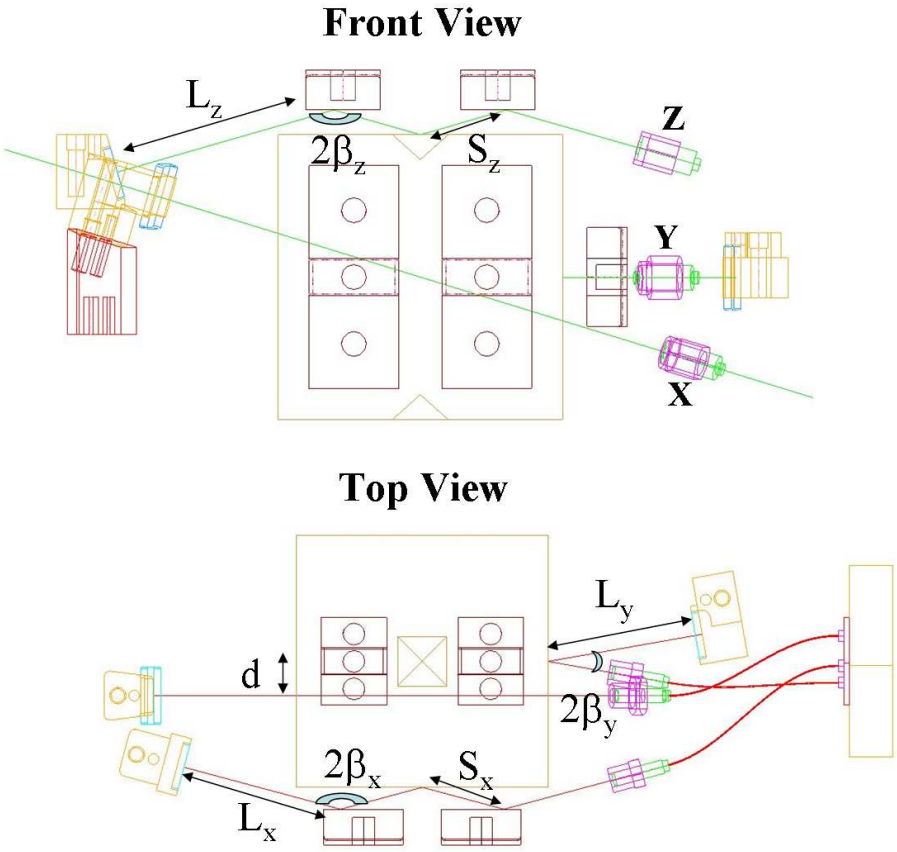

Figure 4.5: ORO integration scheme: top and front projections.

electrode housing are reproduced faithfully as in the actual model, to allow the experimental verification of the correct passing of the light beams and the validation of the design.

Besides this purpose, the tests of the real scale prototype aim at the analysis of the optical matrix of the system. This is the matrix which allows to calculate the test mass displacements from the photodiode signals. It can be calculated analytically by means of the geometrical configuration of the system. Furthermore its elements can be obtained experimentally by proper

measurement. It is thus possible to compare the experimental results with the analytical predictions, as I will show later on in this chapter.
Summarizing, the tests on the real scale prototype concerned mainly two aspects:

- the validation of the integration design;
- the study of the optical matrix.

It is worth noting that in this phase we are not interested in making measurement of the sensitivity performances at this stage of the work.

4.1.3 The experimental setup and the assembling phase

The prototype has been manufactured in the machine shop of INFN section of Napoli. The proof mass and the basic structure are made of aluminium and have been alodyn coated, in order to protect the surfaces. The electrodes are replaced by mirrors with protective gold coating, as the ones attached to the test mass.
Figure 4.6 shows the prototype during the assembling phase. The three mirrors are visible on the top and on the sides of the proof mass. On the left side of the external structure it is possible to see a circular hole, which is the passage for the optical fibers.
As photodetectors we mounted three position sensing devices (PSD). Since the tests do not concern sensitivity measurement, we prefer to use the PSD device, which is more handy, having a sensitivity range which is independent from spot size and thus providing a greater sensitive area. This is important especially in our specific case, in which the extremely small spaces for the passage of the light beams, added to the mechanical tolerances, make it very difficult to center the light spots on the detectors. At this stage of the work it is not worth complicating our experimental problems.
The PSDs are glued to their holders, which have a rectangular profile such as to constrain the photodiodes in the correctly oriented position. [1]. The

[1] Differently from the QPDs, these PSDs have a rectangular shape.

holders in their turn are screwed to the support in the proper locations.
We used the light sources currently at our disposal in the laboratory: two He-Ne lasers to generate the X and Y light beams and a laser diode ($\lambda = 830\,nm$) for the Z path.

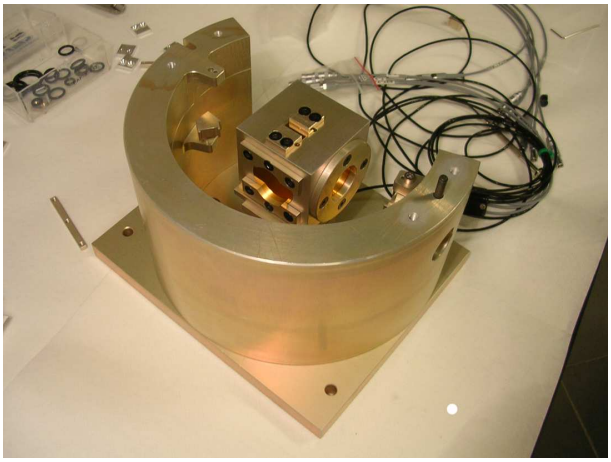

Figure 4.6: Real scale prototype during the assembling phase.

Figure 4.7 shows another important feature of the setup: the pigtail fiber collimaters glued in their alluminium holders, which are stuck in their turn to the support. As it is possible to notice, the profile of the support in the gluing areas is such that the holders are differently inclined, in order to direct the light beams towards the mirrors with the proper angles. The focusers are the $4\,mm$ diameter graded index lens collimaters, which we have mentioned in the previous chapter.
Unfortunately many of these extremely delicate fiber components broke during the assembling phase and we were left with an inappropriate fiber ($\lambda = 830\,nm$) to couple the He-Ne light beam relative to the Y path. For paths X and Z the fibers corresponded to the proper wavelengths, respectively $\lambda = 630\,nm$ and $\lambda = 830\,nm$. The fibers are, as usual, SPM.
The choice concerning the fiber focusers are here dictated by the small dimensions of the setup and by simplicity requirements. In a future study a

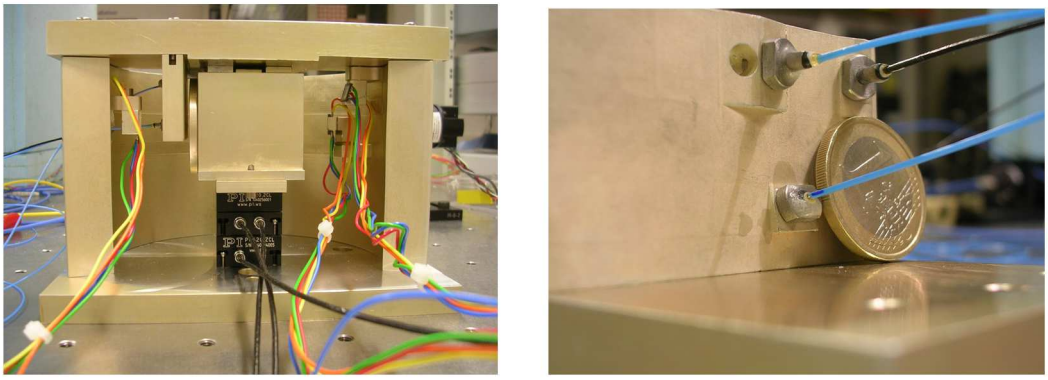

Figure 4.7: The real scale prototype and a detail of the fiber output couplers.

more performant setup suited to work in space invironment must be proposed and tested, in order to establish the proper devices to use for LISA.
As it is shown in figure 4.7, the proof mass is screwed to three piezoelectric translators (PZT) in a column, which allow to move it along the three ortogonal axes x, y and z.

The assembling phase was successful: the reflected light beams reached the photodiodes without clipping, after making few adjustments with thin steel spacers ($\approx 100\,\mu m$). These necessary corrections are consistent with machining tolerances, with the accuracy in the positioning of the fiber output couplers and further with the accuracy in relative alignment of the fiber with its own ferrula.
The maximum distance of the light spots from the center of the PSDs was about $300\,\mu m$.
As expected, it is clear that the accurate positioning of the fiber output coupler will be essential in the real system, and that some possibility of regulating the position of the output detector (for example using calibrated spacers) will be necessary.

4.2 Theoretical versus experimental analysis

4.2.1 The optical matrix and the system calibration

Let's call **B** the optical matrix of the system, which allows to calculate the position of the test mass once we know the signals from the photodiodes. Since there are six DOFs, it is a 6×6 matrix, which is defined by the relation:

$$\begin{pmatrix} X \\ Y \\ Z \\ \alpha \\ \eta \\ \theta \end{pmatrix} = \begin{pmatrix} B_{11} & B_{12} & B_{13} & B_{14} & B_{15} & B_{16} \\ \dots & \dots & \dots & \dots & \dots & \dots \\ \dots & \dots & \dots & \dots & \dots & \dots \\ \dots & \dots & \dots & \dots & \dots & \dots \\ \dots & \dots & \dots & \dots & \dots & \dots \\ B_{61} & \dots & \dots & \dots & \dots & B_{66} \end{pmatrix} \times \begin{pmatrix} X_h \\ X_v \\ Y_h \\ Y_v \\ Z_h \\ Z_v \end{pmatrix}, \qquad (4.1)$$

where the DOFs of the proof mass (X, Y, Z, α, η, θ) ($[m]$, $[rad]$) are indicated in figure 4.8 and the vector (X_h, X_v, Y_h, Y_v, Z_h, Z_v) ($[m]$) includes the photodiode signals (the pedices h and v stand for 'horizontal' and 'vertical'), as shown in figure 4.4. The matrix **B** is a matrix containing all the calibration factors of the system.

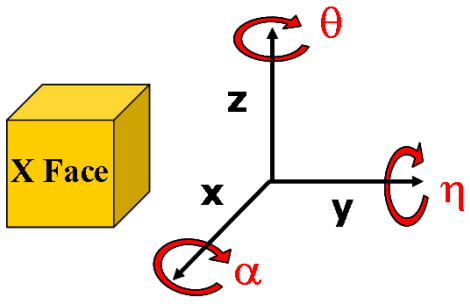

Figure 4.8: Reference frame of the prototype setup.

Actually we can measure the elements of the inverse matrix of **B**, that

we call **A**:

$$\begin{pmatrix} X_h \\ X_v \\ Y_h \\ Y_v \\ Z_h \\ Z_v \end{pmatrix} = \begin{pmatrix} A_{11} & A_{12} & A_{13} & A_{14} & A_{15} & A_{16} \\ ... & ... & ... & ... & ... & ... \\ ... & ... & ... & ... & ... & ... \\ ... & ... & ... & ... & ... & ... \\ ... & ... & ... & ... & ... & ... \\ A_{61} & ... & ... & ... & ... & A_{66} \end{pmatrix} \times \begin{pmatrix} X \\ Y \\ Z \\ \alpha \\ \eta \\ \theta \end{pmatrix} . \tag{4.2}$$

It is worth noticing that the elements of the first three columns are dimensionless, while the elements of the last three have dimensions $[m/rad]$.
The matrix elements A_{ij} are measured using the same basic principle described in the previous chapter for calibration, but here we are interested in more DOFs. So we have to move the test mass of a known amount on one single DOF, using the three DOFs PZT system. In this way, the six matrix elements of a given column can be measured as direct ratio of the six photodiode signals over the input test mass displacement measured by the capacitive sensor of the PZTs. For example, if we move the proof mass along the x axis by a given amount X_0, with no displacements in the other DOFs ($Y = Z = \alpha = \eta = \theta = 0$), we get the matrix elements of the first column as:

$$A_{11} = \frac{X_h}{X_0} \quad A_{21} = \frac{X_v}{X_0} \quad A_{31} = \frac{Y_h}{X_0} \quad A_{41} = \frac{Y_v}{X_0} \quad A_{51} = \frac{Z_h}{X_0} \quad A_{61} = \frac{Z_v}{X_0} \quad . \tag{4.3}$$

In the same way, it is possible to measure the elements of the other columns of the matrix by moving the test mass in the other DOFs. In practice, as we have already mentioned in the previous chapter, the most accurate way of measuring the calibration factors is to excite the system sinusoidally so that the matrix element can be measured with higher precision as the ratio of the power spectral densities of the output and input signals at the modulation frequency f_{sin}. For example, moving the test mass with a sinusoidal excitation X_0 along the x axis, the first element of the matrix would be calculated

as:

$$A_{11} = \left(\frac{\tilde{X}_h}{\tilde{X}_0} \right)_{f_{sin}} \tag{4.4}$$

or

$$A_{11} = \left| \frac{FFT(X_h)}{FFT(X_0)} \right|_{f_{sin}} . \tag{4.5}$$

The second method returns modulus and phase, this latter providing the sign of the matrix element. Once the matrix is filled, we can invert it, in order to obtain the matrix **B**. Actually we can measure only the elements of the first three columns of **A**, because we are not yet supplied with PZT rotators in order to induce calibrated angular displacements of the test mass.
The elements of the second and third columns are measured by moving the proof mass respectively along the y and z axes. If we call the corresponding PZT capacitive signals Y_0 and Z_0, the matrix we can actually measure is:

$$\mathbf{A}_{meas} = \begin{pmatrix} \left(\frac{\tilde{X}_h}{\tilde{X}_0}\right)_{f_{sin}} & \left(\frac{\tilde{X}_h}{\tilde{Y}_0}\right)_{f_{sin}} & \left(\frac{\tilde{X}_h}{\tilde{Z}_0}\right)_{f_{sin}} \\ \left(\frac{\tilde{X}_v}{\tilde{X}_0}\right)_{f_{sin}} & \left(\frac{\tilde{X}_v}{\tilde{Y}_0}\right)_{f_{sin}} & \left(\frac{\tilde{X}_v}{\tilde{Z}_0}\right)_{f_{sin}} \\ \left(\frac{\tilde{Y}_h}{\tilde{X}_0}\right)_{f_{sin}} & \left(\frac{\tilde{Y}_h}{\tilde{Y}_0}\right)_{f_{sin}} & \left(\frac{\tilde{Y}_h}{\tilde{Z}_0}\right)_{f_{sin}} \\ \left(\frac{\tilde{Y}_v}{\tilde{X}_0}\right)_{f_{sin}} & \left(\frac{\tilde{Y}_v}{\tilde{Y}_0}\right)_{f_{sin}} & \left(\frac{\tilde{Y}_v}{\tilde{Z}_0}\right)_{f_{sin}} \\ \left(\frac{\tilde{Z}_h}{\tilde{X}_0}\right)_{f_{sin}} & \left(\frac{\tilde{Z}_h}{\tilde{Y}_0}\right)_{f_{sin}} & \left(\frac{\tilde{Z}_h}{\tilde{Z}_0}\right)_{f_{sin}} \\ \left(\frac{\tilde{Z}_v}{\tilde{X}_0}\right)_{f_{sin}} & \left(\frac{\tilde{Z}_v}{\tilde{Y}_0}\right)_{f_{sin}} & \left(\frac{\tilde{Z}_v}{\tilde{Z}_0}\right)_{f_{sin}} \end{pmatrix}, \tag{4.6}$$

where the sign of each element is identified by the phases of the FFTs at the modulation frequency.

4.2.2 The analytical matrix

The optical matrix is identified by the geometry of the system. It is fixed once the geometrical properties of the setup have been defined. The matrix **A** can thus be calculated analytically by means of geometrical reasonings.
I refer to the geometrical parameters of figure 4.5. I calculated the matrix elements stopping at the first order approximation, achieving the following

result:

$$\mathbf{A}_{geom}=\begin{pmatrix} -\frac{sin(\pi-2\beta_x)}{cos(\beta_x)} & 0 & 0 & 0 & 0 & 2(L_x+S_x) \\ 0 & 0 & 0 & 0 & -2(L_x+S_x)cos(\beta_x) & 0 \\ 0 & \frac{sin(2\beta_y)}{cos(\beta_y} & 0 & 0 & 0 & -2L_y \\ 0 & 0 & 0 & -L_y cos(\beta_y) & 0 & 0 \\ 0 & 0 & 0 & 0 & -2(L_z+S_z)cos(\beta_z) & 0 \\ 0 & 0 & -\frac{sin(\pi-2\beta_z)}{cos(\beta_z)} & -2(L_z+S_z) & -\frac{sin(\pi-2\beta_z)}{cos(\beta_z)}d & 0 \end{pmatrix}. \tag{4.7}$$

The matrix turns out to have determinant equal to zero, because the 2nd and 5th rows are proportional. It is thus not invertible. From a physical point of view this means that it is not possible to extract the proof mass displacements, in all the 6 DOFs, from the signals of the photodiodes in the actual configuration. The current geometry of the system leads to 5 linearly independent equations instead of six, so with this ORO setup it is possible to extract unambigously the six DOFs of the test mass.

If we want to determine the complete position of the test mass we need to find a new geometrical disposition of the three ORO sensors, described by an invertible matrix **A**. I will propose a possible solution in the next section. However, at the moment this design mistake in the originary integration scheme of the ORO in LISA is not a big problem. Indeed in LISA three DOFs of the test mass are read by the main interferometer, so among the 6 position signals needed by the drag free control loop, three are provided by the main interferometer and only the other three have to be furnished by the GRS. I will speak about this argument further on in this chapter.

As a matter of fact, despite the geometrical matrix can't be inverted, the analysis of the present configuration can be very useful, allowing to compare the analytical model with the experimental values.

We can obtain the actual values of the matrix elements by substituting the

parameter values:

$$\mathbf{A}_{geom} = \begin{pmatrix} -1.932 & 0 & 0 & 0 & 0 & 0.0900 \\ 0 & 0 & 0 & 0 & -0.023 & 0 \\ 0 & 0.35 & 0 & 0 & 0 & -0.0540 \\ 0 & 0 & 0 & -0.0266 & 0 & 0 \\ 0 & 0 & 0 & 0 & -0.028 & 0 \\ 0 & 0 & -1.923 & -0.1020 & -0.0120 & 0 \end{pmatrix}. \quad (4.8)$$

We can also calculate the related errors, taking into account the mechanical tolerances of the prototype and using the maximum error propagation. Therefore, we can define an error matrix $\Delta\mathbf{A}_{geom}$ as:

$$\Delta\mathbf{A}_{geom} = \begin{pmatrix} 0.007 & 0 & 0 & 0 & 0 & 0.0004 \\ 0 & 0 & 0 & 0 & 0.002 & 0 \\ 0 & 0.04 & 0 & 0 & 0 & 0.0002 \\ 0 & 0 & 0 & 0.0002 & 0 & 0 \\ 0 & 0 & 0 & 0 & 0.002 & 0 \\ 0 & 0 & 0.008 & 0.0004 & 0.0004 & 0 \end{pmatrix}. \quad (4.9)$$

The previous results have to be compared with the measured matrix.

4.2.3 The measured matrix

The measurement gave the following values for the matrix elements:

$$\mathbf{A}_{meas} = \begin{pmatrix} -1.94 & -0.0126 & 0.173 & - & - & - \\ 0.0119 & -0.0019 & 0.0302 & - & - & - \\ -0.0364 & 0.345 & -0.0439 & - & - & - \\ 0.0101 & -0.0072 & -0.0596 & - & - & - \\ 0.061 & 0.029 & -0.11 & - & - & - \\ 0.034 & -0.019 & -1.8 & - & - & - \end{pmatrix}. \quad (4.10)$$

where the missing elements are the ones we cannot measure with the current setup. An important thing to stress is that different measurement of the

elements of the 5th and 6th row gave very different results. The variation was of the order of about 15%. These discrepancies are explained by the experimental features. Indeed rows 5 and 6 are calculated from the signals of the photodiode Z, associated with the laser diode source. As I have already mentioned in the previous chapter, the laser diode undergoes mode hopping, which causes the calibration factor to change. The matrix elements in rows 5 and 6 are thus estimated as a mean value between the different measurement and the relative errors are evaluated as standard deviations from the mean. The error evaluation concerning the other matrix elements has been made in a different way. Since the matrix elements are calculated as ratios of FFTs, in order to calculate the errors it is necessary to estimate the error on the FFT. This is done by comparing the peak amplitude to the nearby floor noise, as shown in figure 4.9. The maximum error propagation is then used to evaluate the errors on the matrix elements.
Our rough estimate of the matrix elements errors gives:

$$\begin{pmatrix} 0.01 & 0.001 & 0.005 & - & - & - \\ 0.0003 & < 0.0001 & 0.0008 & - & - & - \\ 0.0004 & 0.002 & 0.0003 & - & - & - \\ 0.0002 & 0.0001 & 0.0004 & - & - & - \\ 0.009 & 0.004 & 0.02 & - & - & - \\ 0.005 & 0.003 & 0.3 & - & - & - \end{pmatrix}. \tag{4.11}$$

As it is posssible to see from equations (4.8), (4.9), (4.10) and (4.11), the first three columns of experimental matrix and of the analytical matrix are in good agreement. Our model has been validated by the measurement for what concerns the translational DOFs of the test mass.

4.2.4 Correction for rotated photodiodes

In order to explain the slight discrepancies between analytcal and measured matrix we made an assumption. We supposed that each photodiode had been glued to its holder rotated by an angle $\xi \neq 0$ with respect to the nominal

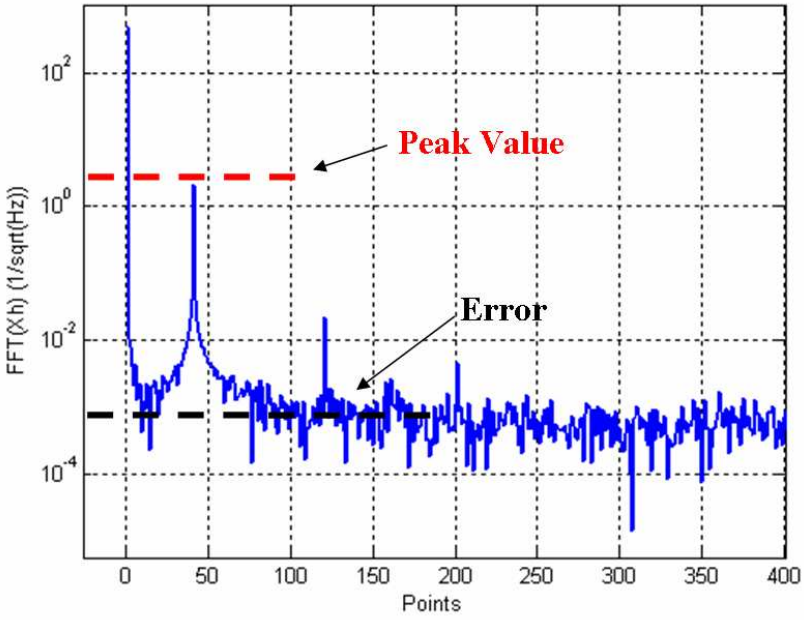

Figure 4.9: Estimate of the error on $FFT(X_h)$. The blue curve represents the function $FFT(X_h)$, while the black dashed line estimates the mean value of the floor noise. The peak indicated in the graph corresponds to the modulation frequency. In order to be identifiable it must stand out from the floor noise level, which thus represents the related error.

position (see figure 4.10). We thus assumed that the difference between the matrix elements was originated by the cross-couplings due to these rotated positions of the detectors.

Calling ξ_x, ξ_y and ξ_z respectively the rotation angles of photodiodes x, y and z, we can estimate them as:

$$tg(\xi_x) = \frac{A_{21}}{A_{11}} \tag{4.12}$$

$$tg(\xi_y) = \frac{A_{42}}{A_{32}} \tag{4.13}$$

$$tg(\xi_z) = -\frac{A_{53}}{A_{63}}. \tag{4.14}$$

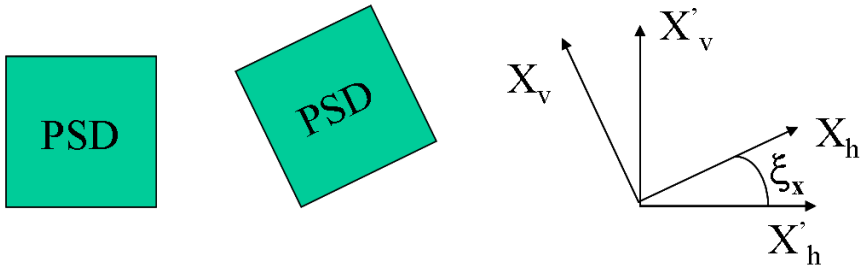

Figure 4.10: Rotated position of the PSD.

The rotation matrix $\mathbf{R}$ corrects the measured matrix $\mathbf{A^{meas}}$ for the rotated positions of the photodiodes:

$$\mathbf{R} = \begin{pmatrix} cos(\xi_x) & sin(\xi_x) & 0 & 0 & 0 & 0 \\ -sin(\xi_x) & cos(\xi_x) & 0 & 0 & 0 & 0 \\ 0 & 0 & cos(\xi_y) & sin(\xi_y) & 0 & 0 \\ 0 & 0 & -sin(\xi_y) & cos(\xi_y) & 0 & 0 \\ 0 & 0 & 0 & 0 & cos(\xi_z) & sin(\xi_z) \\ 0 & 0 & 0 & 0 & -sin(\xi_z) & cos(\xi_z) \end{pmatrix}, \tag{4.15}$$

$$\mathbf{A}_R^{meas} = \mathbf{R} \times \mathbf{A}^{meas}. \tag{4.16}$$

The matrix $\mathbf{A_R^{meas}}$ is the measured matrix corrected for the photodiode rotated positions. Substituting the numerical values in (4.16), we get:

$$\mathbf{A}_R^{meas} = \begin{pmatrix} -1.94 & -0.0126 & 0.173 & - & - & - \\ 0 & -0.0020 & 0.0313 & - & - & - \\ -0.0366 & 0.345 & -0.0427 & - & - & - \\ 0.0094 & 0 & -0.0605 & - & - & - \\ 0.0591 & 0.0298 & 0 & - & - & - \\ 0.0375 & -0.0172 & -1.8388 & - & - & - \end{pmatrix}. \tag{4.17}$$

As it is possible to see comparing the numerical values in (4.17) with the ones in (4.7) and in (4.8), a wrong orientation of the photodiodes doesn't justify the discrepancies between the measured and analytical matrices.

4.3 A setup with invertible optical matrix

A geometrical configuration of the 3-ORO system corresponding to an invertible optical matrix can be obtained by tilting the x beam path by an angle γ around the X axis (see figure 4.11). The analytical matrix relative

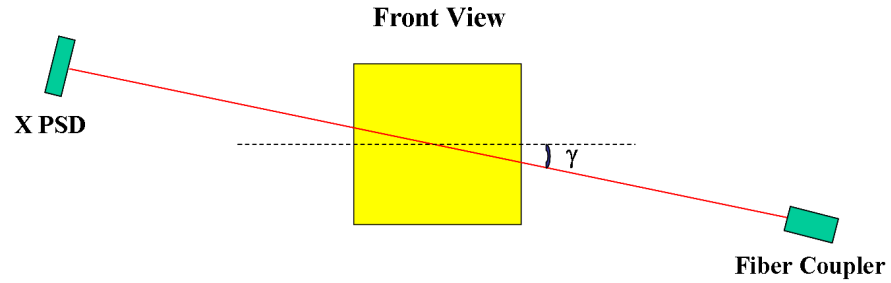

Figure 4.11: Real scale prototype: modified design. A possible value for the angle γ which should require little modification of the present prototype is $\gamma = 16.5°$.

to the new setup is the following:

$$\mathbf{A}^{new}=\begin{pmatrix} -\frac{sin(\pi-2\beta_x)}{cos(\beta_x)} & 0 & 0 & 0 & 0 & 2(L_x+S_x) \\ 0 & -\frac{sin(\pi-2\phi_x)}{cos(\phi_x)} & 0 & 0 & -\frac{2sin(\beta_x)(L_x+S_x)tg(\gamma)}{sin(\phi)} & 0 \\ 0 & \frac{sin(2\beta_y)}{cos(\beta_y} & 0 & 0 & 0 & -2L_y \\ 0 & 0 & 0 & -L_y cos(\beta_y) & 0 & 0 \\ 0 & 0 & 0 & 0 & -2(L_z+S_z)cos(\beta_z) & 0 \\ 0 & 0 & -\frac{sin(\pi-2\beta_z)}{cos(\beta_z)} & -2(L_z+S_z) & -\frac{sin(\pi-2\beta_z)}{cos(\beta_z)}d & 0 \end{pmatrix} \quad (4.18)$$

where the angle ϕ is defined by the relation $tg(\phi) = tg(\beta_x) \cdot tg(\gamma)$. Of course, with $\gamma = 0$ we obtain once more matrix (4.7). All the rows of matrix (4.18) are linearly independent and the matrix can thus be inverted: the six photodiode signals of this new ORO setup completely determine the position of the proof mass in all its DOFs.

4.4 About sensitivity performances

4.4.1 LISA configuration

As I have already mentioned in an earlier section of this chapter, also with the present setup having $\gamma = 0$, the test mass position is completely resolved if we use LISA interferometric signals. Actually this is the current prefered solution for the integration of the ORO sensor in LISA, because in the corresponding configuration no ORO beam would impact the proof mass on the x faces, which are ortogonal to the interferometric axis involved in gravitational wave detection.

The proof mass displacements which are directly measured by LISA interferometer are X, θ and η. The corresponding interferometric signals will be signed with the pedix I of 'ineterferometer' to distinguish them from the ORO measurement. The matrix describing the system is defined in this case by:

$$\begin{pmatrix} X_I \\ \theta_I \\ Y_h \\ Y_v \\ \eta_I \\ Z_v \end{pmatrix} = \begin{pmatrix} 1 & 0 & 0 & 0 & 0 & 0 \\ 0 & 0 & 0 & 0 & 0 & 1 \\ 0 & \frac{sin(2\beta_y)}{cos(\beta_y} & 0 & 0 & 0 & -2L_y \\ 0 & 0 & 0 & -L_y cos(\beta_y) & 0 & 0 \\ 0 & 0 & 0 & 0 & 1 & 0 \\ 0 & 0 & -\frac{sin(\pi-2\beta_z)}{cos(\beta_z)} & -2(L_z{+}S_z) & -\frac{sin(\pi-2\beta_z)}{cos(\beta_z)}d & 0 \end{pmatrix} \times \begin{pmatrix} X \\ Y \\ Z \\ \alpha \\ \eta \\ \theta \end{pmatrix}. \tag{4.19}$$

We call $\mathbf{A_I}$ the matrix 6×6 in equation (4.19) and $\mathbf{B_I}$ its inverse, which represents the optical matrix of the described reference setup.

Substituting the values of expression (4.8) for the relative matrix elements present in $\mathbf{A_I}$ and calculating the corresponding inverse, we get a partially

experimentally verified optical matrix of the system, which we call $\mathbf{B^I}$.

$$\begin{pmatrix} X \\ Y \\ Z \\ \alpha \\ \eta \\ \theta \end{pmatrix} = \begin{pmatrix} B^I_{11} & ... & ... & ... & ... & B^I_{16} \\ ... & ... & ... & ... & ... & ... \\ ... & ... & ... & ... & ... & ... \\ ... & ... & ... & ... & ... & ... \\ ... & ... & ... & ... & ... & ... \\ B^I_{61} & ... & ... & ... & ... & B^I_{66} \end{pmatrix} \times \begin{pmatrix} X_I \\ \theta_I \\ Y_h \\ Y_v \\ \eta_I \\ Z_v \end{pmatrix}. \tag{4.20}$$

4.4.2 How to estimate sensitivity

It is possible to make an estimate of the noise level of the optical sensor measurement in the different DOFs assuming for the ORO the measured sensitivity curve of figure 3.18. We have thus to take into account the geometry of the system, that means its optical matrix.

We consider the reference configuration discussed in the previous subsection, in which X, θ and η are read intereferometrically. We make the reasonable assumption that the noise level of the interferometric measurement is absolutely negligible with respect to the noise relative to the ORO measurement. Then the noise levels we want to estimate are relative to the Y, Z and α DOFs. Taking into account the matrix $\mathbf{B^I}$ defined above, the expected noise for each degree of freedom can be expressed as the incoherent sum of the measured signals weighed by the relative matrix elements. The noise levels $\tilde{Y}$, $\tilde{Z}$ and $\tilde{\alpha}$ relative to Y, Z and α are then given by:

$$\tilde{Y} = \left[(B^I_{23} \cdot \tilde{Y}_h)^2 + (B^I_{24} \cdot \tilde{Y}_v)^2 + (B^I_{26} \cdot \tilde{Z}_v)^2 \right]^{1/2}, \tag{4.21}$$

$$\tilde{Z} = \left[(B^I_{33} \cdot \tilde{Y}_h)^2 + (B^I_{34} \cdot \tilde{Y}_v)^2 + (B^I_{36} \cdot \tilde{Z}_v)^2 \right]^{1/2}, \tag{4.22}$$

$$\tilde{\alpha} = \left[(B^I_{43} \cdot \tilde{Y}_h)^2 + (B^I_{44} \cdot \tilde{Y}_v)^2 + (B^I_{46} \cdot \tilde{Z}_v)^2 \right]^{1/2}. \tag{4.23}$$

Assuming reasonably that the noise level is the same for all the three detectors and that it is equal to the lowest measured noise level $\tilde{y}_s$ obtained with the

rigid setup (black curve in figure 3.18), we get the expected noise for each degree of freedom of our prototype:

$$\tilde{Y} = \left[(B^I_{23})^2 + (B^I_{24})^2 + (B^I_{26})^2\right]^{1/2} \cdot \tilde{y}_s, \tag{4.24}$$

$$\tilde{Z} = \left[(B^I_{33})^2 + (B^I_{34})^2 + (B^I_{36})^2\right]^{1/2} \cdot \tilde{y}_s, \tag{4.25}$$

$$\tilde{\alpha} = \left[(B^I_{43})^2 + (B^I_{44})^2 + (B^I_{46})^2\right]^{1/2} \cdot \tilde{y}_s. \tag{4.26}$$

The calculations can be repeated assuming for $\tilde{y}_s$ the model noise of the ORO sensor.
The results of this analysis are shown in figures 4.12 and 4.13.

4.4.3 The results

Figure 4.12 illustrates the noise levels expected for Y and Z, compared with the capacitive sensor requirement for the translational DOFs. The dashed lines represent the expected model noise levels for Y and Z.
The Y noise level is higher than the Z one because, as I have already pointed out, the relative optical lever incidence angle is smaller.
Figure 4.13 shows the expected noise level relative to α degree of freedom of the prototype, which is below the capacitive sensor specification in about all the bandwidth. Summing up, the layout proposed for the ORO integration in LISA in its analytical model has been validated experimentally. Furthermore, assuming the experimentally demonstrated displacement sensitivity of the ORO (see chapter III) and its potential further improvement, we can predict a noise level for the ORO integration setup within or close to specifications for all the DOFs.

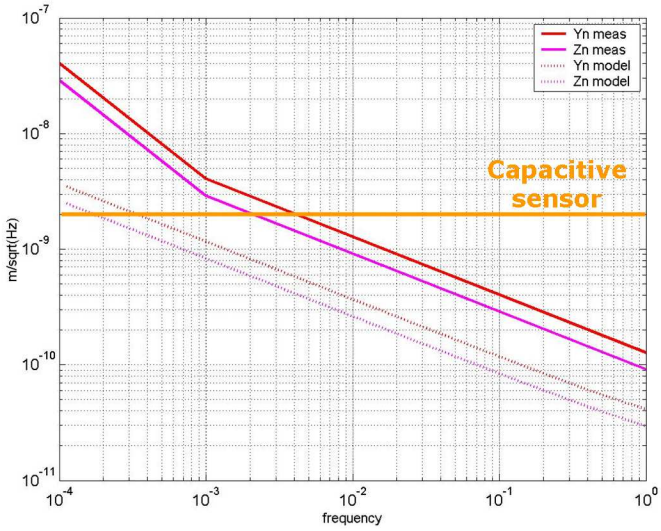

Figure 4.12: Comparison between noise levels relative to the translational DOFs: the orange curve is the capacitive sensor requirement, while the red and magenta curves represent ORO measured noise levels for Y and Z DOFs of the test mass. The dashed lines are the respective ORO potential sensitivities, assuming the model noise.

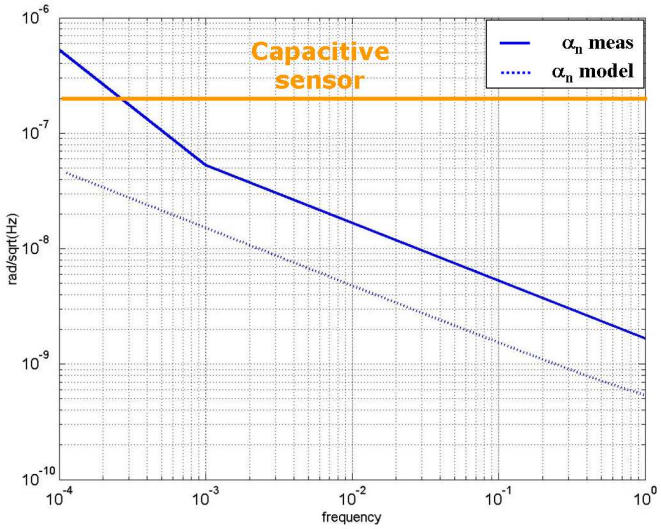

Figure 4.13: Comparison between noise levels relative to the rotational DOFs: the orange curve is the capacitive sensor requirement, while the blue curve represents ORO measured noise level. The dashed line is ORO potential sensitivity, assuming the model noise.

Chapter 5

Ground Testing of the ORO on a torsion pendulum facility

The bench-top measurement described in chapter III and IV have successfully proven that the ORO satisfies the requirements for sensitivity both in translational and in rotational DOFs, overcoming the capacitive sensor performances in a wide range of frequencies. Nevertheless, the rigid bench-top prototypes are not a realistic test stand for the ORO, which will work in space on free falling masses.
Furthermore a rigid setup could not supply measurement of the ORO back-action, due to the radiation pressure of the light beams hitting the test mass, and of other potential unknown interactions.
The installation in Trento of a four mass torsion pendulum facility provides an excellent opportunity to verify the performances of the ORO in a configuration as close as possible to the real one for at least one DOF and to put a relevant upper limit on its induced noise. Moreover it allows to make in-depth comparisons between the ORO and the pendulum capacitive readout system, furnishing a very accurate tool for cross-correlation analysis and for a better estimate of the pendulum mechanical excess noise.
I have already discussed in chapter III that, in order to make preliminary tests in our laboratory in Napoli, we developed a real scale bench-top proto-

type of the ORO designed for integration in Trento ground testing facility. These preliminary measurement gave very good results, analogous to the best ones achieved with the rigid bench-top setup.
After this first experimental validation, for which I refer to dedicated paragraph 3.3.7, we were finally ready to bring the ORO system in Trento and mount it on the torsion pendulum.
This chapter describes the activity concerning the integration of the ORO sensor in the facility and the measurement so far performed. The main part of the experimental work has been accomplished in Trento, were I spent some weeks during my PhD studies.

5.1 The four mass torsion pendulum facility

For each of its test masses LISA demands a nearly perfect free fall along a single translational axis, which is the optical axis of the interferometer. Translational forces along that direction are thus the most important for LISA GRS.
The single mass torsion pendulum described in chapter II is sensitive to torques, rather than to translational forces. Furthermore the force noise that can be achieved with this facility is limited by intrinsic thermal noise of the torsion oscillator and results to be two orders of magnitude above the target force noise for LISA [30].
I mentioned these brief reasonings to introduce the new four mass torsion pendulum facility, which has been developed in Trento in order to improve both the sensitivity of the ground-based measurement and the degree to which they are representative of flight experiments.

5.1.1 The pendulum

The scheme of Trento new pendulum is sketched in figure 5.1. Four LISA-like proof masses (Au-coated, side length: $46\,mm$) are mounted on a cross-shaped support (shaft), with an armlength $b = 10\,cm$ (distance of the proof mass

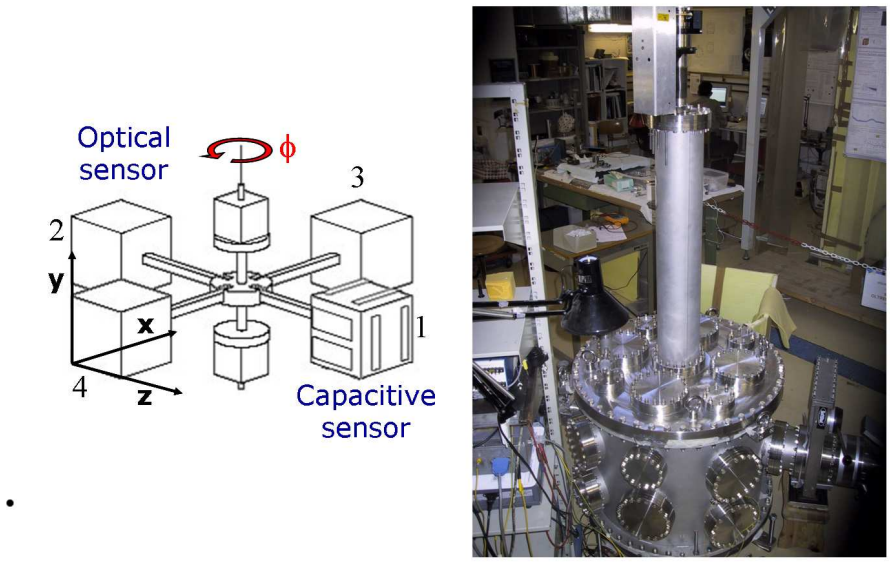

Figure 5.1: Scheme of the four mass torsion pendulum in Trento. Mass 1 is associated to the engineering model of the capacitive readout, while mass 2 deals with the ORO sensor and the so called stiffness compensator. On the right side is shown a picture of the vacuum chamber.

center from the center of the pendulum) [47] [46].

As its single mass companion, the four mass pendulum is hung by a torsion fiber ($L \approx 105\,cm$) to the top of a vacuum chamber. However, differently from the first one, its simple Cavendish type geometry displaces the proof mass from the torsion fiber axis, thus allowing the facility to be sensitive to net forces along the x translational axis.

Referring to figure 5.1, for small rotations ϕ, mass 1 undergoes a translation $x \approx b \cdot \phi$: the x is the so called 'soft DOF' of the proof mass, because in this direction the mass is approximately in free fall. The facility is thus force sensitive along x.

The reference frame we adopt for the displacements of the proof masses is indicated in figure 5.3, together with a sketch of the configuration of the sensors working on the pendulum. The translational DOFs of the proof masses,

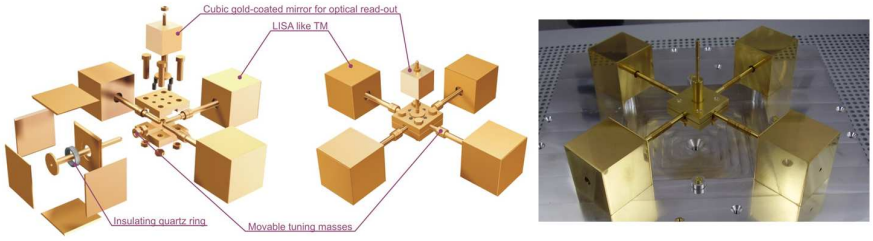

Figure 5.2: The Pendulum. The small cube on top of the pendulum is the mirror on which impinges the autocollimator light beam.

mass 1 and mass 2, are X, Y and Z, while the rotations around the corresponding axes are called θ, ϕ and η. It is worth noticing that X, Y, Z, ϕ and η will be always referred to the displacements of the proof masses, unless it is differently specified.

5.1.2 The sensors

Mass 1 is the proof mass associated to the engineering model capacitive sensor (EM), which represents a real scale prototype of the current solution for LISA GRS. The EM is constituted of six pairs of electrodes, disposed as shown in figure 5.3, which allow to measure test mass 1 displacements in all the six DOFs. The EM electrode housing hosts also the electrodes for electrostatic actuation and the fibers for UV discharge of the proof mass.
Mass 2, or dummy test mass, is instead surrounded by the so called stiffness compensator (STC), a less performant capacitive sensor allowing to compensate the tilt-twist coupling induced on the pendulum by the EM-related stiffness [46]. The STC capacitive sensor is made of three pairs of electrodes, which are visible in picture 5.3. This configuration is sensitive only to the translational displacement of test mass 2.
The ORO sensor acts on mass 2 and is mounted on the STC electrode housing, as we will see in detail later on.
The two electrode housings are installed on a rigid platform and the relative position of the three sensors (EM, STC and ORO) is thus fixed. The proce-

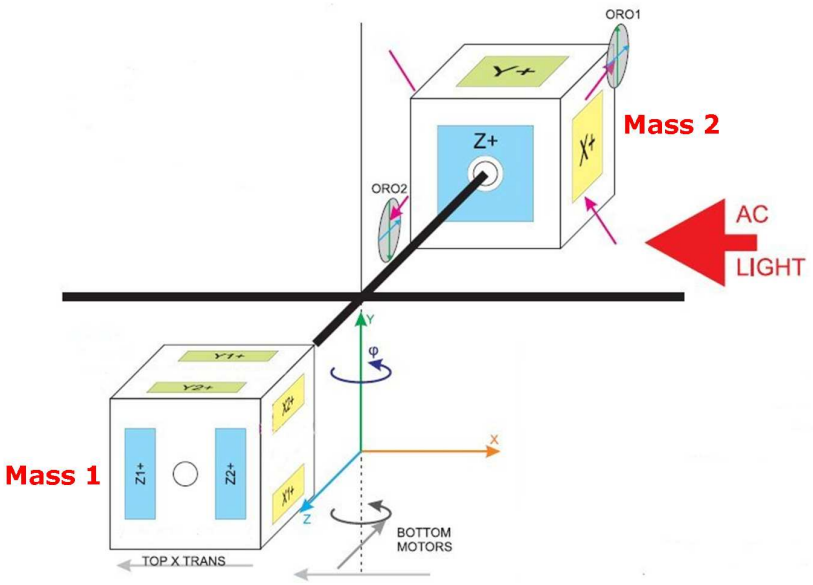

Figure 5.3: Reference frame and of the general orientation of the sensors.

dure aimed at finding the common zero position of the sensors, in order to center them and finally fix them, will be described in section 5.5.
The platform can translate and rotate by means of a micromanipulator.
An autocollimator (AC) located externally to the vacuum chamber sends its light beam to a mirror mounted on top of the pendulum, shown in figure 5.2, measuring the rotations η and ϕ and thus providing the signals for calibrating the EM, ORO and STC sensors.

5.1.3 Other experimental features

The vacuum chamber lays on a concrete slab partially isolated from the laboratory floor. All the experimental setup is enclosed in a large thermally isolated box, except for the acquisition systems.
The working pressure inside the vacuum chamber during the measurement shown in this chapter is around $10^{-7}\,mbar$.
A very important experimental feature is that the signals from the four sensors (EM, ORO, AC, STC) can be visualized in real time on a monitor,

thus providing instantaneous information on the time evolution of the proof masses displacements and on the functioning of the sensors themselves.
This operation is carried out by the Trento acquisition system, which acquires all the signals from the four sensors, together with the temperatures and the pressure inside the vacuum chamber, with a sampling frequency of $10\,Hz$. The signals are then displayed in real time on a monitor as plots in function of time, by means of Labview graphical interfacing.
The real time visualization of the signals is a fundamental tool in the four mass pendulum setup, as I will point out further. In this way we can immediatly become aware, for example, of a possible exit of a light spot from the ORO measurement range or of some problem occurred in the data streams.

5.2 The ORO layout

5.2.1 The geometrical scheme

The ORO configuration planned to work on the torsion pendulum is made up of two optical levers impinging on opposite sides of the dummy test mass, as shown in figure 5.4. The ORO sensors are oriented in opposite directions. The symmetry allows to reduce static force due to the radiation pressure of the light beams hitting the test mass.

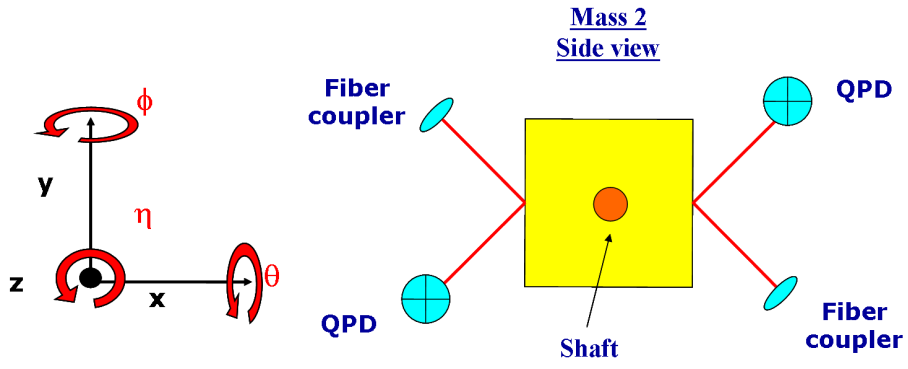

Figure 5.4: ORO configuration on the torsion pendulum.

This layout allows to measure the translational displacements of test mass 2 along the x axis and the rotations ϕ and η around the y and x axes, as it is possible to understand looking at figure 5.5.
A X translation of the test mass causes the light spots to displace along the vertical axes of the photodiodes. In particular, according to the orientation of the ORO sensors shown in figure 5.3, the two vertical displacements have the same sign.
A rotation ϕ of the pendulum results in a rotation ϕ of the proof mass around its center plus a translation of the proof mass center of mass. Consequently, a ϕ rotation of the pendulum causes a displacement of the light spots along both the vertical and horizontal axis of the QPDs. However the ϕ rotation of the proof mass around its center makes the spots displace along the QPDs horizontal axes. The two signals have opposite signs.
A rotation η of the proof mass causes the spots to translate along the vertical axis. The displacements have opposite directions on the two photodetectors.
Of course, the previous reasonings are true if we stop at the first order approximation and neglect the cross-couplings between different DOFs.

5.2.2 Proof mass displacements and ORO signals

The four mass pendulum has different normal modes, corresponding to ϕ (torsional mode) and η (swinging mode) rotations. Furthermore, the pendulum can oscillate around the fiber axis and it also can translate owing to a translation of its suspension point.

Different modes of the pendulum can contribute to a displacement of the proof mass along the same DOF. For example, a translation X of test mass 2 can be caused both by a ϕ rotation of the pendulum or by a translation of the pendulum center of mass by means of a pendulum η rotation. These different motion contributions to a single DOF of the test mass can be distinguished by their proper resonance frequencies, as will be specified in section 5.4, where I will explain the calibration procedure.
From a geometrical point of view, it is possible to characterize the ORO sys-

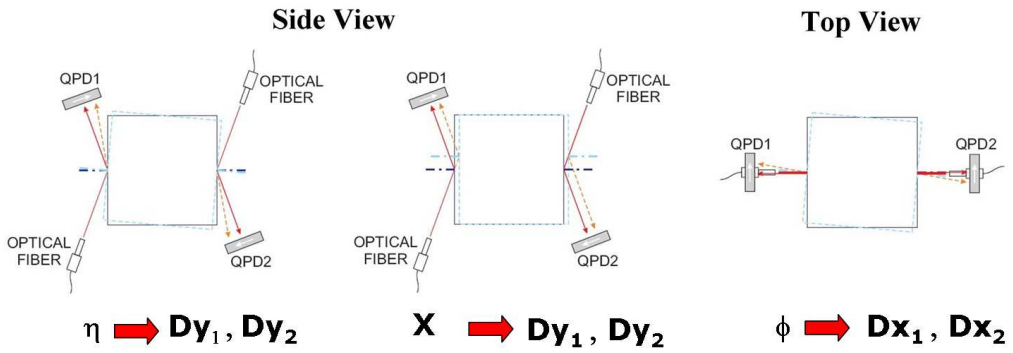

Figure 5.5: Displacements of test mass 2 and ORO signals.

tem relating the displacements of the light spots on the photodiode to the displacements of proof mass 2. For the following discussion I refer to the reference frame and the sensor orientation shown in figure 5.3.
If Dx_1, Dx_2 and Dy_1, Dy_2 are the measured horizontal and vertical displacements of the lights spots on the two photodiodes, the relations between the ORO signals and the proof mass displacements X, ϕ and η are:

$$X = \frac{1}{4sin\alpha}(Dy_1 - Dy_2) \qquad [m], \tag{5.1}$$

$$\phi = \frac{1}{4lcos\alpha}(Dx_1 - Dx_2) \qquad [rad], \tag{5.2}$$

$$\eta = \frac{1}{4l}(Dy_1 + Dy_2) \qquad [rad]. \tag{5.3}$$

The expressions (5.1), (5.1) and (5.1) are obtained by geometrical considerations, stopping at the first order approximation and neglecting the cross-couplings.
Notice that the a single photodiode is sufficient to measure ϕ, but for a better accuracy we consider the mean of the horizontal signals of the two photodetectors.

From a practical point of view, given the measured ORO signals H_N^1, V_N^1 and H_N^2, V_N^2, which are normalized with respect to the sums S_1 and S_2, the

displacements of the test mass measured with the ORO system are:

$$X_{ORO} \propto (V_N^1 - \epsilon V_N^2), \tag{5.4}$$

$$\phi_{ORO} \propto (H_N^1 - \gamma H_N^2), \tag{5.5}$$

$$\eta_{ORO} \propto (V_N^1 + \sigma V_N^2). \tag{5.6}$$

The proportionality constants are the calibration factors. The quantities ϵ, γ and σ take into account the possible differences between the calibration factors of the two photodiodes.

5.2.3 The experimental setup

A basic scheme and a photo of how the ORO is integrated in the STC is shown in figure 5.6, which illustrates a front view of the system: the STC appears as the joint of two L-shaped pieces, on which the fiber couplers and the photodetectors are mounted in the same way described for the bench-top prototype in section 3.3.7.

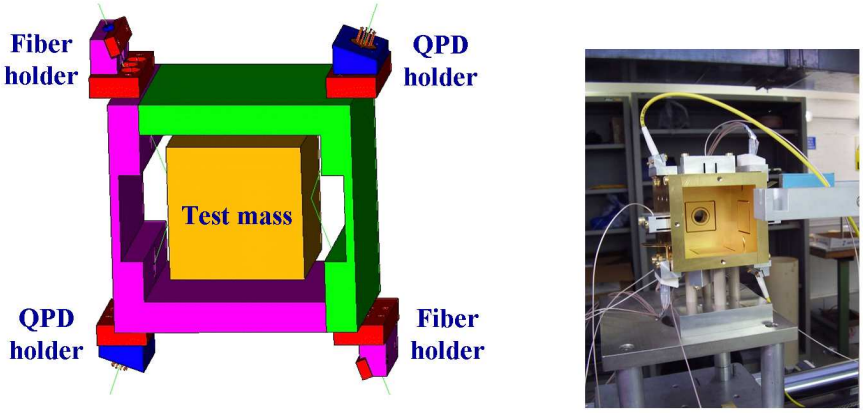

Figure 5.6: Integration of the ORO in the STC.

The holders are the same as in the prototype: the photodiodes are glued to macor holders, which are screwed to the STC through proper interfacing

pieces; the fiber couplers are tightened in between two cilindrical grooves with lateral screws and integrated in the electrode housing with suitable interfacing supports. We made many calibrated interfacing pieces for the photodetector and the fiber couplers, such to readjust the relative positions and allow a good centering of the light spot on the photodiode.
The optical lever armlength and angle are $l = 52.5\,mm$ and $\alpha = 70°$.
The experimental features of the ORO setup on Trento torsion pendulum are the following:

- **Light Sources** $\longrightarrow$ Super Luminescent Light Emitting Diodes ($\lambda = 830\,nm$);
- **Fiber components** $\longrightarrow$ SM optical fibers, Fiber output Couplers: aspheric micro-lenses ($\lambda = 830\,nm$, nominal spot size$= 0.4\,mm$);
- **Sensors** $\longrightarrow$ Quadrant Photodiode (QPD).

The optical fibers and the electric cables of the photodiode enter the vacuum chamber through suitable feedthroughs. It is worth noticing that the optical fibers used so far in the facility are PVC coated and are not suited to deep vacuum, so next step will be to substitute them with hytrel coated ones.

5.2.4 The acquisition system

The acquisition system has been developed and assembled in our laboratory in Napoli. It is based on VME architecture and disposes of 32 not multiplexed channels, with $16\,bit$ analogic-digital converters (Range: $R = 20\,V$ $[-10\,V, +10\,V]$, Sampling frequency: $f_S = 1\,KHz$) and 32 analogic antialisaing filters (8th order Butterworth filters, cutting frequency: $200\,Hz$). The digital data streams can be furtherly filtered with digital antialiasing filters (8th order Butterworth filters) in order to allow an undersampling at desired frequency (usually $10\,Hz$).
The expected acquisition noise level is essentialy the noise level of each analogic-digital converter (ADC), which is estimated as: $\tilde{N}_{ADC} = \frac{R}{2^N} \cdot \sqrt{\frac{1}{f_S}} =$

$20^{-5}\, V/\sqrt{Hz}$.

Actually we have measured the acquisition noise by plugging a channel of

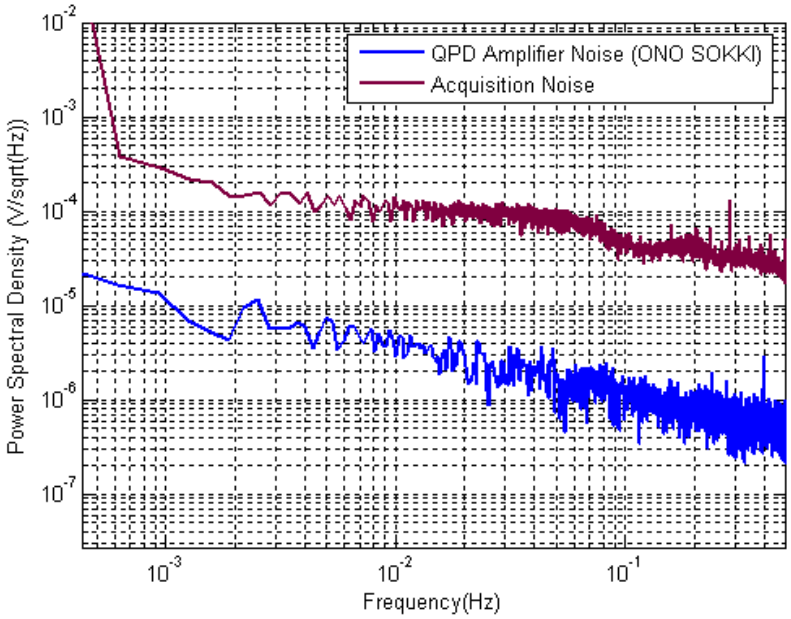

Figure 5.7: Noise level of our acquisition system compared with the electronic noise of the QPD amplifier.

our acquisition system with a $50\,\Omega$ resistance and acquiring the associated signal. It is possible to see from figure 5.7 that the measured acquisition noise is not white as the model predicts. This discrepancy is originated by the antialiasing analogic filters. This is one of the issues we can improve in future steps.

Figure 5.7 also shows the electronic noise of the QPD amplifier, compared with the acquisition noise. This latter is dominant.

In order to use all the voltage range of the ADC and increase the signal to noise ratio between the QPD signals and the acquisition noise, we modified the QPD amplifiers, inserting a switch which allows to change the gain factor of the horizontal and vertical signals from 1 to 20. We call this latter modality 'scientific mode'. Of course when we process the data acquired in scientific mode we must remember to normalize the horizontal and verticl

signals by the factor 20.
It is worth noticing that with gain factor 20, the measurement range on the QPD reduces of a factor 20 too. Considering the spot size $0.4\,mm$, the measurement range becomes $0.02\,mm$. This means that the centering operation of the light spot on the photodiode becomes more difficult and that the spot can easily exit the sensitive area of the photodetector during the pendular displacements.
The signals we acquire are the six signals from the QPDs: S_1, H_1, V_1 and S_2, H_2, V_2. These signals are also acquired with the Trento acquisition system, which allows to display them on a monitor in real time.

5.3 ORO, EM, STC and AC signals

As I have already pointed out, the current ORO layout is sensitive to three DOFs of test mass 2: X, ϕ and η.
Our purpose is to compare the signals measured with the ORO sensor with the signals measured with the capacitive sensors. Therefore, in the following discussion I will consider only the EM and STC signals to be used in the comparison with the ORO sensor.
As it is possible to see from figure 5.3, the STC sensor is made of three couples of electrodes, that we indicate with Z, X and Y. This setup allows the STC to be sensitive only to the translations of test mass 2. In particular, the measurement of the X displacements of proof mass 2 is performed with the STC sensor as:

$$X_{STC} \propto X_{STCV}, \tag{5.7}$$

where X_{STCV} is the voltage signal from the X electrode pair of the STC.
The EM sensor is constituted of 6 pairs of electrodes, called: Z_1, Z_2, X_1, X_2, Y_1, Y_2. From the sum of each pair the relative translational displacement is obtained, while the difference between the signals of the homonymous electrodes give the rotations. So the EM measurement of the X, ϕ and η

displacements of proof mass 1 are obtained from the relations:

$$\phi_{EM} \propto (Z_1 - \delta Z_2), \tag{5.8}$$

$$X_{EM} \propto (X_1 + \tau X_2), \tag{5.9}$$

$$\eta_{EM} \propto (X_1 - \kappa X_2), \tag{5.10}$$

where the factors δ, τ and κ are present for possible differences in the calibration factors of the electrode pairs. Beyond the previous sensors, there is also the AC, which makes independent measurement of ϕ and η, providing the calibration signals for EM, ORO and STC. The output signals ϕ_{AC} and η_{AC} of the AC are directly furnished in degrees.
Summing up, the final signals we deal with are:

- X_{ORO}, ϕ_{ORO}, η_{ORO};
- X_{EM}, ϕ_{EM}, η_{EM};
- X_{STC}
- ϕ_{AC}, η_{AC}.

Actually it is possible to take advantage of the geometry of the pendulum, using both EM and STC or EM and ORO to measure ϕ, improving the sensitivity by means of the armlength of the pendulum. However this way of measuring ϕ is not worth for LISA, so I won't take it into account here.

5.4 Calibration

The calibration is a delicate operation in this context, because of the different pendular normal modes of the four mass pendulum. These modes are the swing and the torsion. Furthermore when the pendulum swings, it also oscillates with respect to the fiber axis. Fortunately this latter oscillation has a high frequency $f \approx 2\,Hz$ and isn't included in the bandwidth we are interested in.

The equilibrium position of the pendulum center of mass can also translate, because its hanging point can move.
The reference signals for calibrating the ORO, EM and STC data are ϕ_{AC} and η_{AC}, as I mentioned in the previous sections.
In order to calculate the calibration factors with the usual method summarized by equation (3.8), we have to consider the different resonant frequencies related to the different pendular normal modes. Typical normalized vertical and horizontal signals from the ORO are shown in figure 5.8.

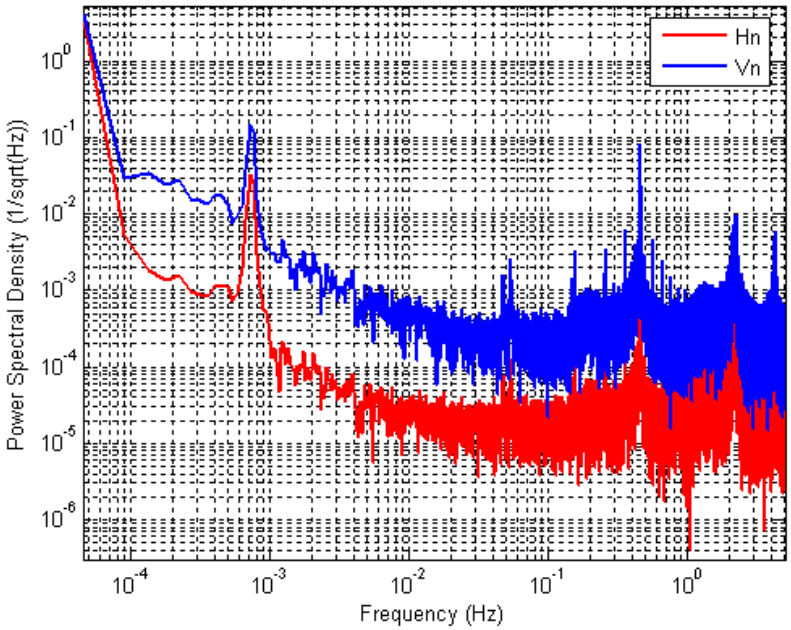

Figure 5.8: Power spectral densities of horizontal (red) and vertical (blue) signals of the ORO operating on the torsion pendulum.

Two main resonant peaks are visible at $f_1 \approx 0.75\,mHz$ and at $f_2 \approx 0.45\,Hz$. The first peak is also visible in $\tilde{\phi}_{AC}$ (figure 5.9), while the second is evident in $\tilde{\eta}_{AC}$, according to the fact that the AC is insensitive to cross-couplings. Indeed, the first resonance corresponds to the torsional mode (rotation ϕ), while the higher frequency peak is associated with the η rotation resonance. The same peaks are visible in the power spectral densities of X_{EM}

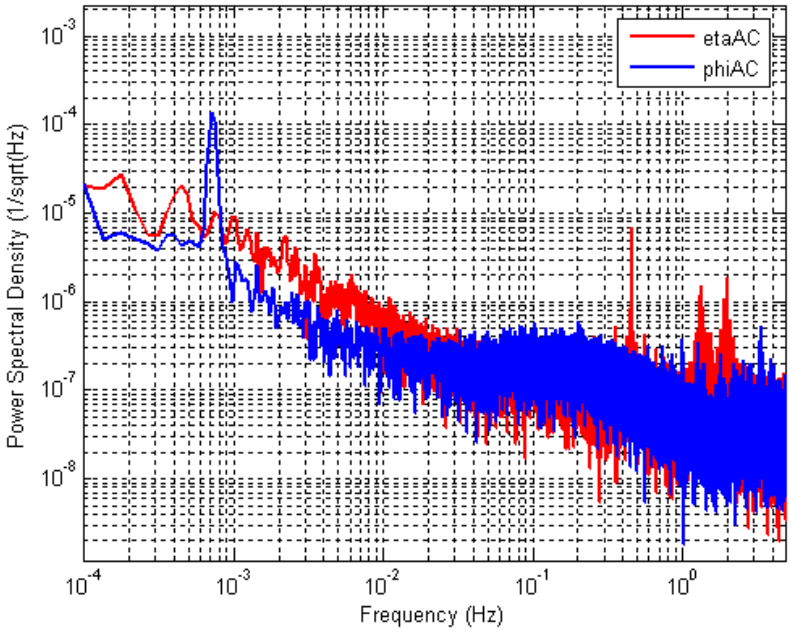

Figure 5.9: Torsion pendulum: power spectral densities of the autocollimator signals.

and X_{STC}, as shown in figure 5.10.

The first peak is thus evident in both ORO signals H_N and V_N, according to equations (5.1) and (5.2). The second peak should be visible only in V_N. Actually we see a smaller peak also in H_N, which is due to cross-coupling. This latter can be caused, for example, by a not perfect alignment of the ORO and the test mass.

Differently from what we used to do for the calibration of the bench-top setups, we do not excite the pendulum with an external force. We use its own pendular normal modes in order to calculate the calibration factors by means of the usual power spectral density method, described in section 3.2.3. We need to pay attention to having properly long lasting measurement, according to the resonant frequency we are taking into account.

The calculation strategy of the calibration factors for the ORO, EM and STC signals is different depending on the proof mass displacement we want to extract.

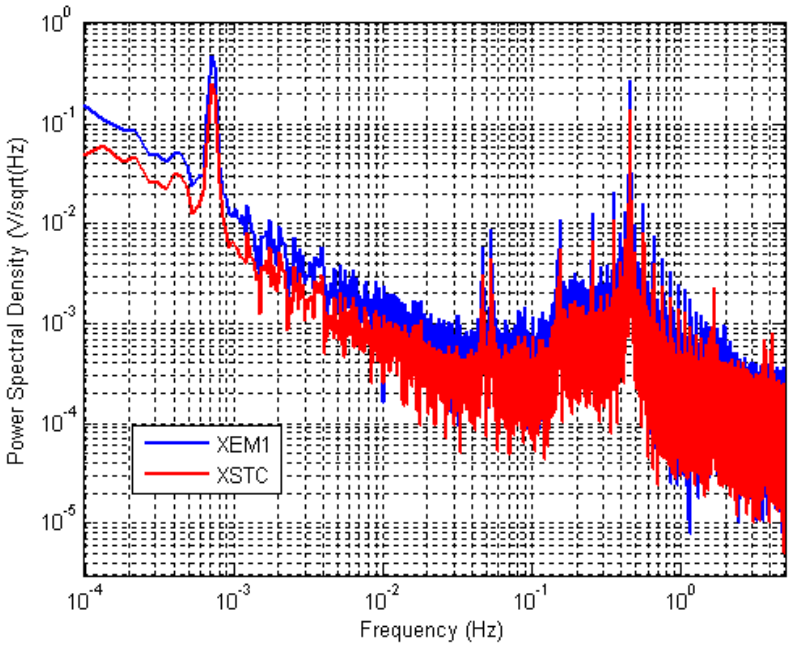

Figure 5.10: Torsion pendulum: power spectral densities of the EM and STC signals, referring respectively to electrodes X_1 of the EM and X of the STC.

5.4.1 Procedure DOF by DOF

The calibration factors relative to ϕ, X and η for the single sensors have been calculated by following the steps described below.

ORO - ϕ DOF

We reasonably assume that at the frequency f_1 the motion of the pendulum is only due to ϕ normal mode. As already mentioned, each horizontal signal of the ORO gives an independent measurement of ϕ, so each H_N^i $(i = 1, 2)$ has to be calibrated singularly against the signal ϕ_{AC}. In this way we get two calibration factors:

$$C^i_{\phi_{ORO}} = \left(\frac{\tilde{H}^i_N}{\tilde{\phi}_{AC}} \right)_{f_1} \quad [rad^{-1}] \qquad \Longrightarrow \qquad \phi^i_{ORO} = \frac{H^i_N}{C^i_{\phi_{ORO}}} \quad [rad] \quad (i = 1, 2). \tag{5.11}$$

Then ϕ_{ORO} is given by the mean of the two different measurement:

$$\phi_{ORO} = \frac{1}{2}(\phi^1_{ORO} - \phi^2_{ORO}) \qquad [rad]. \tag{5.12}$$

It is worth noticing that H^1_N and H^2_N have opposite signs, owing to the orientation of the QPDs and the geometry of the system (see figure 5.3), so in order to calculate the mean and obtain the right sign for ϕ_{ORO}, it is necessary to put the minus sign before ϕ^2_{ORO}.

EM - ϕ DOF

As for the ORO, we assume that the pendulum motion at f_1 is all due to ϕ rotations. In section 5.3 it has been pointed out that ϕ_{EM} is obtained from the difference between the signals Z_1 and Z_2. However, we cannot directly calibrate this difference against ϕ_{AC}, because the two Z electrode pairs have different calibration factors. If δ is the discrepancy factor between the two calibrations of the Z electrodes, the calibration factor is obtained as:

$$C_{\phi_{EM}} = \left(\frac{\tilde{D}}{\tilde{\phi}_{AC}} \right)_{f_1} \qquad [rad^{-1}], \tag{5.13}$$

where

$$D = Z_1 - \delta Z_2 \qquad [V]. \tag{5.14}$$

Owing to the fact that at the resonance frequency all the motion is due to the ϕ normal mode, in order to find δ we have to impose that the two Z electrodes measure the same signal at the frequency f_1. Indeed, in our assumption the signals Z_1 and Z_2 only depend on ϕ at that frequency. So the discrepancy factor is given by:

$$\delta = \left(\frac{\tilde{Z}_1}{\tilde{Z}_2} \right)_{f_1}. \tag{5.15}$$

Finally we get:

$$\phi_{EM} = \frac{1}{C_{\phi_{EM}}}(Z_1 - \delta Z_2) \qquad [rad]. \tag{5.16}$$

ORO - X DOF

We assume that at the frequency f_1 the translational motion X is all due to the ϕ rotation and not to any displacement of the pendulum center of mass. The reference signal for the calibration is now X_{AC}, defined by:

$$X_{AC} = b \cdot \phi_{AC} \qquad [m], \tag{5.17}$$

where b is the pendulum armlength.

As pointed out in section 5.2, X_{ORO} is obtained from the difference between the vertical signals of the ORO system. Following the same reasonings made for calculating $C_{\phi_{EM}}$, we cannot calibrate directly $V_N^1 - V_N^2$ against X_{AC}, because the calibration factors relative to the different QPDs may differ. We calculate the discrepancy factor ϵ in the same way described above:

$$\epsilon = \left(\frac{\tilde{V}_N^1}{\tilde{V}_N^2} \right)_{f_1} . \tag{5.18}$$

The calibration factor is then:

$$C_{X_{ORO}} = \left(\frac{\tilde{J}}{\tilde{X}_{AC}} \right)_{f_1} \qquad [m^{-1}], \tag{5.19}$$

where

$$J = V_N^1 - \epsilon V_N^2 \qquad [V]. \tag{5.20}$$

The X_{ORO} is thus given by:

$$X_{ORO} = \frac{1}{C_{X_{ORO}}} (V_N^1 - \epsilon V_N^2) \qquad [m]. \tag{5.21}$$

EM - X DOF

Each of the two X electrodes of the EM readout measures independently the X DOF of test mass 1. As usual we assume that at the frequency f_1 the signals X_1 and X_2 depend in good approximation only on the ϕ rotations,

rather than on the η rotations. So we can calibrate separately X_1 and X_2 against ϕ_{AC}:

$$C^i_{X_{EM}} = \left(\frac{\tilde{X}_i}{\tilde{X}_{AC}}\right)_{f_1} \quad [m^{-1}] \qquad \Longrightarrow \qquad X^i_{EM} = \frac{\tilde{X}_i}{C^i_{X_{EM}}} \quad [m] \quad (i = 1, 2). \tag{5.22}$$

In the end we calculate the mean value:

$$X_{EM} = \frac{1}{2}(X^1_{EM} + X^2_{EM}) \qquad [m]. \tag{5.23}$$

STC - X DOF

The single pair of X electrodes of the STC allow to measure the X DOF of proof mass 2, by means of the calibration factor:

$$C_{X_{STC}} = \left(\frac{\tilde{X}_{STCV}}{\tilde{X}_{AC}}\right)_{f_1} \qquad [m^{-1}], \tag{5.24}$$

where $\tilde{X}_{STCV}$ is the voltage signal measured by the STC X electrodes. The corresponding displacement is thus:

$$X_{STC} = \frac{\tilde{X}_{STCV}}{C_{X_{STC}}} \qquad [m]. \tag{5.25}$$

ORO - η DOF

The reference signal for the calibration is η_{AC}. Now we assume that at the frequency f_2 all the motion of the pendulum is due to η normal mode.
The measurement η_{ORO} is obtained from the sum of the two vertical signals. As usual, we have to find the discrepancy factor between the calibrations of the two different photodetectors:

$$\sigma = \left(\frac{\tilde{V}^1_N}{\tilde{V}^2_N}\right)_{f_2}. \tag{5.26}$$

The calibration factor is then:

$$C_{\eta_{ORO}} = \left(\frac{\tilde{W}}{\tilde{\eta}_{AC}} \right)_{f_2} \qquad [rad^{-1}], \tag{5.27}$$

where

$$W = V_N^1 + \sigma V_N^2 \qquad [V]. \tag{5.28}$$

The η_{ORO} is thus given by:

$$\eta_{ORO} = \frac{1}{C_{\eta_{ORO}}} (V_N^1 + \sigma V_N^2) \qquad [rad]. \tag{5.29}$$

EM - η DOF

The η DOF is obtained by the difference of the EM signals X_1 and X_2. We calculater the calibration discrepancy factor between the two electrode pairs in the following way:

$$\kappa = \left(\frac{\tilde{X}_1}{\tilde{X}_2} \right)_{f_1}. \tag{5.30}$$

We consider the ϕ resonance because in the power spectral densities of the signals X_1 and X_2 the peak in f_1 is more evident than the peak in f_2.
We calculate the calibration factor as:

$$C_{\eta_{EM}} = \left(\frac{\tilde{M}}{\tilde{\eta}_{AC}} \right)_{f_2} \qquad [rad^{-1}], \tag{5.31}$$

where

$$M = X_1 - \kappa X_2 \qquad [V]. \tag{5.32}$$

The η_{EM} is thus given by:

$$\eta_{EM} = \frac{1}{C_{\eta_{EM}}} (X_1 - \kappa X_2) \qquad [rad]. \tag{5.33}$$

5.5 Assembling phase

The assemblage of the three sensors on the platform proceeded in two main steps: the mounting of the single STC and EM electrode housings, comprehensive of the associated sensors, and their correct positioning and integration on the platform.
Concerning the ORO, the first step consisted in mounting it on the STC electrode housing and in aligning first the two optical sensors and then these latter with the dummy capacitive readout.
Analogously, the two electrode housing must be properly aligned one with respect to the other and consequently fixed to the platform.
The alignment procedure aims at finding the proper relative positioning of the sensors such that all of them measure 0 when the proof mass is in its nominal position. Of course the equality cannot be punctual, but must be worth in a restricted range: a discrepancy up to few μm between the measurement of the sensors is acceptable.

5.5.1 Centering of the ORO sensors and stiffness compensator

In this phase the proof mass n°2 was installed on a long arm mounted of a mechanical translation stage, as shown in figure 5.11, which allowed to translate it along the vertical axis by calibrated steps.

The STC electrode housing including the capacitive electrodes is fixed to a base which is temporarly mounted on a slipping platform, such that the sides of the proof mass and of the electrode housing are parallel. The movable platform allows to translate the electrode housing parallely to the proof mass faces along two ortogonal directions in the horizontal plane. The calibrated displacements of the proof mass and of the electrode housing along the three ortogonal axes are measured with a digital encoder, counting the number of turns of the handles used to carry out the translations.
In picture 5.11 it is also possible to see the two ORO sensors integrated in

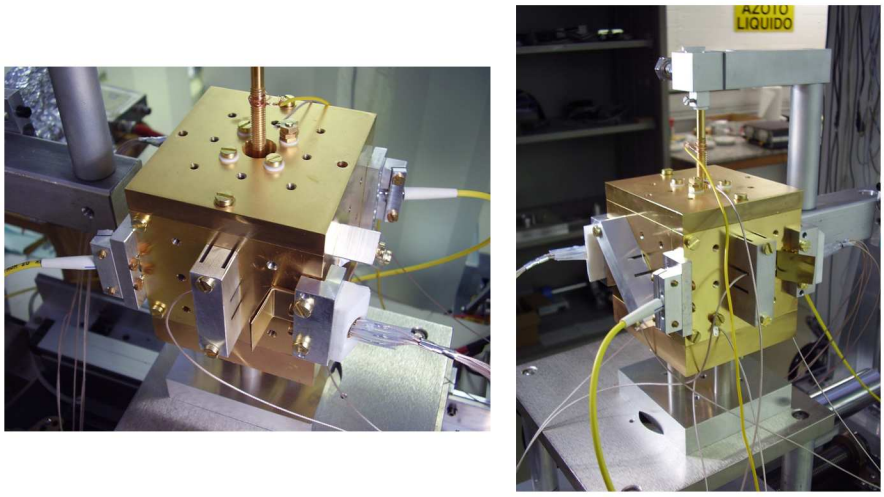

Figure 5.11: Assembling of the ORO sensor on the STC.

the setup.

We assembled the fiber focusers for first. With the proper choice of the calibrated fiber coupler holders, the light beams came out correctly from the relative holes of the electrode housing. Afterwards we mounted the QPDs with the suited calibrated holders, such that the light beams hit the associated sensor. Some corrections were needed in order to position the light spots inside the measurement range of the photodetectors and to center the two ORO sensors: for this purpose calibrated brass spacers are used, inserted in between the electrode housing and the ORO holders and visible in picture 5.11.

After achieving a common zero position with the two ORO sensors, more readjustments were necessary to align both the optical readouts with the STC electrodes.

Figure 5.12 shows the resulting STC (red curve) and ORO (blue curve) X signals after finishing the centering procedure. A rough calibration for the two sensors is obtained by moving the electrode housing by calibrated steps, which are measured with the digital encoder. With a suitable correction of the calibrated factors, we get the curves plotted in figure 5.12: the agreement

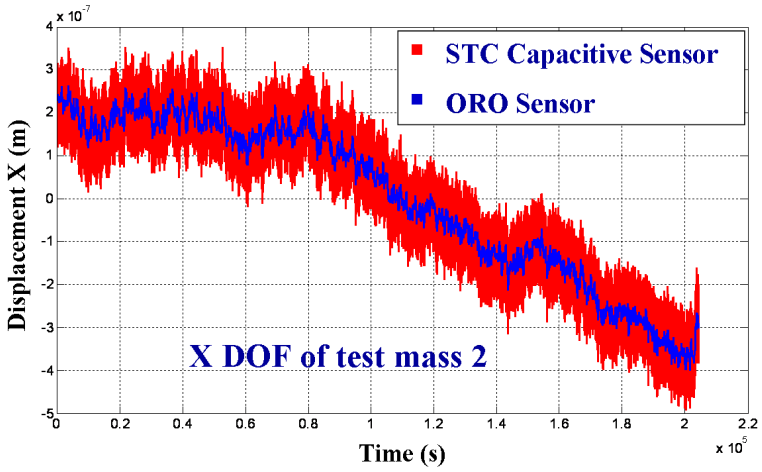

Figure 5.12: Comparison between the signals X_{ORO} and X_{STC} after the alignment of ORO and STC sensors.

is very good and the ORO measurement, as expected, shows a lower level of noise.

5.5.2 Centering of all the sensors

Figure 5.13 shows different moments of the assembling phase of the electrode housings on the platform. As it is possible to see, the body of the pendulum is temporarly fixed on a small column in the center, to simulate the equilibrium position of the pendulum and thus the nominal position of the proof masses.
The EM electrode housing is installed on a translator fixed to the platform. On the other hand the centering of the STC is managed through screws positioned on the sides of its base and beneath it.
As the alignment described in the previous section, the centering of the EM, ORO and STC sensors proceeded by improving approximations, trying to find a common range in which all the readouts measured values close to zero.

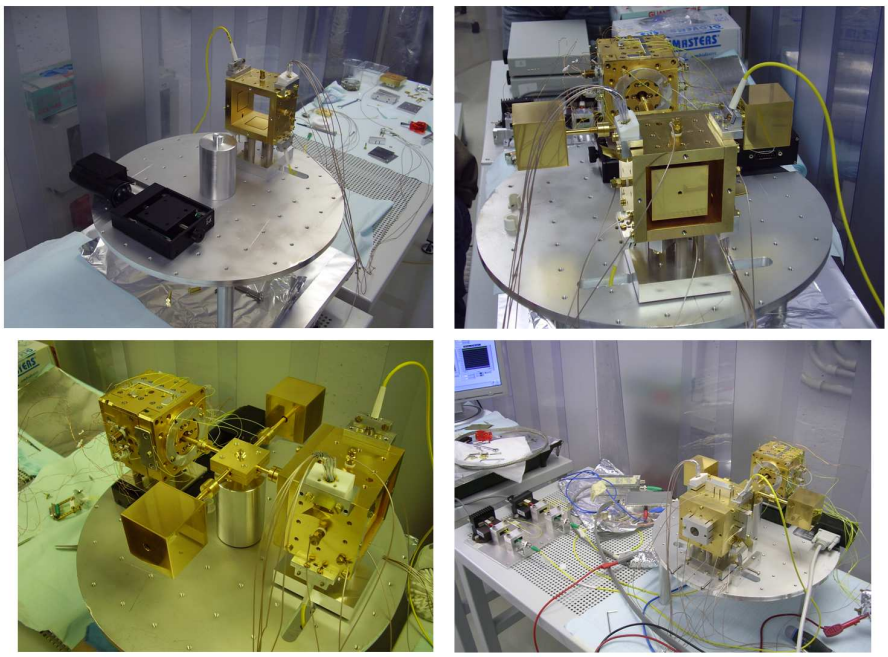

Figure 5.13: Different moments of the assembling of the three sensors on the platform.

5.6 Setting the pendulum for the displacement measurement

After the assembling and centering phases, the pendulum was finally ready to be suspended. I won't give any detail about the suspension stage, because it is pertaining to the work of the Trento group.
I will just give a brief description of the tools used to position the hanging pendulum in the measurement range common to all the sensors, such that it remains in that measurement range for a period of time suitable to the low frequency measurement we are interested to.

The handles we've got in order to move the pendulum are the following:

- it is possible to change the torsional equilibrium angle ϕ_0 by rotating the support of the suspension fiber of the pendulum;
- the vacuum chamber can be tilted by screwing or unscrewing the legs sustaining it, in order to translate the pendulum in the horizontal plane;

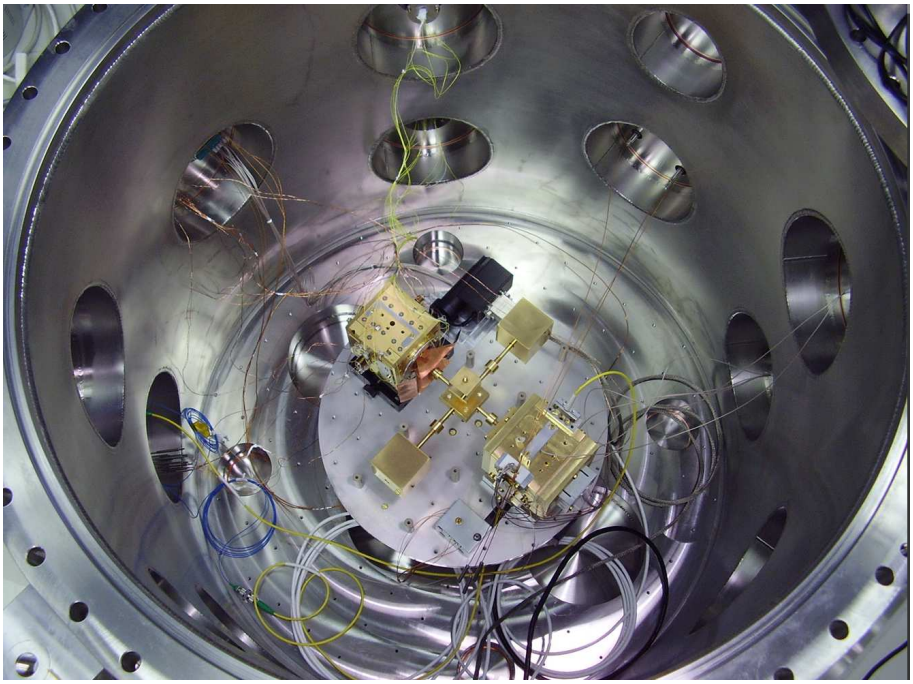

Figure 5.14: The torsion pendulum before suspension.

- it is possible to produce a ϕ rotation by means of electrostatic actuation on the proof masses;
- viscous electrostatic damping is used to slow down and control the swinging pendular normal mode;
- for big swinging oscillation not controlable by the electrostatic damping, it is possible to intervene from the outside by stepping rithmically on the pavement supporting the vacuum chamber, in counterphase with respect to the pendulum swinging mode.

On the other hand, as I have already mentioned, we can rigidly translate and rotate the platform supporting the electrode housings, to readjust the position of the sensors around the proof masses.
In section 5.1.3 I pointed out that the signals from the sensors can be visualized on a monitor. We can thus look at the signals we are interested in, in order to suitably operate on the pendulum by means of the only just

described actions.
It is worth noting that the centering of the pendulum is an exremely delicate operation, which needs much patience and is very time consuming: looking at the signals on the monitor, we have to make an ordered sequence of actions on the pendulum and repeat it very carefully until each signal we are interested in is inside the relative measurement range. Furthermore its oscillation must result properly small and reasonably centered inside the associated measurement range, otherwise the signal will not be measurable for a sufficiently long time, reaching very early saturation.
It is worth noting that if we want to switch the ORO QPD amplifier to the scientific mode, in order to improve the signal to noise ratio between the horizontal and vertical signals and the acquisition noise, the centering conditions of the ORO sensor become the most stringent. This also means that in most cases the ORO signals will be the first ones going out of range.

5.7 First results of the tests on torsion pendulum

The main results achieved so far with the four mass torsion pendulum are illustrated in figures 5.15, 5.16, 5.17 and 5.18. All the measurement accomplished with the ORO sensors shown here are obtained in scientific mode.

Picture 5.15 shows the power spectral density of ϕ DOF measured by the ORO (magenta curve). Unfortunately the Z_1 and Z_2 electrodes of the EM capacitive sensor were not working correctly, owing to a wrong wiring, so we cannot compare the ORO experimental curve with the measured power spectral density of ϕ_{EM}. Instead the expected model noise for ϕ_{EM} is reported (blue line). As it is possible to see from the graph, the ORO sensitivity performance demonstrated so far for the ϕ DOF overcomes the EM expected sensitivity. Furthermore the measured electronic noise of the acquisition system is also plotted (black curve), properly normalized and calibrated: at this stage the ORO ϕ sensitivity is not limited by the acquisition noise. This is

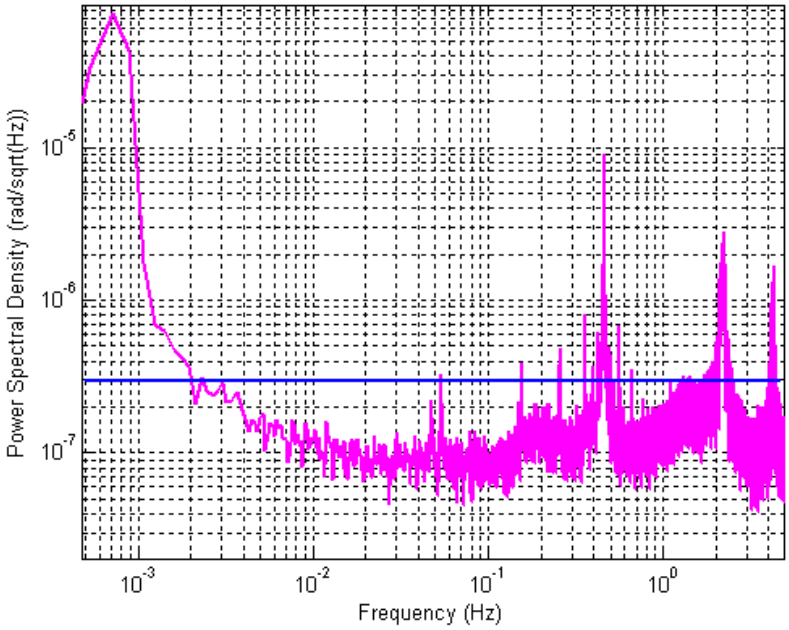

Figure 5.15: Power spectral density relative to the ϕ displacements of the proof mass measured with the ORO sensor (magenta curve) compared with the expected sensitivity of the EM (blue curve).

worth also for the other DOFs, so the next graphs will not show anymore the acquisition noise.

Figure 5.16 shows the the power spectral densities of X_{ORO}, X_{EM} and X_{STC}. It is worth noticing that X_{EM} refers to test mass 2, while X_{ORO} and X_{STC} refer to test mass 1. As it is possible to see, the three sensors measure with very good approximation the same noise level and the features of the curves are very similar. This means that along the X DOF the sensors are dominated by actual motion of the proof masses.

Concerning the rotation η, the results obtained from these first tests are shown in figure 5.17. The power spectral density of η_{EM} is plotted in blue, while η_{ORO} noise is represented by the magenta curve. The ORO performance is slightly better than the capacitive one, although it is not good as expected according to the measurement described in chapter III and IV.

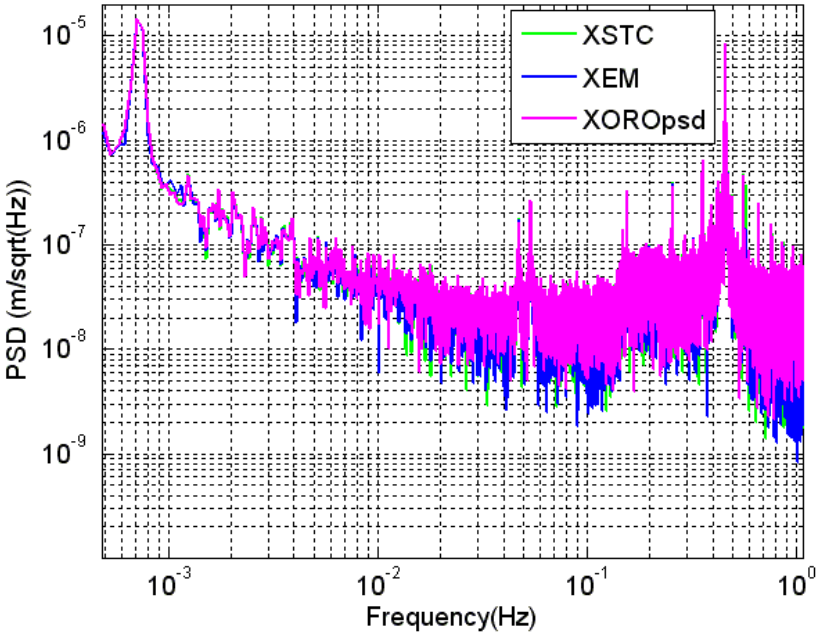

Figure 5.16: Power spectral density relative to the X displacements of the proof masses measured with EM, ORO and STC sensors.

However, it has to be taken into account that all these measurement were performed while the facility was undergoing the debugging phase. Further investigations and new measurement are thus needed.

An interesting result concerns the back-action of the ORO sensor on the pendulum. Figure 5.18 shows the force noise upper limit measured with the EM readout when the ORO is on (blue curve) and off (red curve). There is no evidence of extra-disturbance due to the ORO sensor. Actually the meaured force noise is in good agreement with the thermal noise model expected for the pendulum.

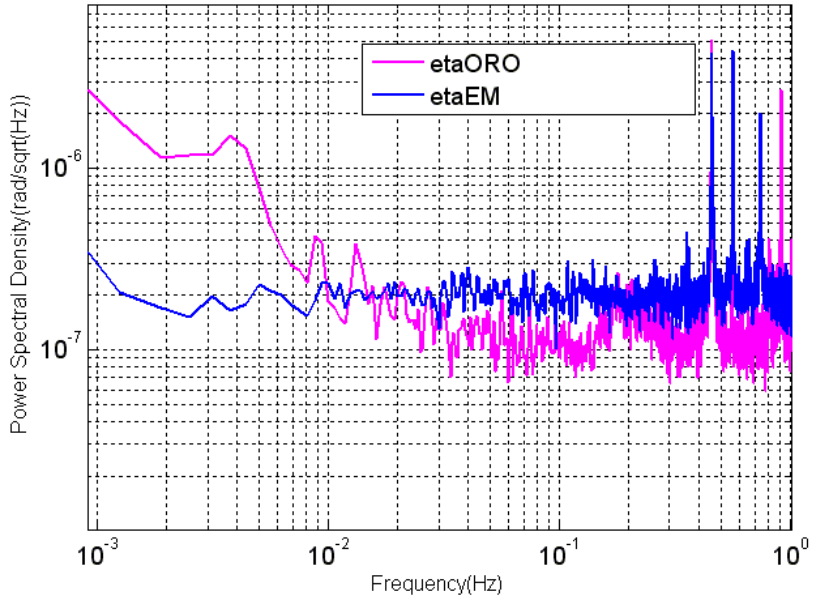

Figure 5.17: Power spectral density relative to the η displacements of the proof mass measured with EM and ORO.

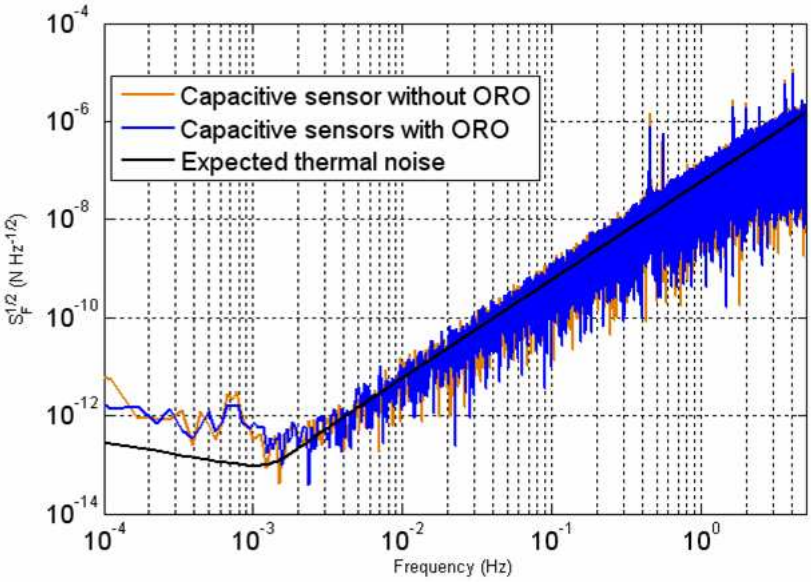

Figure 5.18: ORO Back-action.

Conclusions

The research activity described in this thesis has lead to the development of an optical readout (ORO) system based on optical levers to be integrated in the Gravitational Reference Sensor (GRS) of LISA, providing a backup solution in case the main sensor fails. This latter is a capacitive readout developed by the LISA group in Trento.
The proposal of an ORO based on optical levers dates back to 200, before I joined the LISA group of Napoli. However at that time the ORO was at a very initial stage and the experimental testing was at its first steps.
My work has developed around three main topics:

- Characterization of the sensitivity of the ORO;
- Integration of the ORO in LISA;
- Test of the ORO on the 4 mass torsion pendulum facility in Trento.

A rigid bench-top setup has been used for characterizing the ORO sensitivity in the LISA frequency band $10^{-4}\,Hz - 10^{-1}\,Hz$. Many different experimental configurations have been tested, in order to improve the ORO performances and identify the proper optical devices to propose as guide-line solutions for the integration in LISA GRS. On the base of the experimental analysis, the identified reference solutions are the following:

The bench-top experiments demonstrated that the sensitivity performances of the ORO sensor overcome the capacitive sensor specifications in the whole frequency band of interest. The improvement ranges from a factor of 2 at $1\,mHz$ to a factor of 20 at $100\,mHz$. At lower frequencies, below $0.5\,Hz$, the

ORO noise spectrum exceeds the design sensitivity of the capacitive readout, showing a steeper slope. We think that this is mainly due to thermal and mechanical drifts, rather than to sensor intrinsic noise.
It is worth noticing that the ORO measured sensitivity is better than the one of the capcitive sensor, despite the fact that ORO has not yet reached its potential limit, which is established by the electronic noise of the QPD amplifier. Actually, the ORO shows an excess noise in a factor 4 with respect to the model noise. Many different tests have been made in order to identify the cause of this extra-noise, but its origin has not yet been understood. However, being optimistic, the fact that the currently measured ORO sensitivity is not limited by fundamental noise sources means that further improvements are still possible.
The better sensitivity of the ORO compared to the capacitive readout allows a remarkable relaxation of the cross-coupling conditions. Taking into account the capacitive sensor specifications, the upper limit on the cross-coupling among different DOFs is 0.1% above $1\,mHz$, that is a very demanding experimental condition, especially for a space mission. On the other hand, if the ORO is considered, the upper limit relaxes to 1% over almost all the frequency band.

A possible integration scheme of the ORO in LISA has been proposed in [43], taking into account the current electrode housing model of LISA Pathfinder, which is the most realistic layout available at the moment. In this setup some electrodes are used as mirrors, for directing the light beams through the very small spaces within the electrode housing. Following that scheme, a real scale prototype has been developed and tested. This allowed to validate the proposed integration solution. In particular the optical matrix of the system has been calculated and compared to the measured one, giving an agreement within few percents.
It is worth noticing that this activity din't aim at sensitivity studies, so the photodetectors in use were PSDs. In order to estimate the sensitivity per-

formance of the setup, we took into account the sensitivity curves measured with the rigid bench-top setup and applied the analytical matrix of the system. The results are that also in this layout the ORO sensitivity overcomes the capacitive readout sensitivity for both the translational and rotational DOFs in a wide range of frequencies. If the potential sensitivity is taken into account, the improvement is verified in all the bandwidth we are interested in.

For what concerns the third topic, a suitable ORO layout has been developed for integration in the four mass torsion pendulum facility in Trento. The pendulum represents a realistic test stand for the sensors, because the proof masses approximate free fall along one DOF.
The aims of the integration of the ORO in the facility are thus the verification of ORO sensitivity performances in a more realistic configuration than the bench-top setups; in-depth comparisons between the ORO and the pendulum capacitive readout system; the measurement of the ORO back-action.
The assembling of the ORO and capacitive sensors and the final suspension of the pendulum were accomplished in May 2007. The results obtained from the first measurement are encouraging, even though the facility was still undergoing the debugging phase and some electrodes of the capacitve readout were not working correctly. It was thus not possible to make an exhaustive comparison.
For what concerns the back-action of the ORO on the pendulum, the performed measurement showed no evidence of disturbance introduced by the optical sensor.
The ORO is now in operation on the pendulum and a complete characterization is going on.

Therefore, next steps concern on one side further measurement and investigations on the pendulum facility in Trento. On the other side other kind of light sources, as the FBG and DFB laser diodes, are planned to be tried out and new bench-top tests are required in order to identify the residual noise,

preventing the ORO from reaching the model sensitivity.
Further studies are necessary to bring the proposed ORO from the laboratory breadboarding phase to the status of reliable flight hardware. This requires the development of an engineering model to be assembled with space qualified components and to be tested on different aspects (vacuum, vibration, thermal, radiation, etc...), according to space qualification standards.
For this purpose a proposal for funding has been recently submitted by our group to the Italian Space Agency (ASI), in collaboration with an industrial partner experienced in space hardware development (Carlo Gavazzi Space S.P.A.).

In conclusion, we have proposed a solution for the LISA GRS which is simple and reliable, thus cheap and robust. These peculiarities, together with the small overall dimensions of the devices, are fundamental features for space operation and make the ORO a very worthy candidate, also compared to potentially more sensitive alternative optical sensors. Furthermore the proposed integration scheme has demonstrated to be a valid baseline solution.
The results obtained so far show that the principle layout is already mature enough for being adopted as a useful device in the design of LISA. We believe that the ORO sensor is ready for the engineering and qualification studies.
Bearing in mind that, in case of successful testing on LISA Pathfinder, the capacitive readout will certainly be integrated in LISA, we think that the better sensitivity of the ORO suggests that it becomes the main sensor, while the capacitive system can be kept as a backup. The main advantage would be to facilitate the achievement of LISA design sensitivity, owing to the relaxation of the very demanding specifications on cross-couplings for the drag-free control loop.

Appendix A

Technology transfer in other fields: ORO applied to VLT Survey Telescope

One of the fascinations of developing a handy technological device is that it can be used in very different fields, so it offers the stimulating possibility of cooperating with groups working at very unlike experiments. This has been the case of the ORO, which found a very useful application in the VLT (Very Large Telescope) Survey Telescope, the so called VST apparatus.
The VLT array is a huge ground-based astronomical observatory, built on the top of Cerro Paranal in northern Chile. It constitutes the flagship facility of the ESO (Europeen Southern Emisphere Observatory) [48].
The development and the building of the VST has been carried out by a team of researchers of the INAF (Istituto Nazionale Astrofisica) in Napoli, entrusted with the project by the ESO [49]. The building has begun since few years in the site of the Mecsud factory in Scafati and has been completed one year ago. Part of the apparatus has been carried to the Cerro Paranal observatory between June and August 2007. However, some of its subsystems are still undergoing the qualification phase and the validation tests and will be sent to South America in the first months of 2008.

A.1 The collaboration

A.1.1 The aims of the collaboration and the ORO setup

The collaboration between the VST group and ours concerns the characterization and the qualification of the system for the positioning and the orientation of the secondary mirror (M2) of the VST. A picture of the VST basic structure in Scafati is shown in figure A.1, where the location of the mirror M2 is indicated on top of the setup.

In the final configuration the mirror M2 can be moved in all the 6 DOFs by

Figure A.1: The VST being built in Scafati.

means of two parallel robots, the so called hexapodes, arranged in cascade.

Hexapode 1 is constituted by idraulic actuators with an encoder readout. It allows to carry out relatively large displacements with medium resolution. Hexapode 2 is made of piezo-electric actuators with capacitive readout. It has a better resolution and allows only small displacements.
Both robots dispose of sensors which measure the elongation of the actuators, but not directly the mirror displacements. Here is where the ORO comes into play: three suitably oriented optical sensors provide an independent readout system which measures directly the mirror displacements in all the six DOFs, allowing an independent characterization of the action of the two hexapodes.
Figure A.2 shows the hexapode testing facility in Scafati. The two robots

Figure A.2: VST: the hexapodes, the dummy secondary mirror and the relative ORO setup.

support an aluminum cylinder on the bottom, identical in shape to the secondary mirror, which consitutes a dummy of M2.
The ORO layout in the VST is shown in figure A.3. An important feature of this setup is that the three PSD sensors are integral with the mirror, while the fiber couplers are fixed to the external still structure. Furthermore there is no reflection of the light beam, which goes straight from the focuser to the photodetector. This sensing configuration is absolutely simpler than a real

optical lever.
In picture A.2 the two lateral ORO sensors are visible with their associated yellow optical fibers. A detail is illustrated in figure A.4, where a close-up of a fiber coupler (aspheric micro-lens, diameter: $3\,mm$, $\lambda = 830\,nm$) and of a PSD illustrates the basic detection scheme.
On the desk in front of the apparatus (figure A.2) it is possible to see the SLED sources ($\lambda = 830\,nm$) mounted in their holders (figure A.2). These latter are the same we have developed for the tests on the pendulum facility in Trento. They are shown with greater detail in figure A.5.

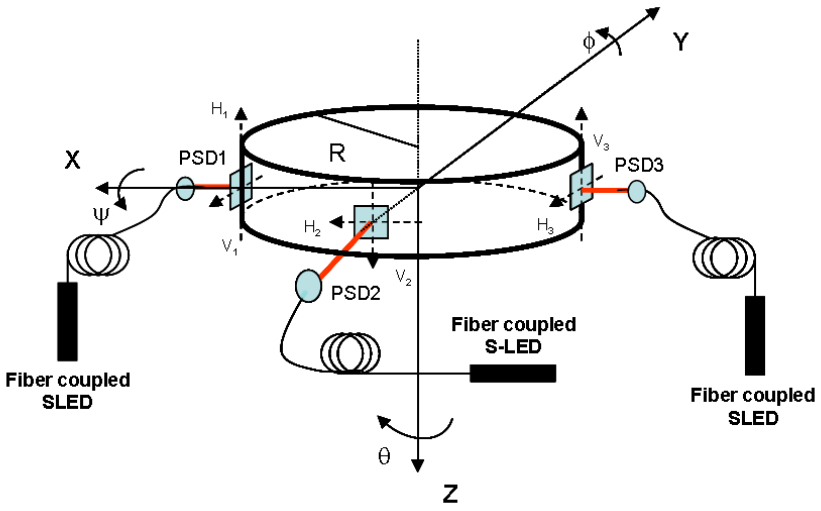

Figure A.3: ORO layout in the VST.

A.1.2 Main topics

Our collaboration with the VST group was splitted in two main parts:

- the activity concerning the development of the proper solution to the problem, accomplished in our laboratory;

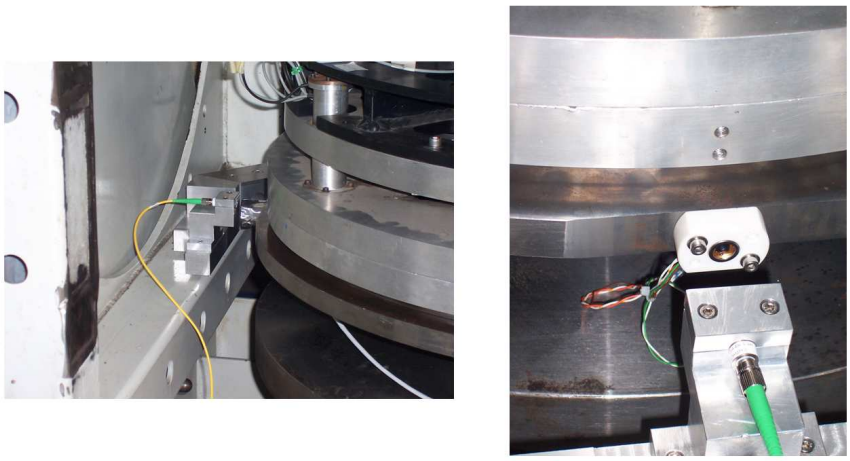

Figure A.4: Detail of the ORO setup on the VST: fiber collimator and PSD.

- the experimental activity carried out in Scafati, mainly the istallation of the ORO on the VST and the testing of the ORO-Hexapodes setup.

The first part concerned, among other things, the accurate calibration of the PSDs to be mounted on the VST and the verification of the constance of the calibration factor in the measurement range of the photodetector, through a grid of repeated measurement over the sensitive area.
Furthermore my 'desk' activity dealed with calculation of the optical matrix, characterizing the ORO system and relating the actual displacements of mirror M2 with the horizontal and the vertical displacements of the 3 light spots on the photodiodes. If Dx_i, Dy_i (i = 1, 2, 3) are respectively the horizontal and vertical light spot displacements measured by the PSDs, the mirror displacements X, Y, Z, ψ, θ and ϕ are expressed by:

$$\begin{pmatrix} X \\ Y \\ Z \\ \psi \\ \theta \\ \phi \end{pmatrix} = \begin{pmatrix} \frac{1}{2} & 0 & -1 & 0 & \frac{1}{2} & 0 \\ -\frac{1}{2} & 0 & 0 & 0 & \frac{1}{2} & 0 \\ 0 & -\frac{1}{2} & 0 & 0 & 0 & \frac{1}{2} \\ 0 & -\frac{1}{2R} & 0 & \frac{1}{R} & 0 & \frac{1}{2R} \\ 0 & \frac{1}{2R} & 0 & 0 & 0 & \frac{1}{2R} \\ -\frac{1}{2R} & 0 & 0 & 0 & -\frac{1}{2R} & 0 \end{pmatrix} \times \begin{pmatrix} Dx_1 \\ Dy_1 \\ Dx_2 \\ Dy_2 \\ Dx_3 \\ Dy_2 \end{pmatrix}, \qquad \text{(A.1)}$$

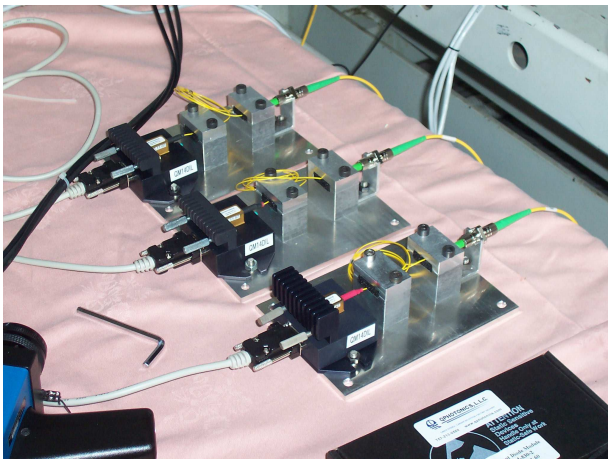

Figure A.5: LED sources mounted on supports in the VST ORO setup.

where R is the radius of the mirror ($R = 30\,cm$).

The work I performed concerning the topics of this collaboration doesn't come within the purposes of this thesis and constituted a minor part of my PhD reasearch. This is the reason why I decided not to include the argument in the chapters and to dedicate to it only an appendix of my PhD thesis. For further details I refer to the article concerning our collaboration with the INAF group (reference [45]).

Bibliography

[1] M. Kramer et al. 2006. *Tests of general relativity from timing the double pulsar.* Science Express, Sept 14, 2006, astro-ph/0609417.

[2] J. Weber. 1960. Physical Review, 117, 306.

[3] P. R. Saulson. *Interferometric Gravitational Wave Detectors.* World Scientific, 1994.

[4] M. Bassan. 1994. Class Quant Grav, Supplement A 39, 11.

[5] Official website of AURIGA: www.auriga.lnl.infn.it;

[6] R. M. Wald. *General Relativity.* The University of Chicago Press, 1984.

[7] S. Weinberg. *Gravitation and Cosmology. Principles and Applications of the General Theory of Relativity.* Wiley, 1972.

[8] C. W. Misner, K. S. Thorne e J. A. Wheeler. *Gravitation.* Freeman and Company, 1970.

[9] K.S.Thorne. *Gravitational Radiation - A New Window onto the Universe.* arXiv: gr-qc/9704042 v1 15 Apr 1997.

[10] Official website: http://www.ligo.caltech.edu/

[11] Official website: http://geo600.aei.mpg.de/

[12] Official website: http://tamago.mtk.nao.ac.jp/

[13] Official website: http://www.virgo.infn.it/

[14] *AIGO Prospectus.* Available at: http://www.gravity.uwa.edu.au/docs/aigo-prospectus.pdf.

[15] *LISA: A Cornerstone Mission for the Observation of Gravitational Waves.* System and Technology Study Report. ESA-SCI(2000)11. July 2000.

[16] H. Kogelnik, T. Li. *Laser Beams and Resonators.* Proc. IEEE, vol 54,pp. 1312-1329, Oct. 1966.

[17] Sensitivity Curve Generator for Spaceborne Gravitational Wave Observatories. Available at:

[18] J. Baker et al.. *LISA: Probing the Universe with Gravitational Waves.* LISA-List-RP-436. January 2007. Available at:

[19] T. Prince, K. Danzmann. *LISA Science Requirements Document.* LISA-ScRD-004. January 2007. Available at:

[20] J. W. Armstrong. 1999. The Astrophysical Journal, 527:814-826,1999 December 20.

[21] M. Tinto, S. V. Dhurandhar. *Time Delay Interferometry.* Living Rev. Relativity, 8, (2005), 4. [Online Article]: http://www.livingreviews.org/lrr-2005-4.

[22] M.Tinto et al.. 2002. *Time Delay Interferometry for LISA.* Physical Review D, Volume 65, 082003.

[23] Scott A. Hughes. *A brief survey of LISA sources and science.* Proceedings of the Sixth LISA International Symposium, Eds. S. Merkowitz, J. Livas, AIP Conf Series 873.

[24] A. Stroeer, A. Vecchio. 2006. *The LISA verification binaries.* Class Quant Grav 23 S809-S817.

[25] A. Toomre. 1977. *Mergers and some consequences.* In *Evolution of Galaxies and Stellar Populations*, Eds. B. Tinsley, R. Larson; Yale University Press, 401-426.

[26] E. Bell et al. 2006. *The merger rate of massive galaxies.* ApJ652, 270-276.

[27] M. Volonteri. 2006. *Supermassive black hole mergers and cosmological structure formation.* Proceedings of the Sixth LISA International Symposium, Eds. S. Merkowitz, J. Livas, AIP Conf Series 873, 61-69, astro-ph/0609741.

[28] C. Hopman. *Astrophysical of extreme mass ratio inspiral sources.* Proceedings of the Sixth LISA International Symposium, Eds. S. Merkowitz, J. Livas, AIP Conf Series 873, astro-ph/0608460.

[29] S. A. Hughes. *(Sort of) Testing relativity with extreme mass ratio inspirals.* Proceedings of the Sixth LISA International Symposium, Eds. S. Merkowitz, J. Livas, AIP Conf Series 873, gr-qc/0608140.

[30] *LISA PF project. Reshaping of the workplan: optical readout system and advanced on ground test facility at LNGS. May 20, 2004.*

[31] C. C. Speake and S. M. Aston. *An interferometric sensor for satellite drag-free control.* Class. Quantum Grav. 21 (2005) S269-S277.

[32] S. M. Aston, C. C. Speake. 2006. *An Interferometric Based Optical Read-Out Scheme For The LISA Proof-Mass.* Pro-

ceedings of the Sixth LISA International Symposium, Eds. S. Merkowitz, J. Livas, AIP Conf Series 873,326-333.

[33] G. Allen et al.. *Using an optical fiber fed Littrow cavity as a displacement sensor for use in drag-free satellites.* Proceedings of the Sixth LISA International Symposium, Eds. S. Merkowitz, J. Livas, AIP Conf Series 873, 334-338.

[34] T. Schuldt et al.. 2006. *A high sensitivity heterodyne interferometer as opical readout for the LISA inertial sensor.* Proceedings of the Sixth LISA International Symposium, Eds. S. Merkowitz, J. Livas, AIP Conf Series 873, 374-378.

[35] Chiao M P, Dekens F and Abramovici A. 2003. *Gravitational-Wave Detection.* Proc. SPIE 4858, p. 98. Ed. M. Cruise and P. Saulson.

[36] S. Vitale et al., 2006. *Achieving the mid-low end of the LISA band.* Proceedings of the Sixth International LISA Symposium, Eds. S. Merkowitz, J. Livas, AIP Conf Series 873.

[37] L. Carbone et al., 2003. *Achieving geodetic motion for LISA test masses: Ground testing results.* Physical Review Letters 91, 151101.

[38] L. Carbone et al., 2004.*Characterization of disturbance sources for LISA: torsion pendulum results.* Classical and Quantum Gravity, Dec 2004, arXiv:gr-qc/0412103.

[39] L. Carbone. 2005. *Ground based investigation of force noise sources for LISA.* PhD Thesis, University of Trento.

[40] M. Hueller. 2004. *Geodesic motion of LISA test masses: development and testing of drag-free position sensors.* PhD Thesis, University of Trento.

[41] S.O. Kasap. *Optoelectronics and photonics. Principles and Practices.* Prentice Hall, 2001.

[42] F. Acernese, E. Calloni, R. De Rosa, L. Di Fiore, L. Garcia, L. Milano. *An optical readout system for the LISA gravitational reference sensors.* Class. Quantum Grav. 21 (2004) S621-S627.

[43] F. Acernese, E. Calloni, R. De Rosa, L. Di Fiore, L. Milano. *An optical readout system for the drag-free control of LISA.* Class. Quantum Grav. 22 (2005) S279-S285.

[44] F. Acernese, R. De Rosa, L. Di Fiore, F. Garufi, A. La Rana, L. Milano. *Some Progress in the Development of an Optical Readout System for the LISA Gravitational Reference Sensor.* Proceedings of the Sixth International LISA Symposium (2006), pp. 339.

[45] P. Schipani, L. Ferragina, L. Marty, A. Grado, L. Di Fiore, R. De Rosa, A. La Rana, A. Buratta. *Parallel robots in a ground-based telescope active optics system: theory and experiments.* Proceedings of SPIE (2007), vol. 6715, pp. 671503-1/671503-9.

[46] L. Carbone et al., 2006. *Torsion Pendulum Facility for direct force measurement of LISA GRS related disturbances.* Proceedings of the Sixth International LISA Symposium, Eds. S. Merkowitz, J. Livas, AIP Conf Series 873.

[47] L. Carbone, A. Cavalleri, R. Dolesi, C.D. Hoyle, M. Hueller, S. Vitale, W.J. Weber. *4-Mass torsion pendulum for ground testing of LISA displacement sensors.* Proceedings of the 10th Marcel Grossmann Meeting on General Relativity, 2004, arXiv:gr-qc/0411049.

[48] Official website: http://www.eso.org/paranal/.

[49] Official website: http://vstportal.oacn.inaf.it/.

Acknowledgments

Now that my feet are back to the ground and the sky I look at is once more the reassuring blue roof on top of my head, I glance at the recent memories and already miss the crucial moments of this beautiful space adventure.
I feel grateful to the people which have driven me through and to the ones that have simply shared with me the travel.
First of all I thank my Master and Guide, Luciano, who took me on board and taught me the 101 secrets in order to succeed in a space mission, including to remedy an error keeping on smiling. For all the Hawaiian dancers, working side by him is really cool! In these three years he has been a real example for me.
My special thanks go to my Captain, Prof. Milano, the gentlehearted sidereal traveller who drives across the stars the VIRGOLab spacecraft. He looks into the deepness of space with the same care and humanity he looks at people. Thank you for teaching me about the stars and about myself.
I thank Rosario, second-in-command, for rescuing me 42 times from space wreck. And I thank Fabio, foreign and alien relations officer, for establishing a fruitful dialogue with me and my personal computer. I bear in mind all your precious advice, my friends, and the beautiful discussions from which I learned so much.
I thank Iolanda and Silvio, who make a small space cabin the most funny place in the world.
Thanks to Fabrizio, the on board chief engineer, to Fausto, the 'steppen wolf' and to Enrico, the on board Relativity specialist, for always opening up my

mind to different and very interesting points of view.
I thank Lara, Antonio E., Saverio and Antonio P. who are now colonizing new frontiers, widening the limits of the known Universe.
My special thanks go to Gianluca and Simona, who didn't allow me to get lost on my way towards optics and related misteries, and who I have felt very close to me during this last year.
In the end I thank Daniele, who saved me from hypoglycemia in few occasions, as many of the people I have already mentioned, but he did it with beautiful, unforgettable home-made pies...
Thank you all, my friends! It's real fun space-travelling with you!

But I haven't finished yet...
My very special thanks go to the extraordinary group of Trento, who hosted me for some miles on their beautiful Au-coated spacecraft... It's a real pleasure travelling with such brave and fearless people!
I thank Stefano Vitale, who is the first person I heard speaking about LISA and made me fall in love with the mission.
In particular I thank Antonella, my favourite space-tango dancer, and Giacomo, my companion during the most adventurous expeditions in the most remote spots of the cosmos. I thank them, together with Bill, Ludovico, Rita, Mauro, David and Peter for the precious discussions, advice and general support.

Furthermore...
My special thanks go to Guido Celentano, who drove me through the dangers and the traps of the dark insides of bureaucracy, always keeping me smiling.
I thank with all my heart Grazia, Azzurra and Raffaele, my favourite space heroes: their friendship makes me feel warm also at the $0° K$ of the cosmic depths.

In the end...

I thank my mother and my father, who showed me the stars for the first time.
I thank my grandparents, who explained me some time ago that the white sphere in the night sky was not a ball, but the Moon.
I thank Dario, who sweetly holds my hand, while together we learn to fly a little higher every day.

I thank you all with all my love.